Long-lived charge carrier dynamics in polymer/quantum dot blends and organometal halide perovskites

Hirokazu Nagaoka

A dissertation submitted in partial fulfillment of the
requirements for the degree of
Doctorate of Philosophy in Chemistry

University of Washington
2014

Reading Committee:
David S. Ginger, Chair
Robert E. Synovec
Brandi M. Cossairt

Program Authorized to Offer Degree
Department of Chemistry

University of Washington

Abstract

Long-lived charge carrier dynamics in polymer/quantum dot blends and organometal halide perovskites

Hirokazu Nagaoka

Chair of the Supervisory Committee:
Professor David S. Ginger
Chemistry

Solution-processable semiconductors offer a potential route to deploy solar panels on a scale, based on the possibility of reduced manufacturing costs by using earth-abundant materials and inexpensive production technologies, such as inkjet or roll-to-roll printing. Understanding fundamental physics underlying device operation is important to realize this goal. This dissertation describes studies of two kinds of solar cells: hybrid polymer/PbS quantum dot solar cells and organometal halide perovskite solar cells. Chapter two discusses details of the experimental techniques. Chapter three and four explore the mechanisms of charge transfer and energy transfer spectroscopically, and find that both processes contribute to the device photocurrent. Chapter four investigates the important question of how the energy level alignment of quantum dot acceptors affects the operation of hybrid polymer/quantum dot solar cells, by making use of the size-tunable energy levels of PbS quantum dots. We observe that long-lived charge transfer yield is diminished at larger dot sizes as the energy level offset at the polymer/quantum dot interface is changed through decreasing quantum confinement using a combination of spectroscopy and device studies. Chapter five discusses the effects of TiO_2 surface chemistry on the performance of organometal halide perovskite solar cells. Specifically, chapter five studies the effect of replacing the conventional TiO_2 electrode with Zr-doped TiO_2 (Zr-TiO_2). We aim to explore the correlation between charge carrier dynamics and device studies by incorporating zirconium into TiO_2. We find that, compared to Zr-free controls, solar cells employing Zr-TiO_2 give rise to an increase in overall power conversion efficiency, and a decrease in hysteresis. We also observe longer carrier lifetimes and higher charge carrier densities in devices on Zr-TiO_2 electrodes at microsecond times in transient photovoltage experiments, as well as at longer persistent photovoltages extending from ~millisecond to tens of sec. Finally, we characterize the combined effects of pyridine treatment and Zr-TiO_2 on device performance and carrier lifetimes.

TABLE OF CONTENTS

Acknowlegements

I would like to thank a number of people for the completion of this dissertation. First, I thank my research advisor, Prof. David Ginger for providing his scientific vision. I have learned so much from you, how to perform and think about my research. Thank you for providing me with a wealth of opportunities and experiences throughout my time in graduate school. Much thanks to the members of the Ginger Research Group: Adam Colbert, Dr. Michael Salvador, Dr. Cody Schlenker, Dr. Fei Ma, Dane W. deQuilettes and Mark Ziffer. Lastly, I would like to acknowledge my parents, family and friends.

Hirokazu Nagaoka
December 2014

Chapter1: Introduction

1.1 Photovoltaics (Thin film technology)

The development of new energy technologies is important to meet increasing global energy consumption. From the standpoint of long term sustainability, solar energy provides a clean, renewable source of energy. Solar technologies have been fabricated from a wide variety of materials, with varying power conversion efficiencies (Figure 1).[1] Crystalline silicon solar panels currently dominate the photovoltaic market.[2] However, none of current technologies have yet met the challenge of low cost cells with low cost manufacturing along with an earth abundant non-toxic material that can be scaled to terawatt (TW) levels of power generation.

Solution-processable semiconductors have the potential to significantly decrease the manufacturing costs of photovoltaics by using methods such as inkjet or roll-to-roll printing. Organic photovoltaics (OPVs) have attractive advantages including light weight, mechanical flexibility, and high absorption coefficients. OPV devices are often based on conjugated polymers whose backbones are composed of alternating carbon-carbon single and double bonds, thereby allowing electron delocalization on the polymer backbone and resulting in the semiconducting properties. Photoexcitation of the conjugated polymer creates tightly-bound excitons (electron-hole pairs bound by Coulombic force), resulting from their low dielectric constants ($\varepsilon_r \approx$ 2-4)[3] compared to inorganic semiconductors (PbS, $\varepsilon_r \approx$ 17.2).[4] The large binding energy of the exciton, which is in the range of 0.1-0.5 eV, prevents exciton dissociation by the built-in electric field of a solar cell.[5, 6] One technique for splitting excitons is by means of a bulk heterojunction (BHJ) between donor and acceptor materials with different electron affinities. In particular, BHJs rely on the difference of energy levels between the donor and acceptor materials to align in a type-II heterojunction, (staggered energy levels) which provides the driving energy for exciton dissociation at donor/acceptor interface to generate free charges (Figure 2). Typical exciton diffusion lengths in organic semiconductor are ~10 nm. However, nanoscale phase separation allows more excitons to reach a donor/acceptor interface prior to recombination.[7] The most commonly studied OPV devices are made from BHJ blends of a conjugated polymer and a fullerene derivative, such as poly 3-hexylthiophene (P3HT): 6,6-phenyl C_{61} butyric acid methyl ester ($PC_{60}BM$).[8]

The use of quantum dot acceptors in place of fullerene, in principle, offers the advantage of harvesting of a larger portion of the solar spectrum than polymer/fullerene blends. Quantum dots could increase the efficiency of bulk heterojunction solar cells by increasing the dielectric environment, resulting in decreased Coulombic attraction between charges and, in turn, reduced non-geminate recombination and longer carrier lifetimes.[9] These blends also retain many of the advantages of OPVs, such as solution-processability and mechanical flexibility. Furthermore, the synthesized quantum dots are coated with an oleate capping layer on the quantum dot

surface.[10] However, the oleate capping ligand on the quantum dot surface works as an electrical barrier due to both the long chained length and the lack of conjugation.[11] Therefore, the quantum dot surfaces or polymer/quantum dot interface can be modified with shorter organic ligands (e.g. EDT: 1,2-ethanedithiol and MPA: 3-mercaptopropionic acid) through the exchange of long organic ligands while still retaining the quantum dot size, increasing charge carrier mobility in quantum dots[11, 12] and improving charge transfer at the polymer/quantum dot interface[9] due to the decrease of inter-particle distance and the distance between a polymer and quantum dots. Moreover, the ligand exchange process changes the chemical identity on the quantum dot surface which alters the surface dipole, leading to the energy level shifts of the conduction and valance bands.[13] More importantly, since the energy levels of the nanocrystals can be tuned through size-dependent quantum confinement effects, polymer/quantum dot blends allow us to systematically vary the energy level offsets between donor and acceptor to investigate the mechanism of photocurrent generation at polymer/quantum dot interface using photo-induced absorption (PIA) spectroscopy. Chapter four discusses these details.

Within the last few years, a new material has emerged in the PV field. Organometal halide perovskites which are of the formula $CH_3NH_3PbX_3$ (X= I, Cl, Br) serve as excellent light-harvesting materials and have rapidly reached 19% conversion efficiency.[14, 15] Furthermore, these perovskite solar cells have a potential for low fabrication costs due to solution processability and earth abundant materials.[15] Current thought is that the high device performance could be attributed to high charge-carrier mobilities intrinsic to these materials, which lead to the long carrier diffusion lengths[16, 17] or a large dielectric constants.[18] Demonstrating long charge-carrier diffusion lengths, Stranks *et al*. measured charge carrier diffusion lengths exceeding 1 μm for the mixed halide perovskites.[17] They argue that this allows the photo-generated electrons and holes to migrate long distances for extraction before they recombine and energy is lost as heat. The high quantum efficiencies and photocurrents observed in these systems are a direct result of the long carrier lifetimes.

However perovskite solar cells are not without their challenges. So far, most reported devices exhibit hysteresis in current-voltage curves.[19] Although no one has ever said so directly, Snaith et al. has assumed that hysteresis effects might be charge carrier trapping/detrapping in the defects of perovskite itself or interfaces between perovskite and charge collection layers, ion migration or ferroelectric properties.[19] Furthermore, they have reported that this hysteresis behavior might be attributed to the interface between perovskite and charge collection layers rather than the perovskite itself. This was shown by fabricating devices either with no compact TiO_2 (electron transporting layer) or no spiro-OMeTAD (hole transporting layer), and observing increased hysteresis.[19] Baumann et al. observed persistent photovoltages on longer timescale (several tens of seconds) in the perovskite ($CH_3NH_3PbI_3$) device through transient photovoltage

(TPV) experiments.[20] They argued that the persistent photovoltage could result from the back transfer of electrons or holes that are populated in the transporting layer into perovskite, or the slowly detrapped carriers due possibly to the presence of defects and grain boundaries within the perovskite film or at the transport layer interfaces, even as a result of a light induced ferroelectric polarization.[20]

In this dissertation, we investigate the effects of TiO_2 surface chemistry on the performance of organometal halide perovskite solar cells. Chapter five discusses these details.

The following two sections focus on the basic properties of quantum dots regarding hybrid solar cells, and properties of organometal halide perovskites.

1.2 What are quantum dots?

Quantum dots are semiconducting nanocrystals with energy levels and optical spectra that depend upon particle size due to quantum confinement effects. The quantum effects arise when the size of the quantum dots becomes smaller than the exciton Bohr radius of the first exciton state in the bulk semiconductor. In this size regime, the electron and hole energy levels become size dependent, and therefore the optical and electronic properties of crystals undergo drastic changes with crystal size. If an exciton is strongly confined to a sphere of radius *R* by an infinite potential *V*,

$$V(r) = \begin{cases} 0 & r < R \\ \infty & r > R \end{cases} \tag{1.1}$$

then for r>R, the wave function must be zero. This model is found in many textbooks[21]. The particle-in-a-sphere wavefunctions can be written as a product of a radial and an angular component,

$$\Phi_{n,\ell,m}(r,\theta,\phi) = C\,\frac{Y_\ell^m(\theta,\phi) j_\ell\left(k_{n,\ell} r\right)}{r} \tag{1.2}$$

where C is a normalization constant, $Y_\ell^m(\theta,\phi)$ is the spherical harmonic, and $j_\ell\left(k_{n,\ell} r\right)$ is the ℓ^{th} order spherical Bessel function, where $k_{n,\ell} = \alpha_{n,\ell}/R$ and $\alpha_{n,\ell}$ is the nth zero of j_ℓ. The energy levels of electrons and holes in such a nanocrystal are given by:

$$E_{n,l} = \frac{\hbar^2 k_{n,\ell}^2}{2m_o} = \frac{\hbar^2 \alpha_{n,\ell}^2}{2m_o R^2} \tag{1.3}$$

where $\hbar$ is the reduced Planck's constant and m_o is the mass of the particle. Equation 1.3 predicts the confinement energy of the particle in the sphere is inversely proportional to the square of the radius. As the nanocrystal radius decreases, the distance between the energy levels

of nanocrystal increases.

The aforementioned model describes empty sphere, whereas a spherical potential well is filled with semiconductor atoms. However, the particle-in-a-sphere model can be applied to this problem using a wave function that satisfies the periodic crystal potential. For direct band gap semiconductor, the energy of conduction and valence bands are approximated by using the effective mass approximation derived from Bloch's theorem.[22]

$$E_k^c = \frac{\hbar^2 k^2}{2m_c^*} + E_g \tag{1.4}$$

$$E_k^v = \frac{-\hbar^2 k^2}{2m_v^*} \tag{1.5}$$

where E_k is the energy of the particle as a function of wave number k. E_g is the semiconductor bandgap. m_c^* and m_v^* are the effective masses of carriers in the conduction and valence bands, respectively. The effective mass approximation provides charge carriers in the semiconductor behave as if they have a mass different from the mass of free particles, allowing us to treat the electron and hole as free particles (with a different mass).

In turn, these excited carriers do not behave as free carriers even if the effective mass approximation is applied to the particle-in-a-sphere model. The electron and hole are bound together in the quantum dots as an electron-hole pair due to Coulomb interaction energy between them. If a carrier is excited with larger energy than the bulk bandgap E_g, the energy of the first excited states E can be written as[23, 24]

$$E = E_g + \frac{\hbar^2 \pi^2}{2m_e^* R^2} + \frac{\hbar^2 \pi^2}{2m_h^* R^2} - \frac{1.8\, e^2}{4\pi\varepsilon\varepsilon_0\, R} \tag{1.6}$$

where the final term is Coulomb interaction energy. Here, e is the electron charge, and the dielectric constant of the semiconductor and the permittivity of free space are ε and ε_0, respectively.

In this dissertation, we use lead sulfide (PbS) quantum dots in the hybrid organic/inorganic solar cells. Bulk lead sulfide has an infrared band gap (0.41 eV) that shifts to the near IR region due to quantum confinement effects for the quantum dots as a result of the small effective mass (m_e^* = 0.085, m_h^* = 0.085) and the large exciton Bohr radius (18 nm).[4, 25] This enables the energy gap of the solar cells to be tuned into the near infrared (1.3 eV-0.7 eV) by altering the quantum dot size between 3 and 7 nm.[25-27] Furthermore, lead sulfide has a high dielectric constant ($\varepsilon_r \approx 17.2$)[4] that may be beneficial in screening Coulombic interactions

between the carriers to generate free charge carriers from photoexcited bound excitons, leading to reduced non-geminate recombination and longer carrier lifetime.[9]

1.3 Organometal halide perovskites

Organic-inorganic perovskites have been studied due to their interesting physical properties, such as superconductivity, magnetoresistance and ferroelectricity.[28, 29] The general crystal structure of organometal halide perovskites is ABX_3, where A is a monovalent metal cation or an organic ammonium cation ($R\text{-}NH^{3+}$), B is a divalent metal cation (e.g. Ge^{2+}, Sn^{2+}, Pb^{2+}) and X is a halogen anion (e.g. Cl^-, Br^-, I^-) that bonds to both cations.[30, 31] This structure consists of a three-dimentional (3D) network of corner-sharing BX_6 octahedra, where B is located at the center of the octahedra and X sits in the corner around metal cation B. The organic ammonium cation A is located in the 12-fold coordination sites between the octahedra to satisfy the charge-balancing of the whole network (Figure 3a).[31, 32] Ideally this perovskite structure shows the cubic unit cell.[33] However, many physical properties, particularly electric, dielectric, and ferroelectric properties are influenced by a distorted cubic structure due to tilting of the octahedral framework or off-center displacement of the metal cation.[34] Typically the physical properties of perovskites can be tailored by substituting chemical composition, resulting in different exciton binding energy[35] or band gap.[34]

An organic cation A can influence the whole lattice by changing the B-X bond length.[32] If the organic cation is too large, 3D perovskite structure can't be formed due to space limitations, leading to a lower (2D) layered perovskite structure (Figure 3b).[31] For instance, crystals of the form $(RNH_3)_2BI_4$ ($R=C_nH_{2n+1}$-) correspond to a 2D layered perovskite structure which have large exciton binding energies (150-540 meV) [35, 36] because they form a type I quantum well structure, composed of semiconducting metal halide layers sandwiched between organic insulating layers.[32] 2D layered perovskite structures show interesting optical properties, such as efficient photoluminescence[36] or bright electroluminescence.[37] In contrast, $CH_3NH_3PbI_3$ has a 3D cubic perovskite structure which lack organic barrier layers.[32] The exciton binding energy of $CH_3NH_3PbI_3$ is only 45 meV[35] which is only slightly larger than thermal energy k_bT at room temperature (25 meV), where k_b is the Boltzmann constant and T=298K.[35] Furthermore, the small ionic radius of organic cations (e.g. methylammonium: $CH_3NH_3^+$ or formamidinium: $NH=CHNH_3^+$) which forms a 3D perovskite structure can extend the band gap toward near IR region.[38]

The excitonic absorption and light emission of organometal halide perovskites can be readily tuned by changing different metal cations or halides. For a metal cation B (e.g. B= Ge, Sn or Pb), as the difference between the electronegativity of the B-X bond increases, the B-X bond length decreases.[34] Therefore, the light emission of organic metal halide perovskite

crystals can be shifted to a longer wavelength when changing the metal cation from Pb to Sn to Ge.[39] When the atomic size of the anions changes from Cl to Br to I with the increase in lattice constants, excitonic absorption spectra for Pb halide perovskite shows a red-shift when changing halogen from Cl to Br to I.[40] On the other hand, the use of mixed halide for perovskite structure (e.g. iodide with bromide or bromide with chloride) can tune the bandgap and the optical absorption to cover the whole visible spectrum.[34]

1.4 Thesis statement

In this dissertation I describe significant progress in terms of two kinds of solar cells: hybrid polymer/ PbS quantum dot solar cells and organometal halide perovskite solar cells. First, chapter two introduces experimental techniques to characterize my devices, especially photoinduced absorption spectroscopy (PIA) and to fabricate the perovskites device. In chapter three, I discuss experiments in terms of energy transfer in the polymer/quantum dot blend using photoluminescence excitation spectroscopy, where I found that energy transfer can effectively generate photocurrent within the devices. In chapter four, I discuss polymer/quantum dot blend (PTB1/PbS quantum dot) that works efficiently in photovoltaics. I observed that both the PIA signal associated with charge formation on the polymer, as well as the external quantum efficiency of the hybrid photovoltaic devices decrease in magnitude with increasing quantum dot size, despite the broader absorption spectrum of the larger dots. Finally, in chapter five I discuss the effects of TiO_2 surface chemistry on the performance of organometal halide perovskite solar cells.

Figures for Chapter1:

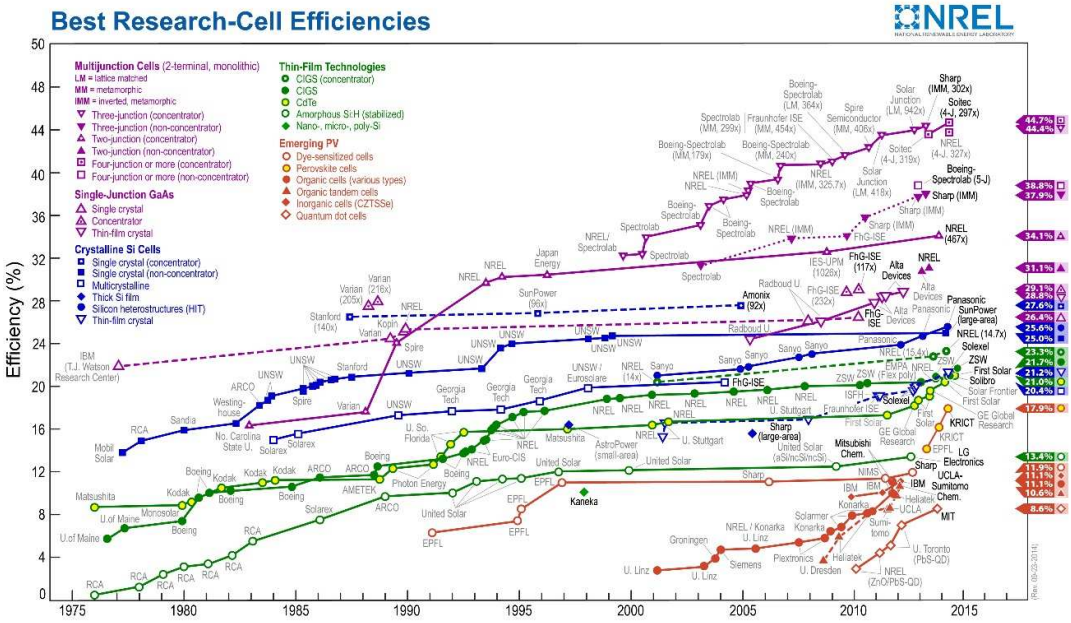

Figure 1 Best Research-Cell Efficiencies plotted by NREL. This chart consists of different kinds of solar cells: multijunction cells and single junction GaAs (purple), crystalline silicon (Si) cells (blue), thin-film technologies (green) and emerging PV (red). This chart is free and open to the public and can be downloaded on the NREL site **http://www.nrel.gov/ncpv/**.

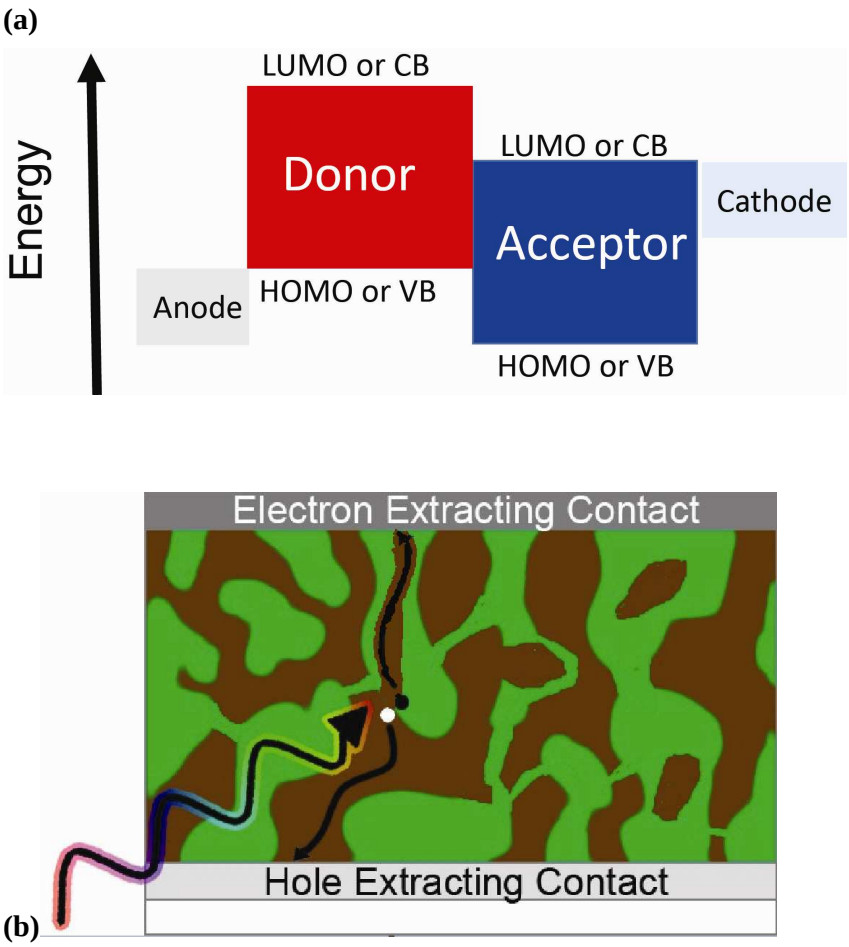

Figure 2 OPV devices based on donor–acceptor heterojunction architectures. (a) Energy level diagram with type-II heterojunction (b) Bulk heterojunction configuration

(a)

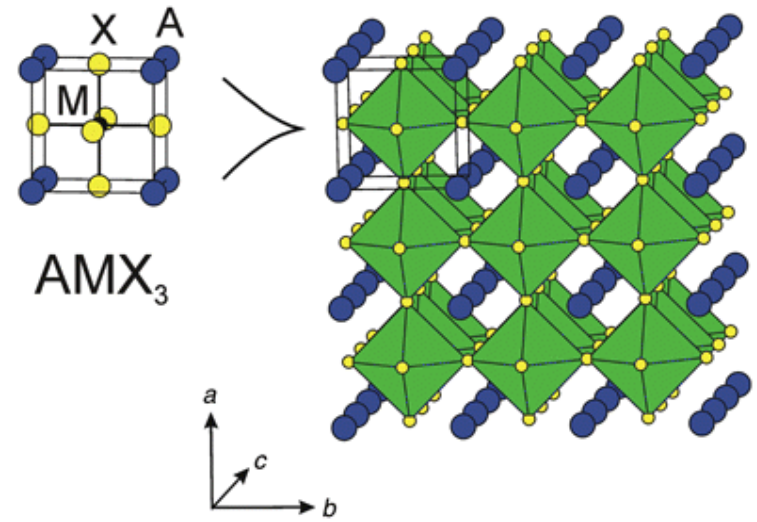

(b)

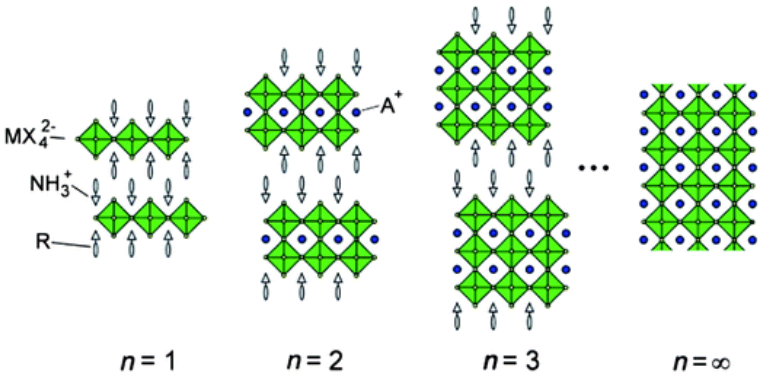

Figure 3 (a) Crystal structure of cubic metal halide perovskites of general formula ABX_3: A (blue) organic or inorganic cations, B(M) (grey) metal cations, X (yellow) halides. (b) Schematic representation of the 2D layered perovskite structure consists of metal halide layers sandwiched between organic insulating layers. The increase in layer number (n) of the inorganic framework leads to the lattice change toward 3D structure (n=∞). Reproduced with permission from Ref. 31. Copyright 2014 RSC

References

(1) Darling, S.; You, F. The case for organic photovoltaics. *Rsc Advances* **2013**, *3*, 17633-17648.

(2) IEA-ETSAP and IRENA Technology Brief E11 (2013) www.etsap.org – www.irena.org.

(3) Hilczer, M.; Tachiya, M. Unified Theory of Geminate and Bulk Electron-Hole Recombination in Organic Solar Cells. *Journal of Physical Chemistry C* **2010**, *114*, 6808-6813.

(4) Nanda, K.; Kruis, F.; Fissan, H.; Behera, S. Effective mass approximation for two extreme semiconductors: Band gap of PbS and CuBr nanoparticles. *Journal of Applied Physics* **2004**, *95*, 5035-5041.

(5) Alvarado, S.; Seidler, P.; Lidzey, D.; Bradley, D. Direct determination of the exciton binding energy of conjugated polymers using a scanning tunneling microscope. *Physical Review Letters* **1998**, *81*, 1082-1085.

(6) Chandross, M.; Mazumdar, S.; Jeglinski, S.; Wei, X.; Vardeny, Z.; Kwock, E.; Miller, T. Exitons in poly(para-phenylenevinylene). *Physical Review B* **1994**, *50*, 14702-14705.

(7) Halls, J.; Pichler, K.; Friend, R.; Moratti, S.; Holmes, A. Exciton diffusion and dissociation in a poly(p-phenylenevinylene)/C-60 heterojunction photovoltaic cell. *Applied Physics Letters* **1996**, *68*, 3120-3122.

(8) Dennler, G.; Scharber, M.; Brabec, C. Polymer-Fullerene Bulk-Heterojunction Solar Cells. *Advanced Materials* **2009**, *21*, 1323-1338.

(9) Noone, K.; Subramaniyan, S.; Zhang, Q.; Cao, G.; Jenekhe, S.; Ginger, D. Photoinduced Charge Transfer and Polaron Dynamics in Polymer and Hybrid Photovoltaic Thin Films: Organic vs Inorganic Acceptors. *Journal of Physical Chemistry C* **2011**, *115*, 24403-24410.

(10) Hines, M.; Scholes, G. Colloidal PbS nanocrystals with size-tunable near-infrared emission: Observation of post-synthesis self-narrowing of the particle size distribution. *Advanced Materials* **2003**, *15*, 1844-1849.

(11) Jeong, K.; Tang, J.; Liu, H.; Kim, J.; Schaefer, A.; Kemp, K.; Levina, L.; Wang, X.; Hoogland, S.; Debnath, R.; Brzozowski, L.; Sargent, E.; Asbury, J. Enhanced Mobility-Lifetime Products in PbS Colloidal Quantum Dot Photovoltaics. *ACS Nano* **2012**, *6*, 89-99.

(12) Ip, A.; Thon, S.; Hoogland, S.; Voznyy, O.; Zhitomirsky, D.; Debnath, R.; Levina, L.; Rollny, L.; Carey, G.; Fischer, A.; Kemp, K.; Kramer, I.; Ning, Z.; Labelle, A.; Chou, K.; Amassian, A.; Sargent, E. Hybrid passivated colloidal quantum dot solids. *Nature Nanotechnology* **2012**, *7*, 577-582.

(13) Munro, A.; Zacher, B.; Graham, A.; Armstrong, N. Photoemission Spectroscopy of Tethered CdSe Nanocrystals: Shifts in Ionization Potential and Local Vacuum Level As a Function of Nanocrystal Capping Ligand. *ACS Applied Materials & Interfaces* **2010**, *2*, 863-869.

(14) Zhou, H.; Chen, Q.; Li, G.; Luo, S.; Song, T.; Duan, H.; Hong, Z.; You, J.; Liu, Y.; Yang, Y. Interface engineering of highly efficient perovskite solar cells. *Science* **2014**, *345*, 542-546.
(15) Lee, M.; Teuscher, J.; Miyasaka, T.; Murakami, T.; Snaith, H. Efficient Hybrid Solar Cells Based on Meso-Superstructured Organometal Halide Perovskites. *Science* **2012**, *338*, 643-647.
(16) Cai, B.; Xing, Y.; Yang, Z.; Zhang, W.; Qiu, J. High performance hybrid solar cells sensitized by organolead halide perovskites. *Energy & Environmental Science* **2013**, *6*, 1480-1485.
(17) Stranks, S.; Eperon, G.; Grancini, G.; Menelaou, C.; Alcocer, M.; Leijtens, T.; Herz, L.; Petrozza, A.; Snaith, H. Electron-Hole Diffusion Lengths Exceeding 1 Micrometer in an Organometal Trihalide Perovskite Absorber. *Science* **2013**, *342*, 341-344.
(18) Juarez-Perez, E.; Sanchez, R.; Badia, L.; Garcia-Belmonte, G.; Kang, Y.; Mora-Sero, I.; Bisquert, J. Photoinduced Giant Dielectric Constant in Lead Halide Perovskite Solar Cells. *Journal of Physical Chemistry Letters* **2014**, *5*, 2390-2394.
(19) Snaith, H.; Abate, A.; Ball, J.; Eperon, G.; Leijtens, T.; Noel, N.; Stranks, S.; Wang, J.; Wojciechowski, K.; Zhang, W. Anomalous Hysteresis in Perovskite Solar Cells. *Journal of Physical Chemistry Letters* **2014**, *5*, 1511-1515.
(20) Baumann, A.; Tvingstedt, K.; Heiber, M.; Vath, S.; Momblona, C.; Bolink, H.; Dyakonov, V. Persistent photovoltage in methylammonium lead iodide perovskite solar cells. *Apl Materials* **2014**, *2*, 081501.
(21) S. Flugge. *Practical Quantum Mechanics*, Springer, Berlin, 1971.
(22) C. Kittle. In*troduction to Solid State Physics:* New york, Wiley, 1986 Ch8.
(23) Brus, L. Electron-electron and electron-hole interactions in small semiconductor crystallites - The size dependence of the lowest excited electronic state. *Journal of Chemical Physics* **1984**, *80*, 4403-4409.
(24) Bawendi, M.; Steigerwald, M.; Brus, L. The quantum-mechanics of larger semiconductor clusters (quantum dots). *Annual Review of Physical Chemistry* **1990**, *41*, 477-496.
(25) Moreels, I.; Lambert, K.; Smeets, D.; De Muynck, D.; Nollet, T.; Martins, J.; Vanhaecke, F.; Vantomme, A.; Delerue, C.; Allan, G.; Hens, Z. Size-Dependent Optical Properties of Colloidal PbS Quantum Dots. *ACS Nano* **2009**, *3*, 3023-3030.
(26) Jasieniak, J.; Califano, M.; Watkins, S. Size-Dependent Valence and Conduction Band-Edge Energies of Semiconductor Nanocrystals. *ACS Nano* **2011**, *5*, 5888-5902.
(27) Hyun, B.; Zhong, Y.; Bartnik, A.; Sun, L.; Abruna, H.; Wise, F.; Goodreau, J.; Matthews, J.; Leslie, T.; Borrelli, N. Electron Injection from Colloidal PbS Quantum Dots into Titanium Dioxide Nanoparticles. *ACS Nano* **2008**, *2*, 2206-2212.
(28) Mitzi, D.; Karlin, K. Synthesis, structure, and properties of organic-inorganic perovskites and related materials. *Progress in Inorganic Chemistry* **1999**, *48*, 1-121.

(29) Cava, R.; Batlogg, B.; Espinosa, G.; Ramirez, A.; Krajewski, J.; Peck, W.; Rupp, L.; Cooper, A. Superconductivity at 3.5 K in $BaPb_{0.75}Sb_{0.25}O_3$ - Why is Tc so low? *Nature* **1989**, *339*, 291-293.
(30) I. Borriello, G. Cantele, and D. Ninno, Ab initio investigation of hybrid organic-inorganic perovskites based on tin halides, *Phys. Rev. B* **2008**, *77*, 235214.
(31) Mitzi, D. Templating and structural engineering in organic-inorganic perovskites. *Journal of the Chemical Society-Dalton Transactions* **2001**, 1-12.
(32) Mitzi, D.; Chondroudis, K.; Kagan, C. Organic-inorganic electronics. *Ibm Journal of Research and Development* **2001**, *45*, 29-45.
(33) Glazer, A. Classification of tilted octahedra in perovskite. *Acta Crystallographica Section B-Structural Science* **1972**, *B 28*, 3384-3392.
(34) Gao, P.; Gratzel, M.; Nazeeruddin, M. Organohalide lead perovskites for photovoltaic applications. *Energy & Environmental Science* **2014**, *7*, 2448-2463.
(35) Muljarov, E.; Tikhodeev, S.; Gippius, N.; Ishihara, T. Excitons in self-organized semiconductor/insulator superlattices - PbI-based perovskite compounds. *Physical Review B* **1995**, *51*, 14370-14378.
(36) Dammak, T.; Koubaa, M.; Boukheddaden, K.; Bougzhala, H.; Mlayah, A.; Abid, Y. Two-Dimensional Excitons and Photoluminescence Properties of the Organic/Inorganic $(4\text{-}FC_6H_4C_2H_4NH_3)_2[PbI_4]$ Nanomaterial. *Journal of Physical Chemistry C* **2009**, *113*, 19305-19309.
(37) Hattori, T.; Taira, T.; Era, M.; Tsutsui, T.; Saito, S. Highly efficient electroluminescence from a heterostructure device combined with emissive layered-perovskite and an electron-transporting organic compound. *Chemical Physics Letters* **1996**, *254*, 103-108.
(38) Pellet, N.; Gao, P.; Gregori, G.; Yang, T.; Nazeeruddin, M.; Maier, J.; Gratzel, M. Mixed-Organic-Cation Perovskite Photovoltaics for Enhanced Solar-Light Harvesting. *Angewandte Chemie-International Edition* **2014**, *53*, 3151-3157.
(39) Mitzi, D. Synthesis, crystal structure, and optical and thermal properties of $(C_4H_9NH_3)_2MI_4$ (M=Ge, Sn, Pb). *Chemistry of Materials* **1996**, *8*, 791-800.
(40) Papavassiliou, G.; Mousdis, G.; Koutselas, I. Some new organic-inorganic hybrid semiconductors based on metal halide units: Structural, optical and related properties. *Advanced Materials For Optics and Electronics* **1999**, *9*, 265-271.
(41) Nelson, C. A.; Zhu, X. Y. Reversible Surface Electronic Traps in PbS Quantum Dot Solids Induced by an Order-Disorder Phase Transition in Capping Molecules. *Journal of the American Chemical Society* **2012**, *134*, 7592-7595.

Chapter2: Materials and Methods

2.1 Photoinduced absorption spectroscopy

Quasi-steady state photoinduced absorption (PIA) spectroscopy is a pump-probe technique used to characterize long-lived (μs-ms) photogenerated species, such as polarons. Polarons are positively charged species on the polymer backbone, created by charge transfer to an acceptor species following photoexcitation. Structural reorganization in the polymer leads to a change in the polymer electronic structure with unique spectral features. A probe beam measures these new sub-bandgap transitions on the polymer. For polymer/QD blends, polarons are generated on the conjugated polymer when photoinduced electron transfer occurs from the excited polymer to the quantum dots, or photoinduced hole transfer occurs from the excited QDs to the polymer. Here, I explain basic principles of photoinduced absorption (PIA) spectroscopy following a book chapter by Wohlgenannt, Ehrenfreund and Vardeny.[1]

In a PIA experiement, a sample is excited by the modulated pump beam. The measured intensity of pump beam in the film is given by

$$I_L(x) = I_L\, e^{\left(-\int_0^x \alpha(x')dx'\right)} = I_L\, e^{(-\alpha x)} \tag{2.1}$$

where I_L is the incident light intensity and α is the film absorption coefficient at the pump energy. This intensity profile generates some photoexcitation population density N(x,t) which give rise to variations, $\Delta\alpha(E,x,t)$:

$$\Delta\alpha(E,x,t) = \sigma(E)N(x,t) \tag{2.2}$$

where σ is the cross-section for absorption at photon energy E, x is position in the sample and t is time. The changes in absorption coefficient are directly proportional to the photoexicted population density N(x,t) and the cross-section for absorption. If we measure the PIA signal, $\frac{\Delta T}{T}$ can be written as

$$-\frac{\Delta T}{T}(E,t) = 1 - e^{\left(-\int_0^d \Delta\alpha(E,x,t)dx\right)} \tag{2.3}$$

where d is a film thickness of a sample. In practice, the measured PIA signal $\frac{\Delta T}{T} \sim 10^{-6} \ll 1$ and thus, we can approximate equation 2.3 as

$$-\frac{\Delta T}{T}(E,t) \simeq \int_0^d \Delta\alpha(E,x,t)dx \tag{2.4}$$

Therefore, the polaron signal $\frac{\Delta T}{T}$ corresponds to the photoinduced absorption of the sample.

Furthermore, in case of thin film (e.g. d=100 nm) which shows low optical density, thus $\alpha d \ll 1$, equation 2.4 can be written as

$$-\frac{\Delta T}{T}(E,t) \cong \Delta\alpha d = \sigma(E)N(x,t)d \tag{2.5}$$

The PIA signal can be regarded as being directly proportional to the photoexcited population density. Furthermore, the above equations show that the PIA signal is dependent on pump light intensity and pump modulation frequency. In the pump modulation-dependence technique, a modulated pump intensity $I(t)$ at a frequency ω can be written as $I(t) = I_0(\cos(\omega t) + 1)$, where I_0 is the pump light intensity (t = 0). We can investigate the recombination mechanism and the decay kinetics of photoexcited species by measuring the PIA signal as a function of pump-modulation frequency. Since the photoexcited population density N(t) are proportional to the measured PIA signals, the measured signals in both in-phase (N_I) and out-of-phase (N_o) components can be written as

$$N_I = \int N(t)\cos(\omega t)\,dt \tag{2.6}$$

$$N_o = \int N(t)\sin(\omega t)\,dt \tag{2.7}$$

In case monomolecular decay of the photoexcited carriers, the rate equation can be described as[2]

$$\frac{dN(t)}{dt} = gI(t) - \gamma N(t) \tag{2.8}$$

where $\frac{dN(t)}{dt}$ is the change in the photoexcited carrier density per unit time, g is the generation rate constant, $gI(t)$ is generation rate, γ is the monomolecular recombination constant which is the inverse monomolecular decay lifetime of the carrier ($\gamma = 1/\tau$) and thus the decay rate is $\gamma N(t)$. Equation (2.8) can be solved by using an approximation for the steady-state case ($t \gg \tau$), and leading to the equation which represents the photoinduced steady state signal N_s:[2]

$$N_s = \frac{gI_0\tau}{\sqrt{1+(\omega\tau)^2}} \tag{2.9}$$

where N_s is proportional to ΔT and thus the PIA signal is linearly dependent on pump intensity. Furthermore, for $\omega\tau \gg 1$ (at high frequency), the signal is inversely dependent on pump modulation frequency ($N_s \propto \omega^{-1}$), while for $\omega\tau \ll 1$ (at low frequency) the signal is independent on the pump modulation frequency.

In case of bimolecular recombination, the kinetics equation is given by[2]

$$\frac{dN(t)}{dt} = gI(t) - \beta N^2(t) \tag{2.10}$$

where β is the bimolecular decay constant, thus the decay rate is $\beta N^2(t)$. When bimolecular recombination dominates, the steady-state photoinduced signal is given approximately by[2]

$$N_s = \frac{\sqrt{\frac{gI_0}{\beta}}\alpha \tanh(\alpha)}{\alpha + \tanh(\alpha)} \tag{2.11}$$

where for small values of $\alpha = \frac{\pi}{\omega\tau_s}$ ($\omega\tau_s \gg 1$), $N_s \propto \omega^{-1}$, while for large values of α ($\omega\tau_s \ll 1$), $N_s = \sqrt{gI_0/\beta}$ and $\tau_s = \frac{1}{\sqrt{g\beta I_0}}$. Thus, the PIA signal is independent of ω and shows a square root dependence on the pump light intensity.

$$\frac{\Delta T}{T} \propto \sqrt{I_0} \tag{2.12}$$

Consequently equations (2.9) and (2.11) allow us to assign two types of recombination processes by means of the dependence of the PIA signals on pump light intensity and pump modulation frequency. For low pump light intensity, monomolecular and bimolecular recombination are effective, while bimolecular recombination becomes dominant for high pump light intensity due to high photoexcited carrier density. Furthermore, both recombination processes show similar frequency dependent behavior. However, at low frequency (near the steady state), they can be distinguishable based on their light intensity dependence. In the case of monomolecular decay, the PIA signal is linearly dependent on the pump light intensity. On the other hand, the signal is dependent on $\sqrt{I_0}$ for bimolecular decay. Therefore, in the case of both recombination processes occurring simultaneously or where recombination is dispersive, the PIA signal can be fitted by using a power law with power that lies between 0.5 and 1.

$$\frac{\Delta T}{T} \propto (I_0)^b \tag{2.13}$$

where $0.5 < b < 1$. For purely first-order monomolecular recombination, $\frac{\Delta T}{T}$ should be linear in light intensity (b=1), while purely for second-order bimolecular recombination, $\frac{\Delta T}{T}$ should be scaled in light intensity by means of a power law with b = 0.5.

Ultimately, PIA spectroscopy allows us to understand the dependence of a long-lived excited state population on the modulation frequency for pump excitation and the pump light intensity, thereby, access the information pertaining to recombination dynamics and decay kinetics of the photogenerated species through PIA data.

Experimental details:

Figure 1 shows the experimental setup for acquiring PIA spectra using standard lock-in techniques.[1, 3] The sample is excited with an electrically modulated light emitting diode (LED; Luxeon Rebel) using an Agilent 33120A arbitrary waveform generator (function generator) with a home-built driver circuit and probed with a monochromated tungsten halogen lamp. The resulting signal is detected via a Si/InGaAs dual-band photodetector (Thorlabs, DSD2) with sensitivity from the visible to the near-IR (500−1700 nm). The use of a second monochromator and a longpass filter in front of the photodetector facilitates better isolation of the PIA signal from the pump beam. A preamplifer (SR570) and a lock-in amplifier (SR830) are used to detect the small fractional changes in the probe beam transmission (ΔT) at each measured probe beam wavelength, which are corrected by subtracting sample photoluminescence (PL) or scattered pump beam from the PIA signal, and normalized to the probe beam transmission (T) as ΔT/T. The sample's PL spectra were acquired in parallel with the PIA signal by blocking the probe beam at each wavelength using an automated shutter. The lock-in is phased to a modulated pump frequency (200Hz) of scattered LED pump beam without longpass filter prior to measurement. The lock-in was phased such that signal with a short lifetime, such as the scattered pump excitation, was entirely a positive signal in the X-channel (in-phase) of the lock-in. As a result, signals arising due to photoinduced absorption are negative in the X channel. PIA signals lasting longer than the inverse of the pump frequency appear positive in the Y-channel (out-of-phase), which is 90° phase lagged from the X-channel. The total PIA signal is expressed by $R = (X^2 + Y^2)^{1/2}$, where the X and Y are components of the X channel and Y channel, respectively. Samples were held under active vacuum during PIA measurements.

2.2 Perovskite device fabrication

Figure 2a shows an illustration of the device configuration of the perovskite solar cells I used in this dissertation. The device structure, from bottom to top, consists of a transparent electrode, which is a transparent conducting oxide, usually fluorine-doped tin oxide (FTO) or indium-doped tin oxide (ITO). This is followed by n-type metal oxide (e.g. ZnO or TiO_2) as an electron transporting layer (ETL). Next, the photoactive layer consists of an organometal perovskite material (e.g. $CH_3NH_3PbI_{3-x}Cl_x$). The 2,2′,7,7′-Tetrakis (*N*,*N*-di-*p*-methoxy phenylamine)-9,9′-spirobifluorene (spiro-OMeTAD) is used for a hole transporting layer (HTL) (Figure 2b). Finally, the bottom contact is composed of a metal electrode, such as silver (Ag) or gold (Au). The following section describes the device fabrication techniques.

Methylammonium iodide. Methylammonium iodide was prepared following a previous report.[4] 24 mL of methylamine solution (0.193 mol, 33% in ethanol, Sigma) was diluted with

100 mL of ethanol. 10 mL aqueous solution of hydriodic acid (0.076 mol, 57 wt% in water, Sigma) was added to this solution under constant stirring. After a reaction time of 1 h at room temperature, the resulting solution was evaporated at 100°C for more than 12 hours. The obtained crude product was washed with dry diethyl ether, and then recrystallized using a mixed solvent of ethanol and ether. Finally the obtained white crystals were dried under vacuum overnight. This white crystalline powder should be stored under a dry nitrogen atmosphere.

Perovskite precursor solution. 0.8 g of dried methylammonium iodide (MAI) and 0.46 g of lead(II) chloride ($PbCl_2$, 99.999%, Alfa Aesar) were dissolved in anhydrous N,N-dimethylformamide (DMF, Sigma) at a 3:1 molar ratio of MAI to $PbCl_2$, with final concentrations 0.83 M lead chloride and 2.5 M methylammonium iodide to form the non-stoichiometric $CH_3NH_3PbI_{3-x}Cl_x$ precursor solution. This solution should be stored under a dry nitrogen atmosphere.

Sol-gel TiO_2. The preparation of sol-gel TiO_2 was carried out in air ambient at room temperature.[5] 5 mL Titanium (IV) n-butoxide (1.43 mmol, 97%, Sigma) was mixed with 4 mL of triethanolamine (98%, Sigma) and 25 mL of anhydrous ethyl alcohol in a flask under continuous magnetic agitation for 1 h, ((where a 0.34 mL of Zirconium (IV) butoxide solution (0.74 mmol, 80 wt. % in 1-butanol, Sigma) would be added for Zr-doped TiO_2 electrodes, Zr/Ti molar ratio being 5%.)) 5 mL of Acetic acid (glacial, Macron Fine Chemicals) and 5 mL of deionized water were then added into the mixture with continuous magnetic agitation for 24 h. The resulting solution was clear and transparent. The solution was filtered through a 0.45 μm PTFE syringe filter prior to spin-coating.

Perovskite solar cells. FTO coated glass sheets (7 Ω/sq, Aldrich) were etched with zinc powder and HCl (4 M) to obtain the required electrode pattern. The sheets were then washed with soap (2 vol % Micro-90, International Products Corp., in purified deionized water), deionized water, acetone, and isopropanol and finally treated under oxygen plasma for 10 min to remove the last traces of organic residues prior to spin-coating. The sol-gel derived TiO_2 electrodes were coated on FTO substrates using spin-coating with following heat treatment. 60 μL of the sol-gel TiO_2 solution were deposited on the FTO substrates by dynamical spin-coating at 3500 rpm for 1 min, following by heat treatment in air on a hotplate at 500 ºC for 1 hour to achieve full anatase crystallization. To form the perovskite layer for devices, the non- stoichiometric precursor was spin-coated on the prepared TiO_2 films in a nitrogen- filled glovebox, at 2000 rpm for 60 s. After spin-coating, the films were left to dry at room temperature in the glovebox for 30 minutes, to allow slow solvent evaporation. They were then annealed on a hotplate in the glovebox at

90 °C for 120 minutes, and then heating at 120°C for 15 min. During the annealing procedure at 90°C, the coated substrate changed color from light yellow to dark brown, indicating the formation of the perovskite film. After drying, the films were covered with Spiro-OMeTAD (Borun Chemicals, 99.47% purity). 96 mg of Spiro-OMeTAD were dissolved in 1 mL of chlorobenzene and mixed with 10 μL 4-*tert* -butylpyridine (*t* BP, 96%, sigma) and 43 μL of a 175 mg mL^{-1} bis (trifluoromethane) sulfonimide lithium salt (Li-TFSI, 99.95% sigma) solution in acetonitrile. This solution was spincoated at 4000 rpm for 1 min. Before evaporating the gold electrodes, Spiro-OMeTAD was allowed to oxidize in air over night at room temperature in the dessicator. For the counter electrode, a 100 nm-thick Au was deposited on the top of the Spiro-OMeTAD over layer by a thermal evaporation, where Au evaporated with a base pressure below 5×10^{-7} Torr.

Figures for Chapter2:

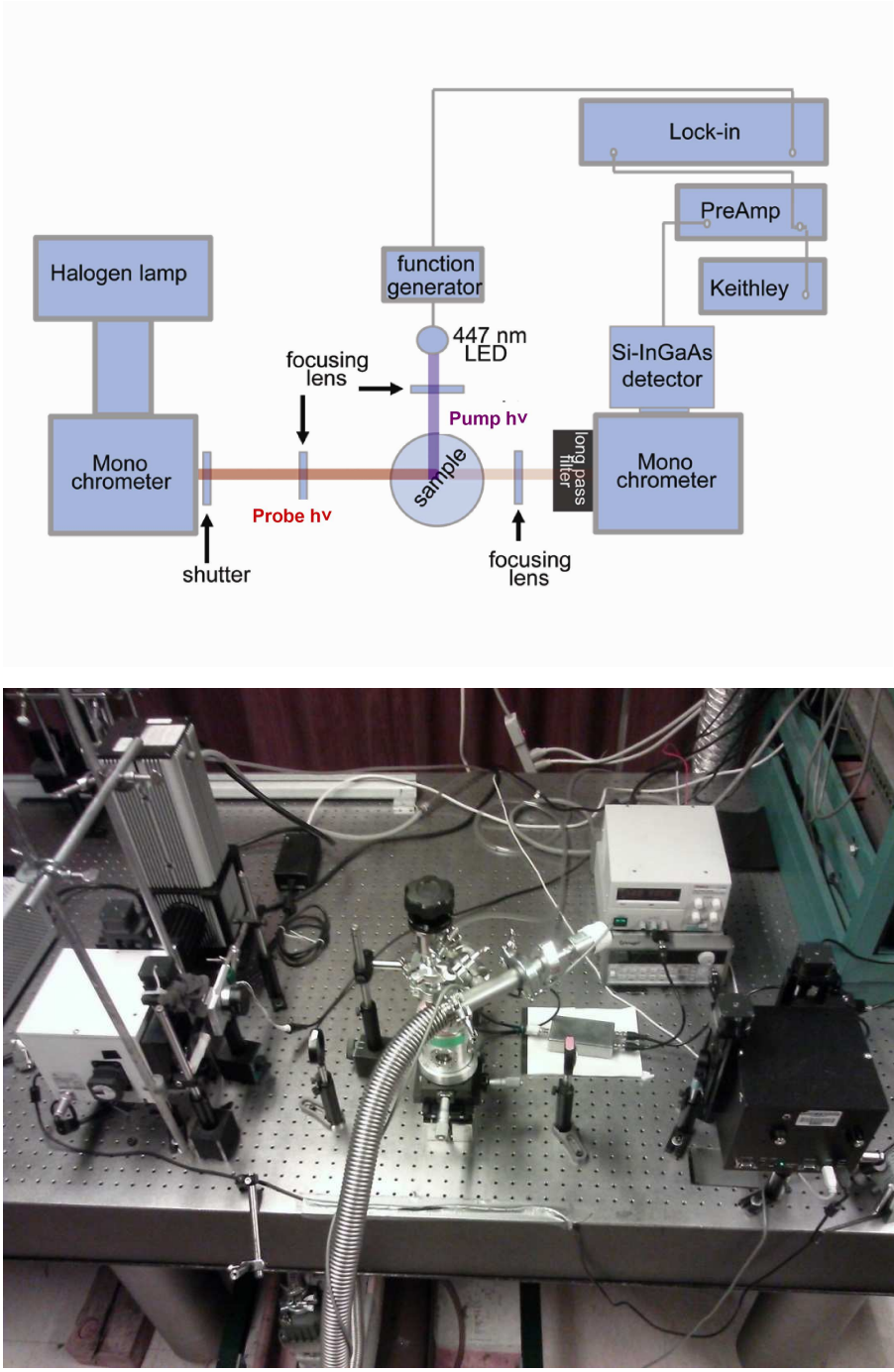

Figure 1 Schematic illustration of PIA setup (top) and photograph of the PIA bench (bottom).

(a)

(b)

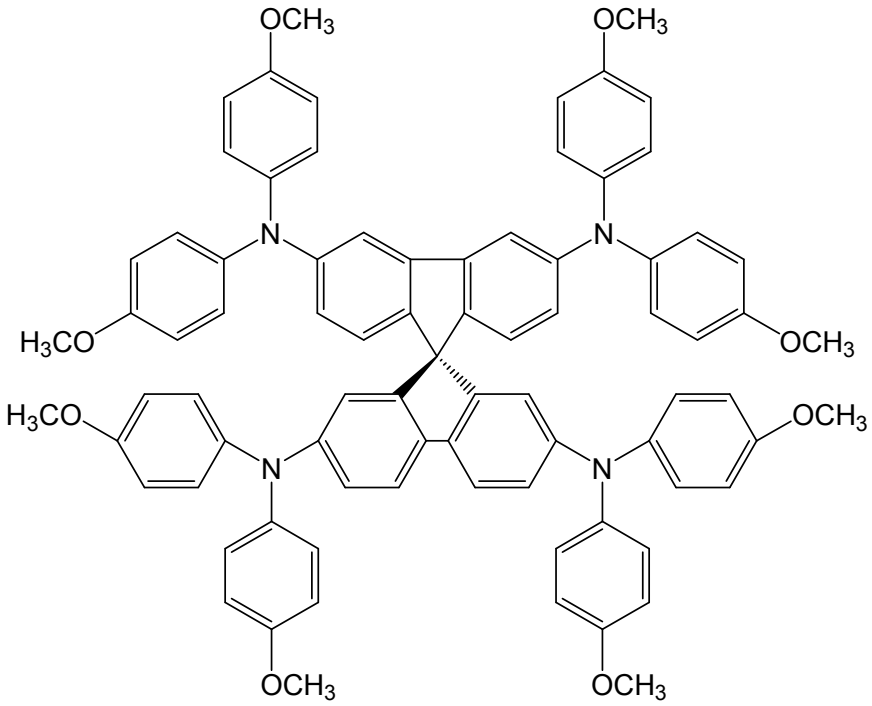

Figure 2 (a) Schematics of common layer structure of perovskite devices (b) The structure of 2,2′,7,7′-Tetrakis(*N*,*N*-di-*p*-methoxyphenylamine)-9,9′-spirobifluorene (spiro-OMeTAD).

References:

(1) Wohlgenannt, M.; Ehrenfreund, E. and Vardeny, Z. in *Photophysics of Molecular Materials: From Single Molecules to Single Crystals*, ed. Lanzani, G. Wiley-VCH, Weinheim,. 2006, Ch.5, pp 183-259.

(2) Botta, C.; Luzzati, S.; Tubino, R.; Bradley, D.; Friend, R. Photoinduced absorption of polymer solutions. *Physical Review B* **1993**, *48*, 14809-14817.

(3) Ginger, D.; Greenham, N. Photoinduced electron transfer from conjugated polymers to CdSe nanocrystals. *Physical Review B* **1999**, *59*, 10622-10629.

(4) Lee, M.; Teuscher, J.; Miyasaka, T.; Murakami, T.; Snaith, H. Efficient Hybrid Solar Cells Based on Meso-Superstructured Organometal Halide Perovskites. *Science* **2012**, *338*, 643-647.

(5) Tang, J.; Kemp, K.; Hoogland, S.; Jeong, K.; Liu, H.; Levina, L.; Furukawa, M.; Wang, X.; Debnath, R.; Cha, D.; Chou, K.; Fischer, A.; Amassian, A.; Asbury, J.; Sargent, E. Colloidal-quantum-dot photovoltaics using atomic-ligand passivation. *Nature Materials* **2011**, *10*, 765-771.

Chapter 3:

Charge Generation and Energy Transfer in Hybrid Polymer/Infrared Quantum Dot Solar Cells

In this chapter, we study photocurrent generation processes in hybrid polymer/quantum dot photovoltaics by comparing device performance and photoinduced absorption (PIA) spectra across blends of 3 different conjugated polymers, poly(2,3-bis(2-(hexyldecyl)-quinoxaline-5,8-diyl-alt-N-(2-hexyldecyl)-dithieno-[3,2-b:20,30-d]pyrrole) (PDTPQx-HD), poly[(4,40-bis (3-(2-hexyl-decyl)-dithieno[3,2-b:20,30-d]pyrrole)-2,6-diyl-alt-(2,5-bis(3-(2-ethyl-hexyl)-thioph en-2yl)thiazolo[5,4-d]thiazole)] (PPEHTT), and poly[(4,40-bis(2-octyl)dithieno [3,2-b:2030-d] silole)-2,6-diyl-alt-(2,5-bis(3-octylthiophen-2yl)thiazolo[5,4-d]thiazole)] (PSOTT) with PbS quantum dots. The PIA spectra and device performance provide evidence for long-lived photoinduced charge separation and bulk heterojunction device operation for blends of both PDTPQx-HD and PPEHTT with PbS. In contrast we find that PSOTT/PbS blends can produce viable solar cells without any evidence for long-lived charge transfer in the PIA spectra. Even so, the external quantum efficiency (EQE) spectra of PSOTT/PbS solar cells indicate that the polymer plays a significant role in light harvesting. We use photoluminescence excitation spectroscopy to confirm that the polymer funnels energy to the PbS quantum dots via energy transfer, and speculate that these blends may operate as PbS Schottky diodes sensitized by energy transfer from the semiconducting polymer host.

I partially contributed to this work that is particularly photoluminescence excitation spectroscopy experiments to determine if energy transfer is a possible mechanism for photocurrent generation for a specific polymer/quantum dot blend (PSOTT/PbS). To test the plausibility of this energy transfer hypothesis, we collected photoluminescence excitation (PLE) spectra by monitoring the quantum dot photoluminescence signal while sweeping the excitation light on the following three different films: pristine PSOTT, neat PbS and a PSOTT/PbS blend. Figure 1 shows the resulting PLE data. As expected, the PLE trace for the pristine quantum dot film detected at the quantum dot emission peak (dashed green line) tracks the quantum dot

absorption spectrum. Likewise the neat PSOTT polymer film shows no detectable emission at the quantum dot emission peak (thin gray line), and a PLE trace that follows the polymer absorption spectrum when detected at the polymer emission peak (dotted blue line). Notably, the PLE trace for the PSOTT/PbS quantum dot blend (collected at the quantum dot emission) shows a strong feature that exactly matches the polymer absorption peak, providing strong evidence that energy transfer can indeed occur from PSOTT to PbS quantum dots in this size range.

Experimental methods

Photoluminescence Excitation Measurements. Photoluminescence excitation (PLE) samples were made by spin coating on glass in the same way as the PIA samples. Since EDT treatment tends to quench the signal[41] we need to monitor (the quantum dot photoluminescence) the presented samples were left untreated. The same monochromated tungsten halogen lamp used for PIA spectroscopy was used as the excitation source and sample photoluminescence intensity was monitored with the same Si/InGaAs dual-band photodetector (ThorLabs, DSD2). A 900 nm long pass filter was used to filter excitation light in the pristine PSOTT spectrum, and a 1300 nm long pass filter was used to filter both scattered excitation light and polymer PL in the pristine PbS, PSOTT/PbS, and pristine PSOTT control samples. Samples were held under dynamic vacuum with the film facing the excitation light. Emitted light was wave-guided from the side of the glass substrate and focused using two aspheric lenses mounted in front of the photodetector. A fraction of the excitation light was split with a glass microscope slide to monitor the excitation intensity with an amplified silicon (λ <= 1000 nm) or an amplified InGaAs (λ > 1000 nm) photodetectors. All spectra were normalized to the excitation intensity. Spectra for Pristine PbS and PSOTT/PbS were normalized to the nanocrystal exciton peak at ~1160 nm. The pristine PSOTT spectra were scaled to match the blend intensity at 600 nm. Figure 2 shows schematic diagram of the experimental setup for PLE measurements.

Figures for Chapter3:

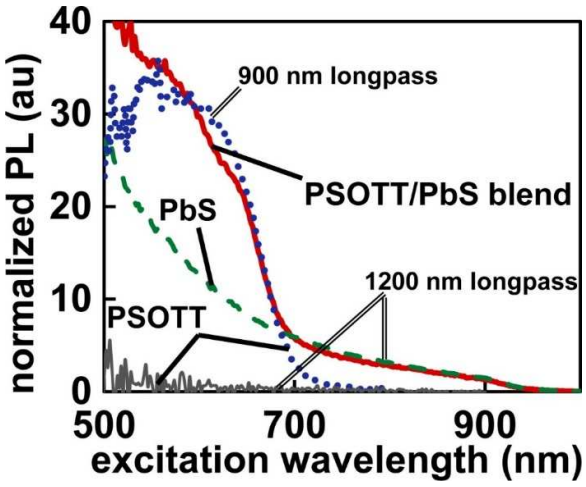

Figure 1 Photoluminescence excitation data. The red (solid) line is signal from light detected at wavelengths greater than 1200 nm for PSOTT blended with PbS. The blue (dotted) line is signal from light detected at wavelengths greater than 900 for a pristine PSOTT. The green (dashed) line is signal from light from neat PbS detected at wavelengths greater than 1200 nm. The gray (thin solid) line shows that no signal is detected from pristine PSOTT at wavelengths greater than 1200 nm.

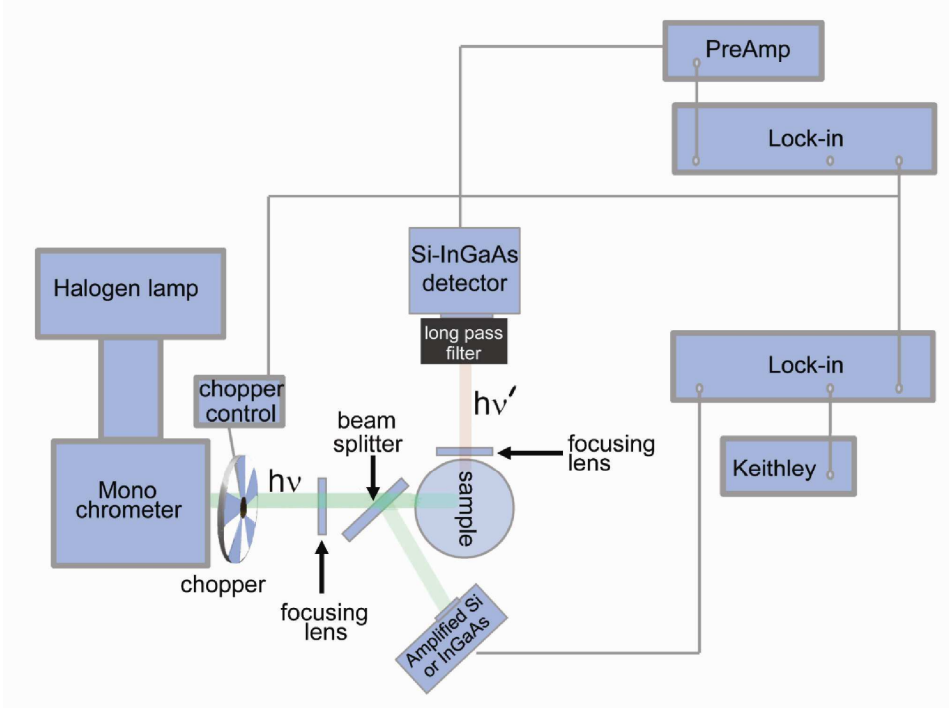

Figure 2 Schematic of the PLE set up

(1) Nelson, G.; Zhu, X. Reversible Surface Electronic Traps in PbS Quantum Dot Solids Induced by an Order-Disorder Phase Transition in Capping Molecules. *J. Am. Chem. Soc.* **2012**, *134*, 7592-7595.

Chapter 4:

Size-Dependent Charge Transfer Yields in Conjugated Polymer/Quantum Dot Blends

Introduction

Hybrid photovoltaics based on composites of conjugated polymers and inorganic semiconductors have attracted attention due to their potential as renewable energy sources with low fabrication costs.[1-16] Furthermore, understanding charge collection and recombination at the organic/inorganic interface is important for both organic solar cells,[17] and possibly for hybrids made from perovskites with organic hole transport layers.[14] Inorganic PbS QDs are not only attractive models for studying basic charge generation processes, but are also viable potential substitutes for fullerene acceptors due to their tunable band gaps, broad absorption spectra extending into the infrared, the possibility for carrier multiplication,[18-20] and their good carrier mobilities.[21,22] Furthermore, the use of nanocrystalline inorganic acceptors such as quantum dots in place of fullerenes could increase the efficiency of bulk heterojunction solar cells by increasing the local dielectric constant,[4,23,24] while retaining many of the mechanical and processing advantages of a flexible polymer solar cell. While polymer/quantum dot solar cells are among the most efficient nonfullerene bulk heterojunctions so far reported,[25] the performance achieved by hybrid quantum dot/organic cells still lags behind the efficiencies reported with both all-organic cells using fullerene as acceptors[26] and purely inorganic solar cells made using only quantum dots[27] or nanocrystal precursor inks.[28] A better understanding of the operating mechanisms of polymer/quantum dot cells has the potential not only to improve the performance of this class of devices, but also to provide insight into the limits of fullerene-based cells by allowing one to vary systematically properties such as the energy offset at the donor/acceptor interface by tuning the quantum dot size.

Early on, it was assumed that polymer/quantum dot cells would operate as bulk heterojunction cells, with type II heterojunctions supporting bidirectional charge transfer across

the polymer/quantum dot interface. There is strong evidence that some cells do behave as bulk heterojunctions, with charge transfer between the polymer and quantum dots.[2,3] However, recent evidence indicates that the rates of forward (electron) and reverse (hole) charge transfer are not always equal in these blends.[7] Furthermore, we have hypothesized that some polymer/quantum dot composites may operate, at least in part, as energy-transfer-sensitized Schottky-diode cells.[6] Thus, there is interest in exploring the operational mechanism of polymer/quantum dot blends, especially as one varies the energy level offset at the polymer/quantum dot interface.

Herein, we study blends of a newer high-performance conjugated polymer, poly((4,8-bis(octyloxy)benzo(1,2-*b*:4,5-*b′*)dithiophene-2,6-diyl)(2-((dodecyloxy)carbonyl)thieno(3,4-*b*)thiophenediyl)) (PTB1), with PbS quantum dots of various sizes. We aim both to explore the mechanism of photocurrent generation in these blends and, importantly, to understand how changing the energy level alignment of the quantum dot acceptor with quantum dot size affects their operation. Perhaps surprisingly, we find that for the PTB1/PbS blends described here, increasing the size of the quantum dots so that they harvest more of the solar spectrum has the consequence of reducing photocurrent by decreasing the yield of photogenerated charges in the film.

Experimental methods

Materials. PTB1 was purchased from 1-Material. Lead(II) oxide powder (PbO; 99.999+%), oleic acid (technical grade, 90%), 1-octadecene (ODE; >95%), zinc acetate dihydrate (≥98%), potassium hydroxide (≥85%), hexamethyldisilathiane (HMDS; synthesis grade), 3-mercaptopropionic acid (≥99%), and butylamine (>99.5%) were purchased from Sigma-Aldrich. All organic solvents were purchased from Sigma-Aldrich.

PbS Synthesis. PbS quantum dots were synthesized via a modified protocol reported by Hines et al.[29] The first excitonic peaks of PbS quantum dots were tuned by controlling reaction temperatures and the concentrations of precursors. A typical synthetic procedure for PbS quantum dots with a characteristic first excitonic peak of 1.30 eV is as follows. The lead precursor solution is prepared by stirring 2 mmol of lead(II) oxide with 4 mmol of oleic acid in 14 g of 1-octadecene in a three-neck flask under vacuum at 110 °C for at least 1 h. After 1 h, the solution is typically clear, and the flask is placed under flowing nitrogen gas and the temperature is raised to 140 °C. Simultaneously, a sulfur precursor solution of 1 mmol of hexamethyldisilathiane and 4 g of ODE is prepared in another sealed flask under flowing nitrogen gas. Using a syringe with a 13 gauge needle, the sulfur precursor is rapidly injected into the hot lead precursor. The flask containing the mixture is then cooled in a water bath to quench the reaction. The products are isolated from unreacted precursors and other impurities

by precipitation with acetone followed by centrifugation. The resulting precipitate is dispersed in a minimum volume of hexanes and extracted at least three times with methanol. The final products are stored in hexanes in the dark.

Butylamine Ligand Exchange. The quantum dot ligand exchange procedure is carried out in air through a modified protocol reported by Noone et al.[3] 2 mL of butylamine is added to the dried products of a typical synthesis; this suspension is allowed to sit for 20 min with sonication to aid the dispersion of the quantum dots before being precipitated with excess methanol, and then centrifuged at 3500 rpm (Eppendorf Centrifuge 5804). The supernatant is discarded, and the precipitate is dried under nitrogen gas. The dry precipitate is redispersed in another 2 mL of butylamine, again with the aid of sonication for 20 min, and then precipitated with excess isopropanol, centrifuged, the supernatant is discarded, and the dot pellet dried. The quantum dots are then dispersed for a third and final time in 2 mL of butylamine and allowed to sit with sonication for 20 min. The ligand exchanged quantum dots are isolated by adding just enough isopropanol to precipitate them and then centrifuging. The dots are then dried and immediately dispersed into filtered dichlorobenzene in the glovebox. Once dissolved, these solutions are allowed to sit with sonication to aid the dispersion of the quantum dots, centrifuged at 3500 rpm to remove any aggregates, and then filtered through 0.45 μm PTFE syringe filters to prepare them for use in active layers for PIA or device experiments.

Colloidal ZnO Nanocrystal Synthesis. ZnO nanocrystals are prepared according to a literature method developed by Sun with some modification.[30] Zinc acetate dihydrate ($Zn(Ac)_2 \cdot 2H_2O$, 0.8182 g, 3.73 mmol) was added into a flask containing 42 mL of methanol. The solution was heated to 60 °C with magnetic stirring. Potassium hydroxide (KOH, 0.4859 g, 7.22 mmol) was dissolved in 23 mL of methanol as the stock solution and then dropped into the flask within 10 min. It was prepared with magnetic stirring at a constant temperature of 60 °C for 2 h. The resulting opaque white colloid was isolated from unreacted precursors by centrifugation at 1000 rpm (Eppendorf Centrifuge 5804). The isolated nanocrystals were cleaned three times by the addition of 20 mL of methanol, agitated by vortexing, and centrifuged. The supernatant was discarded between cycles. This cleaning process was repeated three times. Finally, 10 mL of chloroform and 400 μL of *n*-butylamine were used to disperse the ZnO nanocrystals at a concentration of ~20 mg/mL.

Active Layer Solution Protocol. All solutions were prepared in filtered dichlorobenzene. A 10 mg/mL solution of a PTB1 polymer was prepared in anhydrous dichlorobenzene and stirred at 80 °C for at least 12 h before making blend solutions. All solutions were filtered through 0.45 μm PTFE syringe filters before combining with the PbS solutions.

Device Fabrication Protocol. 1.5 cm × 1.5 cm indium tin oxide (ITO) substrates were first scrubbed with detergent solution (2 vol % Micro-90, International Products Corp., in

purified deionized water), and then cleaned by subsequent sonication in purified deionized water, acetone, and then isopropanol for 10 min each. The ITO was then etched with 1 M $FeCl_3$ in hydrochloric acid to produce a 9 mm wide strip of ITO in the center of the substrate. The etched ITO was then further cleaned in a second round of subsequent acetone and then isopropanol with sonication for 20 min each. The ITO substrates were then cleaned by air plasma treatment for 10 min. ZnO was immediately spin-coated from a chloroform solution at 2500 rpm to give a ~30 nm coating of ZnO nanocrystals (as measured by surface profilometery). Coated substrates were annealed at 300 °C for 30 min in air, and then cooled to room temperature. All subsequent sample preparation steps were performed in a nitrogen glovebox. A blend solution was prepared by mixing the PTB1 and PbS QDs solutions in a 1:9 (w/w) ratio, and stirring at 80 °C for at least 1 h. PTB1/PbS active layers were then spin-coated on ZnO-coated ITO for 1 min at 1000 or 1500 rpm. For PIA samples, films were spin coated under the same conditions onto 1.5 cm × 1.5 cm glass microscope slides. Spin-coated films were treated with 3-mercaptopropionic acid to remove ligands and passivate the surface according to a procedure adapted from the literature.[21] Films were treated with a 0.002 M solution of MPA in anhydrous acetonitrile by coating the film surface with the solution, waiting for 2 min, then spin-casting the film for 15 s at 1000 rpm. The films were subsequently washed with anhydrous acetonitrile by spin-coating twice to remove residual quantum dot ligand. Photovoltaic device back contacts of MoO_x (8 nm)/Ag (100 nm) were deposited by consecutive thermal evaporations from a base pressure below 5×10^{-7} Torr. Individual pixels were defined by a shadow mask.

PIA Measurements. PIA spectra were acquired using standard lock-in techniques as discussed in detail elsewhere.[2] Briefly, a 447 nm light-emitting diode (LED; Luxeon Rebel, 700 mA, LXML-PR01) with a home-built driver circuit was used as the excitation source and was electronically modulated by transistor circuit gated by an Agilent 33120A arbitrary waveform generator. The excitation source was modulated at 200 Hz. A monochromated 100 W tungsten halogen lamp was used as the probe beam, which was detected via a Si/InGaAs dual-band photodetector (Thorlabs, DSD2) with sensitivity from the visible to the near-IR (500–1700 nm). A Stanford Research Systems lock-in amplifier (SR830) was used to detect the small fractional changes in the probe beam (dT), which are reported normalized to the probe transmission (T) as dT/T values. The phase of the lock-in was set such that scattered LED pump light appeared entirely as a positive signal in the x-channel. Thus, a fast absorption induced by the pump appears as a negative dT/T signal in the x-channel. Corrections were made to subtract any film photoluminescence (PL) or scattered pump light from the PIA spectra by acquiring data with the probe beam blocked at each wavelength. The PL spectra were collected in parallel with the PIA data, using an automated shutter to block the probe light.

Device Measurements. All photovoltaic measurements were conducted under dynamic

vacuum of approximately 20 mTorr. *I–V* curves and photocurrent spectra were measured using a Keithley 2400 source measure unit. Photocurrent spectra were collected using a 100 W tungsten-halogen bulb (Oriel) passed through a monochromator (Acton 2150). Calibrated silicon (OSI optoelectronics) and InGaAs (Thorlabs) photodetectors were used to calculate external quantum efficiencies. The device pixels and the calibrated photodiode were masked to identical 1.22 mm^2 active areas. Light *I–V* curves were collected under illumination of AM 1.5 G light from a solar simulator (Solar Light Co. model 16S-300).

Results and Discussion

We investigated BHJ blends of PbS QDs with the low band gap polymer PTB1 ($E_g^{opt} \approx$ 1.6 eV).[31] Figure 1a shows the absorbance and photoluminescence (PL) spectra of neat PTB1 (the chemical structure in the inset). Figure 1b shows the absorbance spectra of the different sized PbS QDs used in this study, while Figure 1c shows the approximate energy level positions for all materials as estimated from literature reports.[31-33] Although there may be systematic shifts between solution (electrochemical) and solid-state measurements for the positions of these energy levels,[32] the qualitative size dependence of the energy levels is what is important for our measurements here. The driving force for charge separation via photoinduced electron transfer from the excited polymer to the QDs is determined by the energy difference between the excited-state ionization potential (IP*) of the donor polymer and the ground-state electron affinity of the QD acceptor,[34] and will decrease as the QD size decreases (QD band gap increases). Conversely, the driving force for charge separation via photoinduced hole transfer from an excited QD is determined by the energy offset between the QD valence band and the ground-state IP of the polymer,[34] and will decrease as the QD size increases. In either case, the offset at the valence band edge is much smaller than the offset at the conduction band edge at least using the values shown in Figure 1.[31-33]

We used photoinduced absorption (PIA) spectroscopy to screen for the generation of long-lived charged species, such as polymer polarons, in BHJ composites of PTB1 and PbS QDs. The quantum dots first underwent a solution-phase ligand exchange with butylamine (BA). This treatment removes excess oleate and helps facilitate spin-coating of a mixed polymer/QD solution. We then prepared each film by spin coating a PTB1/PbS QD blend solution at a ratio of 1:9 (w/w). A postdeposition ligand exchange with 3-mercaptopropionic acid (MPA) was subsequently performed on the films as described in the Experimental Methods. The motivation for using this two-step ligand exchange is that devices using QDs that first underwent treatment with butylamine show significantly improved photocurrent generation as compared to devices made with oleate-capped PbS quantum dots that undergo the same MPA postdeposition ligand

exchange but without butylamine exchange (Appendix 1: Figure S1). MPA treatment has been shown to improve carrier mobility and decrease carrier trapping in PbS assemblies[21] and thus is expected to improve carrier collection. In our case, the postdeposition MPA treatment may improve both charge generation at the donor/acceptor interface and charge transport in the QD phase.

Figure 2 shows the PIA spectra of polymer/QD blend films at room temperature with varying sizes of PbS QDs. The signal magnitudes are scaled by the absorbed photon flux at the excitation wavelength (Φ_{Abs} with unit of mol cm^{-2} s^{-1}). The PTB1/PbS blend with QD band gap at 1.28 eV shows a broad photoinduced absorption feature below the polymer band gap at ∽1.1 eV. We attribute this broad absorption feature to long-lived polarons on the PTB1 polymer chains, consistent with the PIA spectra of a PTB1/fullerene blend (Appendix 1 Figure S2).

The PIA spectra of blends with 1.13 and 0.92 eV band gap QDs appear similar. However, the polaron absorption is partly obscured by the overlapping ground-state bleach of the quantum dot first excitonic transition as indicated in Figure 2 (black arrows). The polaron feature appears to decrease for the larger dot sizes; however, the QD bleach obscures the signal considerably, making qualitative analysis difficult. Nevertheless, the largest dots, with the least bleaching interference in the polaron band over ∽1.0–1.6 eV, also show the smallest photoinduced absorption due to the polaron, consistent with this film having the lowest photocarrier yield.

Although the data in Figure 2 suggest that the largest QDs are leading to the least amount of long-lived photoinduced charge generation, we performed additional PIA experiments to clarify this trend. To do this experiment, we removed most of the interference between the polymer polaron peak and the QD absorption bleach. Because the bleach signal in QDs arises primarily due to state blocking,[35,36] rather than depletion of the ground state, charged QDs with the carriers residing in traps show much less bleach signal than dots with carriers in delocalized states.[37] We exploit this effect by performing spectroscopy using butylamine-exchanged dots without the MPA-treatment (as MPA is known to remove carrier traps) to allow QD/polymer charge transfer while suppressing the QD bleach.

To this end, Figure 3 compares the effect of QD size on the PIA spectra of PTB1/PbS films with no postdeposition MPA-treatment (which thus show less interference from the PbS bleach signal). Now, the PIA signal clearly diminishes with decreasing QD band gap, with the polaron signal being the largest for the 1.25 eV dots, smallest (almost nonexistent) for the 0.90 eV dots, and decreasing monotonically in between. The data in Figure 3 represent one of the central results of this article, that the yield of charge carriers measured with PIA decreases with

increasing QD size (decreasing QD band gap) in PTB1/PbS blends. Indeed, virtually no long-lived polaron signal is seen in the blend of PTB1 with the 0.90 eV band gap quantum dots. As discussed below, the device data from solar cells made with blends of PTB1 and PbS QDs are consistent with this conclusion. While the size-dependent charge transfer has been reported at QD/TiO_2 interfaces,[38] it is far rarer in polymer/QD blends.[2]

Next, we consider the effect of quantum dot size on the efficiency of solar cells made with blends of PTB1 and PbS quantum dots. Figure 4a shows the *J–V* curves of photovoltaic devices with the device structure shown in the inset (ITO/ZnO/active layer/MoOx/Ag). The active layer of each device was treated with MPA via the same procedure as that for the films shown in Figure 2. Notably, the devices made from the largest quantum dots have the lowest J_{SC} values, despite having a broader absorption spectrum. Figure 4b shows the external quantum efficiency (EQE) spectra for the same devices. The spectral photocurrent is collected with significant efficiency from both components of the blend film and is dominated by the polymer absorption peak (~2.0 eV) and the quantum dot absorption (<1.5 eV).

Comparing hybrid devices fabricated from PbS QDs with band gaps of 1.32, 1.23, 1.12, and 1.02 eV (Figure 4b), we observe that the EQEs are lowest for the devices made from the largest quantum dots, consistent with the *J–V* curves in Figure 4a, and in good qualitative agreement with the decreasing carrier yields shown in Figures 2 and 3. Interestingly, the largest decrease in quantum efficiency seems to originate from the polymer region, especially at the polymer absorption peak. Figure 4a and Table 1 show the *J–V* characteristics of PTB1/PbS blends after MPA treatment, measured under AM1.5G illumination at 100 mW/cm^2. The FF and V_{OC} do not appear to correlate strongly with QD band gap, despite the clear correlation of decreasing J_{SC} with increasing quantum dot band gap. Devices using 1.32 eV band gap QDs exhibited the best device performance with a J_{SC} of 15.8 mA/cm^2, a V_{OC} of 0.49 V, and a FF of 36%, giving an overall PCE of 2.8%. While the trend of decreasing J_{SC} with decreasing QD band gap is qualitatively consistent with the PIA data, we note that even the devices with the largest QDs still produce photocurrents with EQEs of up to ~30% even though very little PIA signal is observed for those blends. Given that the EQE at the QD absorption peak is insensitive to QD size, while the EQE at the polymer peak is size-dependent, we speculate that these blends may be operating partially as QD Schottky diode cells, in parallel with a polymer/QD bulk heterojunction. This hypothesis would explain both the size-dependent EQE and the PIA spectra, as well as the relative insensitivity of the IR photocurrent peak to the QD size (the Schottky diode current being independent of charge transfer at the polymer/QD interface).

In summary, we have studied charge generation in hybrid solar cells consisting of the conjugated polymer PTB1 with PbS quantum dots of various sizes. When using smaller PbS QDs (e.g., PbS QDs with band gaps of 1.32 eV), these solar cells exhibit EQE's of over 70%

and power conversion efficiencies of 2.8%, comparable to some of the better polymer/PbS blends so far reported.[8,9,13] However, when larger quantum dots are used, the J_{SC} drops significantly due predominantly to a decrease in the EQE in the region of the spectrum where the polymer dominates the film absorption. This size-dependent decrease in EQE agrees well with our PIA data, which show a significant reduction in the population of long-lived positive charge carriers on the polymer when larger PbS QDs are used. We thus conclude that PTB1/PbS solar cells are operating, at least in part, as bulk heterojunction solar cells, and we interpret the reduction in long-lived charge as resulting from the changing energy level offset at the polymer/QD interface. Such strongly size-dependent quantum yields in conjugated polymer/QD blends are relatively rare; indeed early studies of polymers and CdSe quantum dots looked for such an effect but were unable to find significant differences based on QD sizes.[2] Future studies should examine whether these size-dependent changes in long-lived photogenerated charge yield arise from changes in driving force for the initial electron or hole transfer event, or rather from size-dependent changes in back transfer/recombination rates.

Figures for Chapter4:

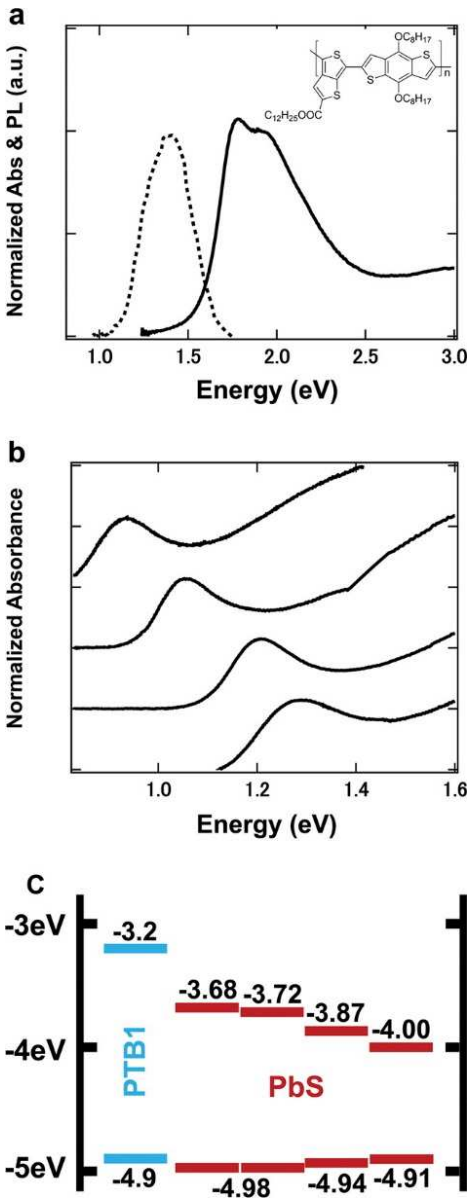

Figure 1 (a) Absorption (solid line), photoluminescence (dotted line), and the chemical structure of the polymer PTB1. (b) Absorption spectra for different sizes of PbS quantum dots (QDs) suspended in tetrachloroethylene showing the size-tunability of the quantum dot band gap. (c) Energy levels for the PTB1 polymer and varying sizes of PbS quantum dots reported from the literature using cyclic voltammetry (CV) or photoelectron spectroscopy in air (PESA). Energy levels for the PTB1 polymer and the PbS QDs are estimated according to refs 31, 32, and 33.

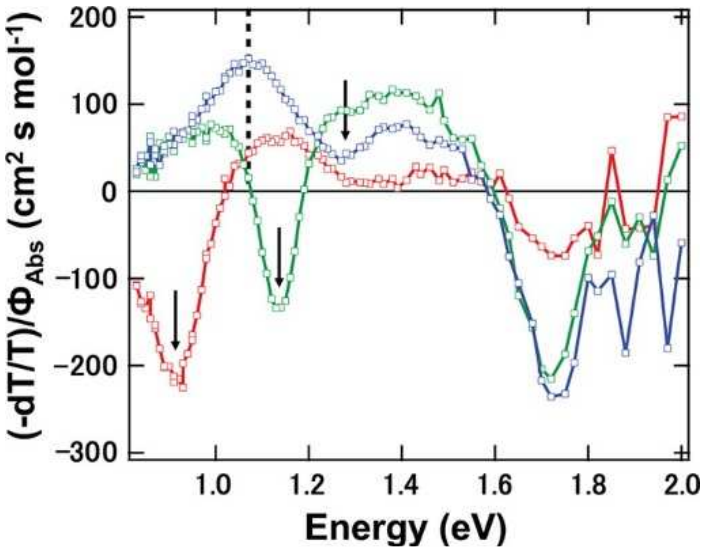

Figure 2 Photoinduced absorption (PIA) spectra (X-channel) of MPA-treated PTB1/PbS QD blends with varying QD band gaps: 1.28 eV (blue), 1.13 eV (green), and 0.92 eV (red). PIA spectra were scaled by the absorbed photon flux (Φ_{Abs}) under 2.77 eV excitation. The arrows indicate PbS quantum dot bleaches, and the black dotted line indicates polymer polaron absorption.

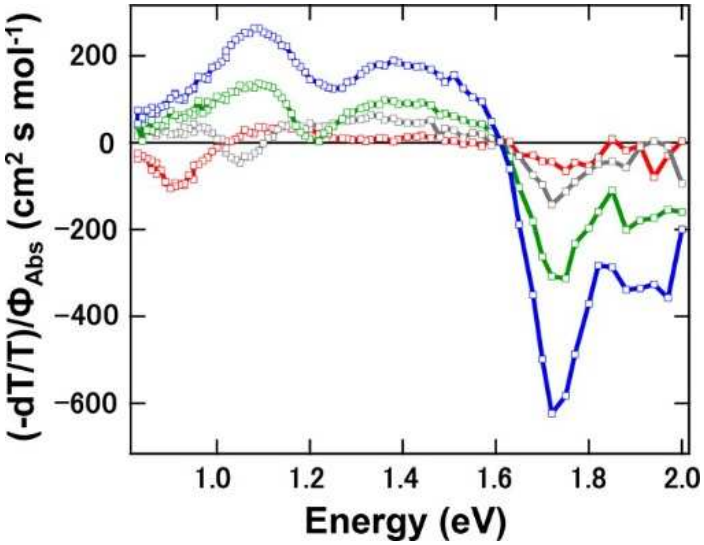

Figure 3 X-Channel (in-phase) photoinduced absorption spectra of polymer/PbS QDs blends with varying QD band gaps, 1.25 eV (blue), 1.22 eV (green), 1.05 eV (gray), and 0.90 eV (red) (butylamine treated). PIA spectra were scaled by the absorbed photon flux (Φ_{Abs}) under 2.77 eV excitation

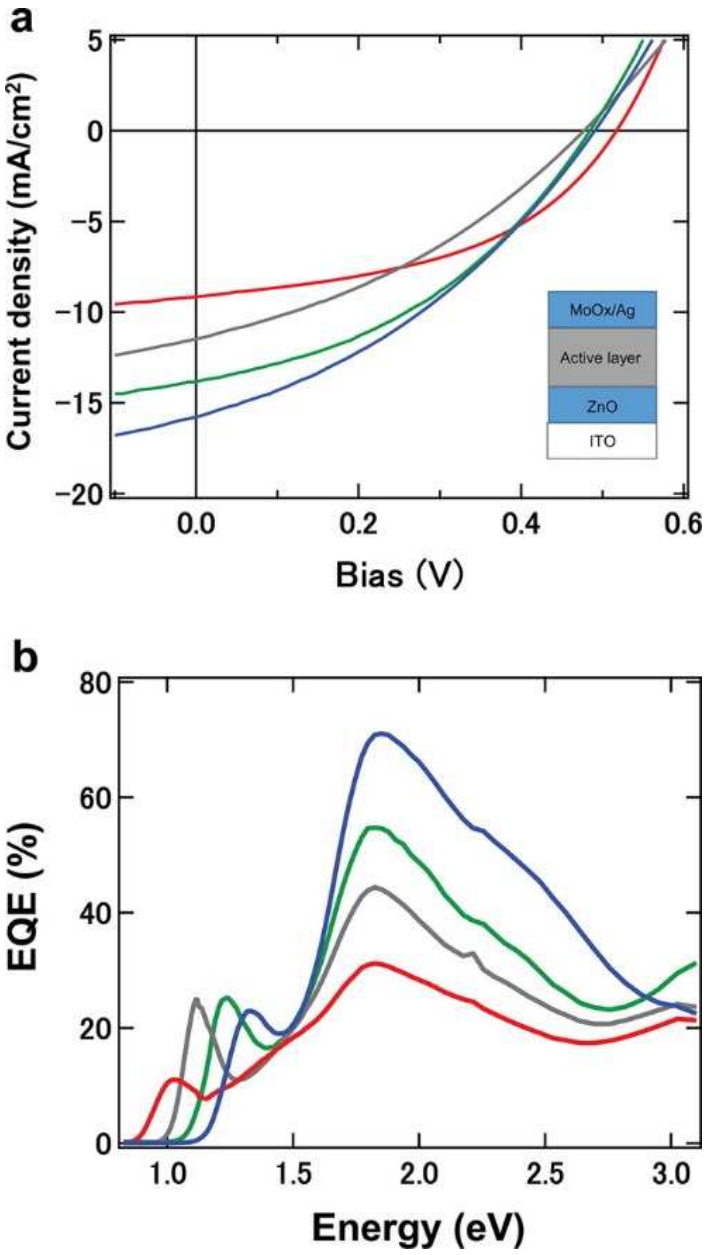

Figure 4 (a) *J–V* curves of MPA treated PTB1/PbS QDs as a function of the band gap of QDs using 1.32 eV (blue), 1.23 eV (green), 1.12 eV (gray), and 1.02 eV (red) QDs. The inset shows the device structure: ITO/ZnO/active layer/MoOx/Ag. (b) External quantum efficiency of MPA-treated PTB1/PbS QDs photovoltaic devices as a function of the QD band gap

Table 1. Summary of Device Performance in MPA-Treated PTB1/PbS Photovoltaics as a Function of the QDs Band Gap

Band gap (eV)	Voc (V)	Jsc (mA/cm^2)	FF	PCE (%)	Estimated Jsc (mA/cm^2)
1.32	**0.49 ± 0.01**	**15.8 ± 0.6**	**0.36 ± 0.01**	**2.77 ± 0.13**	**15.8 ± 0.5**
1.23	**0.48 ± 0.01**	**13.8 ± 0.4**	**0.40 ± 0.01**	**2.66 ± 0.12**	**13.4 ± 0.3**
1.12	**0.48 ± 0.02**	**11.5 ± 0.3**	**0.35 ± 0.01**	**1.93 ± 0.07**	**11.6 ± 0.3**
1.02	**0.52 ± 0.02**	**9.2 ± 0.5**	**0.46 ± 0.02**	**2.20 ± 0.27**	**9.2 ± 0.6**

Estimated J_{sc} is calculated from the EQE spectra. The data are the averages and standard deviations of 6 pixels.

Acknowledgements

This work was supported by the U.S. Department of Energy, Office of Basic Energy Sciences, Division of Material Sciences, under Award DE-FG02-07ER46467. We thank JNC Corp. for an unrestricted gift, which was used to support H.N. M.S. acknowledges a fellowship from the Portuguese Foundation for Science and Technology (FCT) (SFRH/BPD/71816/2010). C.W.S. was supported by the National Science Foundation SEES fellowship (DMR-1215753).

Notes and References

See Appendix 1 for Additional figures: EQE of PTB1/PbS devices with different ligand exchange in Figure S1. X-Channel PIA data for neat PTB1, neat PbS quantum dots, PTB1/PbS blend, and PTB1/PC71BM blend in Figure S2. Effect of MPA ligand on photoluminescence of solid QD films in Figure S3. Photoluminescence quenching in polymer/QD blends in Figure S4. Photoluminescence excitation data in Figure S5.

(1) Greenham, N.; Peng, X.; Alivisatos, A. Charge separation and transport in conjugated-polymer/semiconductor-nanocrystal composites studied by photoluminescence quenching and photoconductivity. *Phys. Rev. B* **1996**, *54*, 17628−17637.

(2) Ginger, D.; Greenham, N. Photoinduced electron transfer from conjugated polymers to CdSe nanocrystals. *Phys. Rev. B* **1999**, *59*, 10622−10629.

(3) Noone, K.; Strein, E.; Anderson, N.; Wu, P.; Jenekhe, S.; Ginger, D. Broadband absorbing bulk heterojunction photovoltaics using low-bandgap solution-processed quantum dots. *Nano Lett.* **2010**, *10*, 2635−2639.

(4) Noone, K.; Subramaniyan, S.; Zhang, Q.; Cao, G.; Jenekhe, S.; Ginger, D. Photoinduced

charge transfer and polaron dynamics in polymer and hybrid photovoltaic thin films: Organic vs inorganic acceptors. *J. Phys. Chem. C* **2011**, *115*, 24403−24410.
(5) Dayal, S.; Kopidakis, N.; Olson, D.; Ginley, D.; Rumbles, G. Photovoltaic devices with a low band gap polymer and CdSe nanostructures exceeding 3% efficiency. *Nano Lett.* **2010**, *10*, 239−242.
(6) Strein, E.; Colbert, A.; Subramaniyan, S.; Nagaoka, H.; Schlenker, C. W.; Janke, E.; Jenekhe, S. A.; Ginger, D. S. Charge generation and energy transfer in hybrid polymer/infrared quantum dot solar cells. *Energy Environ. Sci.* **2013**, *6*, 769−775.
(7) Colbert, A.; Janke, E.; Hsieh, S.; Subramaniyan, S.; Schlenker, C.; Jenekhe, S.; Ginger, D. Hole transfer from low band gap quantum dots to conjugated polymers in organic/inorganic hybrid photovoltaics. *J. Phys. Chem. Lett.* **2013**, *4*, 280−284.
(8) Zhang, Y.; Li, Z.; Ouyang, J.; Tsang, S.; Lu, J.; Yu, K.; Ding, J.; Tao, Y. Hole transfer from PbS nanocrystal quantum dots to polymers and efficient hybrid solar cells utilizing infrared photons. *Org. Electron.* **2012**, *13*, 2773−2780.
(9) Seo, J.; Cho, M.; Lee, D.; Cartwright, A.; Prasad, P. Efficient heterojunction photovoltaic cell utilizing nanocomposites of lead sulfide nanocrystals and a low-bandgap polymer. *Adv. Mater.* **2011**, *23*, 3984−3988.
(10) Greaney, M.; Das, S.; Webber, D.; Bradforth, S.; Brutchey, R. Improving open circuit potential in hybrid P3HT:CdSe bulk heterojunction solar cells via colloidal tert-butylthiol ligand exchange. *ACS Nano* **2012**, *6*, 4222−4230.
(11) ten Cate, S.; Schins, J.; Siebbeles, L. Origin of low sensitizing efficiency of quantum dots in organic solar cells. *ACS Nano* **2012**, *6*, 8983−8988.
(12) Jarzab, D.; Szendrei, K.; Yarema, M.; Pichler, S.; Heiss, W.; Loi, M. Charge-separation dynamics in inorganic-organic ternary blends for efficient infrared photodiodes. *Adv. Funct. Mater.* **2011**, *21*, 1988−1992.
(13) Piliego, C.; Manca, M.; Kroon, R.; Yarema, M.; Szendrei, K.; Andersson, M.; Heiss, W.; Loi, M. Charge separation dynamics in a narrow band gap polymer-PbS nanocrystal blend for efficient hybrid solar cells. *J. Mater. Chem.* **2012**, *22*, 24411−24416.
(14) Lee, M.; Teuscher, J.; Miyasaka, T.; Murakami, T.; Snaith, H. Efficient hybrid solar cells based on meso-superstructured organometal halide perovskites. *Science* **2012**, *338*, 643−647.
(15) Stranks, S.; Eperon, G.; Grancini, G.; Menelaou, C.; Alcocer, M.; Leijtens, T.; Herz, L.; Petrozza, A.; Snaith, H. Electron-hole diffusion lengths exceeding 1 micrometer in an organometal trihalide perovskite absorber. *Science* **2013**, *342*, 341−344.
(16) Strein, E.; deQuilettes, D.; Hsieh, S.; Colbert, A.; Ginger, D. Hot hole transfer increasing polaron yields in hybrid conjugated polymer/PbS blends. *J. Phys. Chem. Lett.* **2014**, *5*, 208−211.
(17) Knesting, K.; Ju, H.; Schlenker, C.; Giordano, A.; Garcia, A.; Smith, O.; Olson, D.; Marder,

S.; Ginger, D. ITO interface modifiers can improve Voc in polymer solar cells and suppress surface recombination. *J. Phys. Chem. Lett.* **2013**, *4*, 4038−4044.

(18) Ellingson, R.; Beard, M.; Johnson, J.; Yu, P.; Micic, O.; Nozik, A.; Shabaev, A.; Efros, A. Highly efficient multiple exciton generation in colloidal PbSe and PbS quantum dots. *Nano Lett.* **2005**, *5*, 865−871.

(19) Stewart, J.; Padilha, L.; Qazilbash, M.; Pietryga, J.; Midgett, A.; Luther, J.; Beard, M.; Nozik, A.; Klimov, V. Comparison of carrier multiplication yields in PbS and PbSe nanocrystals: The role of competing energy-loss processes. Nano Lett. 2012, 12, 622−628.

(20) Nozik, A. Nanoscience and nanostructures for photovoltaics and solar fuels. *Nano Lett.* **2010**, *10*, 2735−2741.

(21) Jeong, K.; Tang, J.; Liu, H.; Kim, J.; Schaefer, A.; Kemp, K.; Levina, L.; Wang, X.; Hoogland, S.; Debnath, R.; Brzozowski, L.; Sargent, E.; Asbury, J. Enhanced mobility-lifetime products in PbS colloidal quantum dot photovoltaics. *ACS Nano* **2012**, *6*, 89−99.

(22) Tang, J.; Kemp, K.; Hoogland, S.; Jeong, K.; Liu, H.; Levina, L.; Furukawa, M.; Wang, X.; Debnath, R.; Cha, D.; Chou, K.; Fischer, A.; Amassian, A.; Asbury, J.; Sargent, E. Colloidal-quantum-dot photovoltaics using atomic-ligand passivation. *Nat. Mater.* **2011**, *10*, 765−771.

(23) Koster, L.; Shaheen, S.; Hummelen, J. Pathways to a new efficiency regime for organic solar cells. *Adv. Energy Mater.* **2012**, *2*, 1246−1253.

(24) Li, Z.; Gao, F.; Greenham, N.; McNeill, C. Comparison of the operation of polymer/fullerene, polymer/polymer, and polymer/nanocrystal solar cells: A transient photocurrent and photovoltage study. *Adv. Funct. Mater.* **2011**, *21*, 1419−1431.

(25) Zhou, R.; Stalder, R.; Xie, D.; Cao, W.; Zheng, Y.; Yang, Y.; Plaisant, M.; Holloway, P.; Schanze, K.; Reynolds, J.; Xue, J. Enhancing the efficiency of solution-processed polymer:colloidal nanocrystal hybrid photovoltaic cells using ethanedithiol treatment. *ACS Nano* **2013**, *7*, 4846−4854.

(26) You, J.; Dou, L.; Yoshimura, K.; Kato, T.; Ohya, K.; Moriarty, T.; Emery, K.; Chen, C.; Gao, J.; Li, G.; Yang, Y. A polymer tandem solar cell with 10.6% power conversion efficiency. *Nat. Commun.* **2013**, *4*, 1446.

(27) Ip, A.; Thon, S.; Hoogland, S.; Voznyy, O.; Zhitomirsky, D.; Debnath, R.; Levina, L.; Rollny, L.; Carey, G.; Fischer, A.; Kemp, K.; Kramer, I.; Ning, Z.; Labelle, A.; Chou, K.; Amassian, A.; Sargent, E. Hybrid passivated colloidal quantum dot solids. *Nat. Nanotechnol.* **2012**, *7*, 577−582.

(28) Guo, Q.; Ford, G.; Yang, W.; Hages, C.; Hillhouse, H.; Agrawal, R. Enhancing the performance of CZTSSe solar cells with Ge alloying. *Sol. Energy Mater. Sol. Cells* **2012**, *105*, 132−136.

(29) Hines, M.; Scholes, G. Colloidal PbS nanocrystals with sizetunable near-infrared emission: Observation of post-synthesis selfnarrowing of the particle size distribution. *Adv. Mater.* **2003**, *15*, 1844−1849.
(30) Sun, B.; Sirringhaus, H. Solution-processed zinc oxide fieldeffect transistors based on self-assembly of colloidal nanorods. *Nano Lett.* **2005**, *5*, 2408−2413.
(31) Liang, Y.; Wu, Y.; Feng, D.; Tsai, S.; Son, H.; Li, G.; Yu, L. Development of new semiconducting polymers for high performance solar cells. *J. Am. Chem. Soc.* **2009**, *131*, 56−57.
(32) Jasieniak, J.; Califano, M.; Watkins, S. Size-dependent valence and conduction band-edge energies of semiconductor nanocrystals. *ACS Nano* **2011**, *5*, 5888−5902.
(33) Moreels, I.; Lambert, K.; Smeets, D.; De Muynck, D.; Nollet, T.; Martins, J.; Vanhaecke, F.; Vantomme, A.; Delerue, C.; Allan, G.; Hens, Z. Size-dependent optical properties of colloidal PbS quantum Ddots. *ACS Nano* **2009**, *3*, 3023−3030.
(34) Ren, G.; Schlenker, C.; Ahmed, E.; Subramaniyan, S.; Olthof, S.; Kahn, A.; Ginger, D.; Jenekhe, S. Photoinduced hole transfer becomes suppressed with diminished driving force in polymer-fullerene solar cells while electron transfer remains active. *Adv. Funct. Mater.* **2013**, *23*, 1238−1249.
(35) Ginger, D.; Dhoot, A.; Finlayson, C.; Greenham, N. Long-lived quantum-confined infrared transitions in CdSe nanocrystals. *Appl. Phys. Lett.* **2000**, *77*, 2816−2818.
(36) Houtepen, A.; Vanmaekelbergh, D. Orbital occupation in electron-charged CdSe quantum-dot solids. *J. Phys. Chem. B* **2005**, *109*, 19634−19642.
(37) Shim, M.; Wang, C.; Guyot-Sionnest, P. Charge-tunable optical properties in colloidal semiconductor nanocrystals. *J. Phys. Chem. B* **2001**, *105*, 2369−2373.
(38) Robel, I.; Kuno, M.; Kamat, P. Size-dependent electron injection from excited CdSe quantum dots into TiO2 nanoparticles. *J. Am. Chem. Soc.* **2007**, *129*, 4136−4137.

Chapter 5:

Zr-doped TiO_2 Electrodes Reduce Hysteresis and Improve Performance in Hybrid Perovskite Solar Cells while Increasing Carrier Lifetimes

Hirokazu Nagaoka, Fei Ma, Dane W. deQuilettes, Sarah M. Vorpahl, Micah S. Glaz, Adam E. Colbert, Mark Ziffer and David S. Ginger.

Abstract

We investigate the effect of zirconium (Zr) doping into the titanium dioxide (TiO_2) electron transporting layer commonly used in hybrid organometal halide perovskite solar cells. We find that, compared to Zr-free controls, solar cells employing Zr-doped TiO_2 (Zr-TiO_2) give rise to an increase in overall power conversion efficiency, and a decrease in hysteresis. While fill factor (FF), open circuit voltage (V_{oc}) and short circuit current density (J_{sc}) all improve with Zr-TiO_2 electrodes, the relative changes in FF are largest. We use transient photovoltage and photocurrent extraction to measure charge carrier lifetimes and densities as a function of light intensity for devices prepared with and without Zr incorporated into the TiO_2 layer. We observe longer carrier lifetimes and higher charge carrier densities in devices on Zr-TiO_2 electrodes at microsecond times in transient photovoltage experiments, as well as at longer persistent photovoltages extending from ~millisecond to tens of sec. We characterize the surface stoichiometry, change in work function and reduction potential of the TiO_2 upon incorporation of Zr, and discuss the charge recombination at the perovskite TiO_2 interface in the context of these variables. Finally, we characterize the combined effects of pyridine treatment and Zr-TiO_2 on device performance and carrier lifetimes. We find that pyridine-treatment and Zr-modification of the electrodes exhibit complicated competing effects on the lifetimes, but that devices with Zr-TiO_2 electrodes and pyridine treatment show even better performance than either modification on their own.

Introduction:

Organometal halide perovskite semiconductors of the chemical formula $CH_3NH_3PbX_3$ (X= Cl, Br, I) have attracted the interest of many scientists working on thin film photovoltaics (PV) due to their low cost, potential ease of processing, and efficient performance.[1, 2] The device performance of perovskite solar cells already reached 19% within just a few years.[3-6] These successes have been achieved by optimizing the device architecture[5, 7] the perovskite layers[8, 9] and the carrier transport layers.[4, 10] The high device efficiencies have been attributed to long carrier lifetimes and large transport lengths,[11, 12] high charge-carrier mobilities,[13] as well as their

high dielectric constants.[14]

However, despite their high efficiencies, most reported planar heterojunction perovskite devices exhibit hysteresis in their current-voltage curves.[15-17] Snaith and co-workers have speculated that these hysteresis effects might result from charge carrier trapping/detrapping in the defects of perovskite itself, at interfaces between perovskite and charge collection layers, or even as a result of ion migration or ferroelectric properties.[15] In addition, Baumann et al. recently observed persistent photovoltages at longer timescales (several tens of seconds) in perovskite ($CH_3NH_3PbI_3$) devices during transient photovoltage (TPV) experiments.[18] They argued that the persistent photovoltage could result from a number of possibilities, including the back transfer of electrons or holes that are populated in the transporting layer into perovskite, or slow detrapping of carriers possibly due to the presence of defects and grain boundaries within the perovskite film or at the transport layer interfaces.[18]

The charge transporting layers also play an important role by enhancing selective charge collection in the efficient perovskite solar cells. N-type metal oxide materials such as TiO_2 and ZnO, are widely used in most studies[5, 19] because they can help prevent shunting and reduce leakage currents under reverse bias.[20] Others have shown how manipulating the interfacial chemistry at the electrodes can have a beneficial effect on both overall performance, and hysteresis.[19, 21]

Tailoring the metal oxide layer is an approach that has been pursued across a number of photovoltaic technologies, as it can offer advantages such as optimized energy levels, more favorable surface energies, or increased carrier concentrations, resulting in enhanced performance.[4,10] Doping of metal oxides has also been used to decrease interfacial recombination.[22, 23] The use of mixed zirconium-titania (Zr-TiO_2) instead of pure TiO_2 has been used successfully in dye-sensitized solar cells and quantum dot solar cells.[24-26] For instance, Liu et al. have reported the performance of PbS quantum dot solar cells was improved by changing energy levels and electron density with zirconium inclusion into the TiO_2.[25] Along with doping of metal oxides, others have shown surface passivation of the perovskite is an interesting technique that remove trap states and surface defects in perovskite.[27, 28] Noel et al have reported that post-deposition pyridine treatments improved device performance, proposing that Lewis base molecules might bind to the under-coordinated Pb ions in the perovskite crystal.[27]

Here, we investigate the effects of zirconium incorporation into titanium dioxide electron transporting layer (ETLs) in organometal halide perovskite solar cells. We find that devices with Zr-TiO_2 electrodes show longer carrier lifetimes and higher charge carrier densities, resulting in improved device performance. We also investigate how the surface chemistry and electronic properties of the Zr-TiO_2 influence device operation. Finally, we study the effect of combining a pyridine treatment of the perovskite with Zr-doping of the TiO_2 on the device performance and

hysteresis of perovskite solar cells and show that the effects are additive.

Results and discussion:

(a)

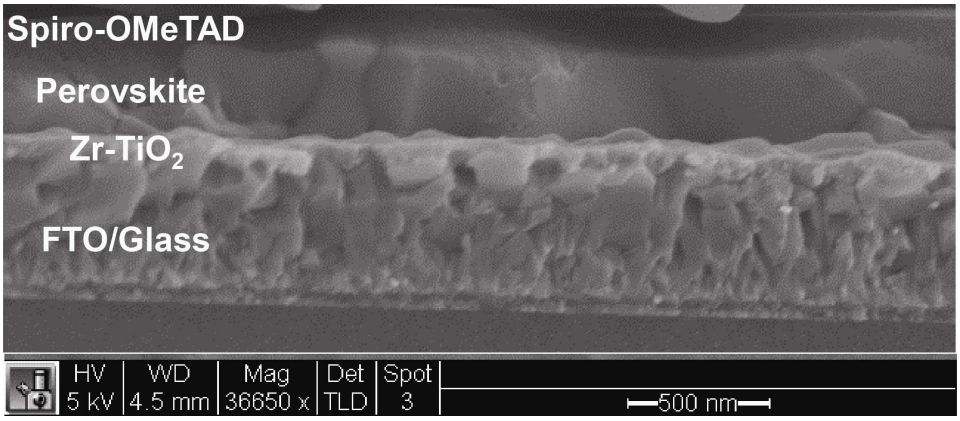

(b) (c)

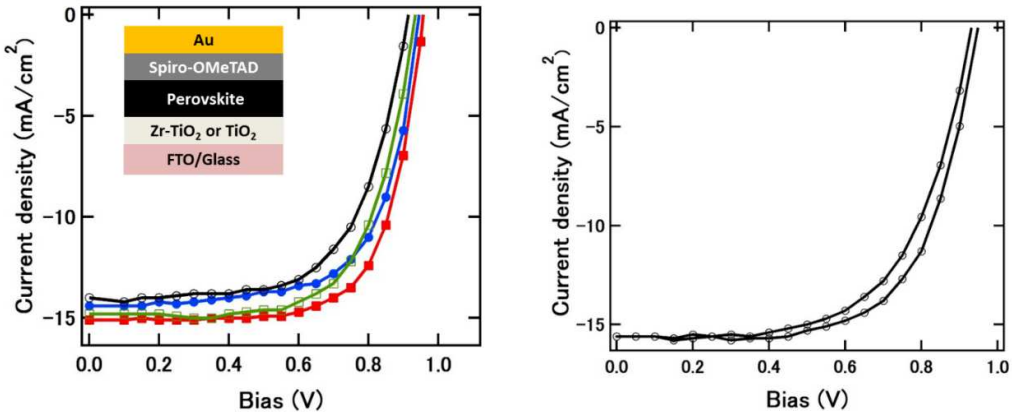

Figure 1 (a) Cross-sectional scanning-electron microscope (SEM) image of a mixed halide perovskite ($CH_3NH_3PbI_{3-x}Cl_x$,) device architecture. (b) J-V curves of devices based Zr-TiO_2 (blue filled circle), TiO_2 (black empty circle), Zr-TiO_2/pyridine treatment (red filled square) and TiO_2/pyridine treatment (green empty square) measured at the scanning rate of 0.15V/s and reverse scan (from open-circuit to short-circuit). The inset shows that the layers in the device from the bottom are: FTO / Zr-TiO_2 or TiO_2/ Perovskite/ Spiro-OMeTAD / Au. (c) Typical J-V curves of devices with Zr-TiO_2 electrodes and pyridine treatment acquired at the scanning rate of 0.15V/s.

Table 1. Summary of average device performance

	Voc (V)	Jsc (mA/cm^2)	FF	PCE (%)
TiO_2	**0.90 ± 0.004**	**14.1 ± 0.25**	**0.62 ± 0.02**	**8.1 ± 0.32**
Zr-TiO_2	**0.93 ± 0.005**	**14.4 ± 0.23**	**0.67 ± 0.01**	**9.1 ± 0.28**
TiO_2/pyridine	**0.93 ± 0.003**	**14.7 ± 0.15**	**0.67 ± 0.01**	**9.2 ± 0.18**
Zr-TiO_2/pyridine	**0.96 ± 0.002**	**14.9 ± 0.08**	**0.69 ± 0.01**	**9.8 ± 0.1**

The values reported are the averages and standard deviations of the mean for 21 pixels from (7 devices) per row.

Figure 1a shows a cross-sectional scanning-electron microscope (SEM) image of a typical perovskite solar cells employing mixed Zirconium/Titanium dioxide TiO_2 (Zr-TiO_2) electrodes. We fabricated p-i-n planar heterojunction perovskite solar cells with the structure: glass / fluorine-doped tin oxide (FTO) / Zr-TiO_2 (or TiO_2) / perovskite / spiro-OMeTAD / Au (fabrication procedures are described in Materials & Methods). We prepared both Zr-free TiO_2 and Zr-doped TiO_2 by sol-gel methods following previous reports.[25] We used a mixed halide perovskite ($CH_3NH_3PbI_{3-x}Cl_x$,) for the active layer, which has a valence band maximum (VBM) and the conduction band minimum (CBM) reported to be -5.3 and -3.75 eV, respectively.[4] We used the standard 2,2′,7,7′-tetrakis-(N,N-di-4-methoxyphenylamino)-9,9′-spirobifluorene (spiro-OMeTAD) and gold as our hole transporting layer and electrode, respectively.

Figure 1b shows the improvements realized with Zr-TiO_2 electrodes by comparing typical JV characteristics of perovskite devices made at the same time using the same active layer solutions, but with different electrodes and post-deposition treatments. We compared Zr-TiO_2 electrodes, TiO_2 electrodes, Zr-TiO_2 electrodes with pyridine treatment, and TiO_2 electrodes with pyridine treatment. Table 1 shows average device performance values across many separate devices, (and many more pixels), that are consistent with the individual devices shown in Figure 1b. Notably, the devices with Zr-TiO_2 electrodes that have undergone pyridine treatment exhibit the highest average device performance with a J_{SC} of 14.9 mA/cm^2, a V_{OC} of 0.96 V, and a FF of 69%, giving an overall PCE of 9.8%. We also found that devices employing both Zr-TiO_2 and pyridine treatments show a decrease in hysteresis compared to the other devices, regardless of scan rate (see device hysteresis data with different scan rates (Figure S1)). Compared to the device with Zr-free TiO_2, we observe that either Zr-doping or pyridine treatment and both of them improves short-circuit current density (J_{sc}), and is confirmed by the external quantum efficiency (Figure S2). We also find an increase in open circuit voltage (V_{oc}) and fill factor (FF) after either Zr-doping or pyridine treatment. In all cases the improvements from using Zr-doped TiO_2 compounded with improvements found from pyridine treatment,

suggesting that these two modifications are affecting complementary aspects of the device performance.

We performed a series of experiments to gain insight into the changes incurred by incorporating Zr into the TiO_2. Using XPS we confirmed that the Ti to Zr atomic ratios at the surface of our Zr-TiO_2 films were 15.7:1 (Figure S5), consistent with, but slightly higher than the growth solution (which had Ti:Zr = 19:1). Using cyclic-voltammetry (CV), we determined the location of the conduction band (CB) edge (Figure S3). Based on the reduction onset, we report small shift in the conduction band edge towards vacuum for our Zr-TiO_2 compared to TiO_2. (-3.82 eV for our Zr-TiO_2 films vs -3.87 eV for our TiO_2 films). We also used scanning Kelvin Probe microscopy (SKPM) to measure changes in surface potential (work function) between Zr-TiO_2 and TiO_2 electrodes (Figure S4). Our data show the work function of Zr-TiO_2 electrodes is 0.18 eV shallower than that of TiO_2 electrodes, consistent with the slightly upward shift in conduction band in Zr-TiO_2 electrodes to vacuum. While relatively minor, these shifts in electron affinity and work function are consistent with the observed improvements in device performance as they could serve to bring the Zr-TiO_2 contact into slightly better alignment with that of the perovskite (reported at -3.75 eV).[4] Nevertheless, we do not think that these shifts alone are responsible for all of the effects of Zr-incorporation.

(a) (b)

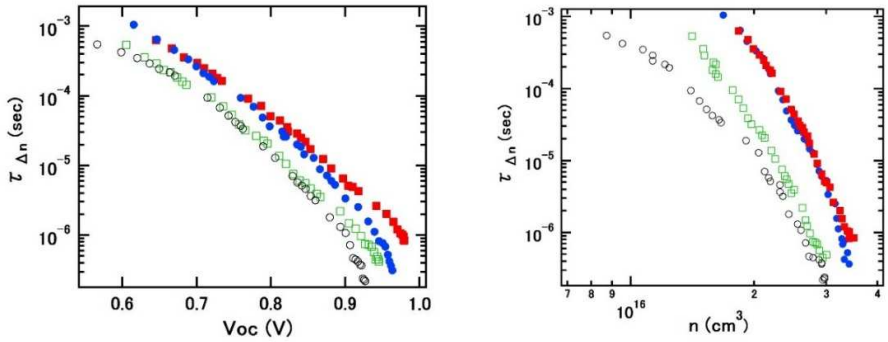

Figure 2 Lifetime of charge carriers at (a) different Voc and (b) different charge carrier density using Zr-TiO_2 (blue filled circle), TiO_2 (black empty circle), Zr-TiO_2/pyridine treatment (red filled square) and TiO_2/pyridine treatment (green empty square).

Therefore, we used transient photovoltage and charge extraction in order gain further insight into the effects of using Zr-doped TiO_2, both with and without pyridine treatments of the perovskite. Transient photovoltage methods can be used to measure the pseudo-first-order decay lifetime ($\tau_{\Delta n}$) of a photovoltage perturbation created by a small transient light source in the presence of a large background carrier population, typically provided by a white light source. Charge extraction (CE) can be used to measure carrier density in a device by shunting a device

and recording the current transient. Together these methods allow for determination of carrier recombination rates at varying carrier densities.[29] The specific details of our experimental configuration are available in the literature.[30] We find that devices incorporating the Zr-doped TiO_2 electrodes show slower voltage decays on timescales spanning nearly 6 orders of magnitude in time regardless of the carrier density. We also find that pyridine treatment increases carrier lifetime at high V_{OC} and high carrier density conditions, but reduces carrier lifetime at low V_{OC} and low carrier density conditions.

Figure 2 plots our TPV and CE data on the different perovskite devices. Figure 2a plots TPV lifetime as a function of V_{OC}, while Figure 2b plots charge carrier lifetime measured with TPV versus charge carrier density through charge extraction (CE) measurement. We observe that the devices with Zr-TiO_2 electrodes show less recombination loss at short times and high carrier densities compared to the device with Zr-free TiO_2 electrodes. In organic solar cells, TPV decays as these fast times are typically associated with non-geminate recombination of carriers in devices,[29] an interpretation which has been advanced for TPV data on the perovskites as well.[28] The slower TPV decays for solar cells using the Zr-TiO_2 electrodes would thus be consistent with the observed higher V_{OC} and FF for these devices. The increase in lifetime could be due to reduced interfacial recombination between Zr-TiO_2 electrodes and perovskite, either because of a reduction in interfacial states because of the Zr surface chemistry, or because the shallower work function of the Zr-TiO_2 permits a slightly more favorable surface field in the perovskite, thus reducing the hole concentration near the electron-extracting contact. Similar phenomena have been reported in OPV devices.[30]

(a) (b)

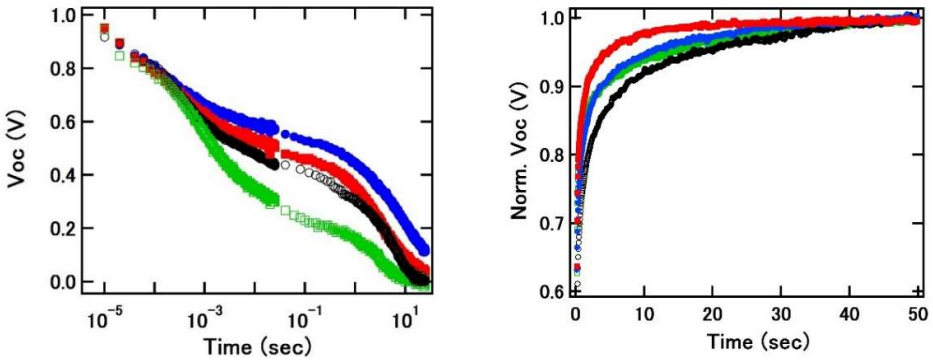

Figure 3 (a) Open circuit voltage transients for the perovskite devices based Zr-TiO_2 (blue filled circle), TiO_2 (black empty circle), Zr-TiO_2/pyridine treatment (red filled square) and TiO_2/pyridine treatment (green empty square). (b) Photovoltage rise times under 118 W/cm^2 white LED illumination showing normalized photovoltage as a function of time after the light was turned on (same symbols). Photovoltage for each devices was normalized at 50 s in (b).

Baumann et al. have previously reported long persistent photovoltages in hybrid perovskite solar cells. Although the origin of these persistent photovoltages was unclear, they speculated that the perovskite/TiO_2 interface might play an important role. We thus also explored the effects of Zr-doping of the electrode and pyridine treatment of the active layer on long time persistent photovoltages, as well as on the rise time of the photovoltage following illumination of the devices.

Figure 3a shows open circuit voltage transients for the perovskite devices based Zr-TiO_2, TiO_2, Zr-TiO_2/pyridine treatment and TiO_2/pyridine treatment. In these experiments, the devices were held at simulated 1-sun illumination with a white LED until the open circuit voltage plateaued, then the light was abruptly turned off and the V_{OC} was recorded as a function of time. We observe persistent photovoltage decays spanning timescales from ~10^{-5}-10 s, consistent with those reported previously for planar $CH_3NH_3PbI_3$ solar cells.[18] Interestingly, we find more persistent photovoltage on timescales of ~10^{-3}-10 s in devices with Zr-TiO_2 electrodes, yet we see faster photovoltage decays in devices with pyridine treatment on timescales of ~10^{-3}-10 s. We also measured the photovoltage transients with three different illumination intensities for each sample (Figure S6). Figure 3b shows transient photovoltage rise time for each perovskite devices as a function of time after the light was turned on. We see all devices reach the steady state of open circuit voltage over several tens of seconds. The devices with Zr-TiO_2 electrodes reaches steady state faster when illuminated, and takes longer to decay once the illumination is removed. Notably, if the same simple slow recombination process were governing both rise and decay then one would expect both be shorter or both be faster. We therefore interpret these results as indicating that the long time voltage decays do not result from a single simple recombination process.

Following the hypothesis of Baumen et al.,[18] the long and short phases of photovolatage decay dynamics (Figure 3a) might be the result of components of recombination that are caused by carriers that are populated in the perovskite (fast recombination) and back transfer of electrons or holes that are populated in the transporting layer into perovskite (slow recombination).[18] The longer photovoltage decays observed in our devices with Zr-TiO_2 electrodes are consistent with this hypothesis, and would suggest slower back electron transfer from the Zr-TiO_2 into perovskite layer. The faster rise and slower decay could be explained either by traps in the perovskite film (due to different film formation at the Zr-TiO_2 interface) or at the transport layer interface fills more quickly, and empties more slowly in the devices with Zr-TiO_2. For the devices with pyridine treatment, we attribute the faster photovoltage rise and decay to lower trap density due to passivation of defect sites.[27] Therefore, the device with TiO_2 electrodes and pyridine treatment (but without Zr) shows the fastest photovoltage decay.

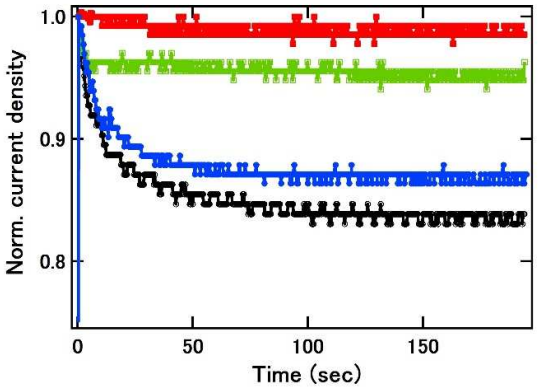

Figure 4 Photocurrent density as a function of time for the perovskite devices with Zr-TiO_2 (blue filled circle), TiO_2 (black empty circle), Zr-TiO_2/pyridine treatment (red filled square) and TiO_2/pyridine treatment (green empty square) held at 0.75V under simulated AM1.5 at 100 mW/cm^2. Photocurrent transients were measured after switching the devices from open circuit to short circuit.

Noel et al. have previously reported pyridine treatment improves the stabilized power output, and might be consistent with hysteresis in hybrid perovskite solar cells. We thus also explored the effects of Zr-inclusion of the electrode and pyridine treatment of perovskite layer on power output at maximum power point. Figure 4 shows photocurrent density as a function of time for each perovskite devices with Zr-TiO_2, TiO_2, Zr-TiO_2/pyridine treatment, and TiO_2/pyridine treatment, held at maximum power point voltage under illumination. We observe the pyridine-treated devices stabilizes photocurrent density under a fixed 0.75 V forward bias. For the untreated devices, the photocurrent density decreases over 10%. We find the device with Zr-TiO_2 electrodes slightly improves photocurrent density loss. Given the smaller effect of the Zr compared to the pyridine, we attribute the photocurrent loss to non-passivated defect sites in perovskite rather than defect sites or the interface with the ETL.[27] Thus, both Zr-doping and pyridine treatment contribute complementary effects to improve device performance and reduced hysteresis.

Conclusion:

In conclusion, we have demonstrated that hybrid organometal halide perovskite solar cells employing Zr-TiO_2 electrodes and pyridine treatment give rise to an increase in overall power conversion efficiency and a decrease in hysteresis. We observe longer carrier lifetimes and higher charge carrier densities in devices on Zr-TiO_2 electrodes at microsecond times in transient photovoltage experiments, as well as at longer persistent photovoltages extending from ~millisecond to tens of sec. Furthermore, we find devices with Zr-TiO_2 electrodes and pyridine

treatment show higher stabilized device performance as well as faster photovoltage rises, indicating reduced defect sites in the perovskite or at the interfaces. We therefore suggest interface modification employing doping of metal oxide or fullerene derivative[21] and passivation of defect sites in the bulk are both strategies that should continue to improve device performance and reduce hysteresis. Furthermore, observing these distinct charge carrier kinetics with different electrodes using microscopic techniques would lead to further investigation of persistent photovoltage and improvement of device studies.[31]

Experimental methods:

Methylammonium iodide. Methylammonium iodide was prepared following a previous report.[2] 24 mL of methylamine solution (0.193 mol, 33% in ethanol, Sigma) was diluted with 100 mL of ethanol. 10 mL aqueous solution of hydriodic acid (0.076 mol, 57 wt% in water, Sigma) was added to this solution under constant stirring. After a reaction time of 1 h at room temperature, the resulting solution was evaporated at 100°C for more than 12 hours. The obtained crude product was washed with dry diethyl ether, and then recrystallized using a mixed solvent of ethanol and ether. Finally the obtained white crystals were dried under vacuum overnight. This white crystalline powder should be stored under a dry nitrogen atmosphere.

Perovskite precursor solution. 0.8 g of dried methylammonium iodide (MAI) and 0.46 g of lead(II) chloride ($PbCl_2$, 99.999%, Alfa Aesar) were dissolved in anhydrous N,N-dimethylformamide (DMF, Sigma) at a 3:1 molar ratio of MAI to $PbCl_2$, with final concentrations 0.83 M lead chloride and 2.5 M methylammonium iodide to form the non-stoichiometric $CH_3NH_3PbI_{3-x}Cl_x$ precursor solution. This solution should be stored under a dry nitrogen atmosphere.

Sol-gel TiO_2. The preparation of sol-gel TiO_2 was carried out in air ambient at room temperature.[26] 5 mL Titanium (IV) n-butoxide (1.43 mmol, 97%, Sigma) was mixed with 4 mL of triethanolamine (98%, Sigma) and 25 mL of anhydrous ethyl alcohol in a flask under continuous magnetic agitation for 1 h, ((where a 0.34 mL of Zirconium (IV) butoxide solution (0.74 mmol, 80 wt. % in 1-butanol, Sigma) would be added for Zr-doped TiO_2 electrodes, Zr/Ti molar ratio being 5%.)) 5 mL of Acetic acid (glacial, Macron Fine Chemicals) and 5 mL of deionized water were then added into the mixture with continuous magnetic agitation for 24 h. The resulting solution was clear and transparent. The solution was filtered through a 0.45 μm PTFE syringe filter prior to spin-coating.

Perovskite solar cells. FTO coated glass sheets (7 Ω/sq, Aldrich) were etched with zinc powder

and HCl (4 M) to obtain the required electrode pattern. The sheets were then washed with soap (2 vol % Micro-90, International Products Corp., in purified deionized water), deionized water, acetone, and isopropanol and finally treated under oxygen plasma for 10 min to remove the last traces of organic residues prior to spin-coating. The sol-gel derived TiO_2 electrodes were coated on FTO substrates using spin-coating with following heat treatment. 60 μL of the sol-gel TiO_2 solution were deposited on the FTO substrates by dynamical spin-coating at 3500 rpm for 1 min, following by heat treatment in air on a hotplate at 500 ºC for 1 hour to achieve full anatase crystallization. To form the perovskite layer for devices, the perovskite precursor solution was spin-coated on the prepared TiO_2 substrates in a nitrogen- filled glovebox, at 2000 rpm for 60 s. After spin-coating, the substrates were left to dry at room temperature in the glovebox for 30 minutes, to allow slow solvent evaporation. They were then annealed on a hotplate in the glovebox at 90°C for 150 minutes, and then heating at 120°C for 15 min. During the annealing procedure at 90°C, the coated substrate changed color from light yellow to dark brown, indicating the formation of the perovskite film. After drying, the substrate was cooled down to room temperature. The substrate was treated with a 0.25 M solution of pyridine in anhydrous chlorobenzene and then the spin-coating the substrate for 1 min at 4000 rpm. The substrate was subsequently covered with Spiro-OMeTAD (Borun Chemicals, 99.47% purity). 96 mg of Spiro-OMeTAD were dissolved in 1 mL of chlorobenzene and mixed with 10 μL 4-*tert* -butylpyridine (*t* BP, 96%, Sigma) and 43 μL of a 175 mg mL^{-1} bis (trifluoromethane) sulfonimide lithium salt (Li-TFSI, 99.95% sigma) solution in acetonitrile. This solution was spincoated at 4000 rpm for 1 min. Before evaporating the gold electrodes, Spiro-OMeTAD was allowed to oxidize in air over night at room temperature in the dessicator. For the counter electrode, a 100 nm-thick Au was deposited on the top of the Spiro-OMeTAD over layer by a thermal evaporation, where Au evaporated with a base pressure below 5×10^{-7} Torr.

J-V characteristics and time-dependent photocurrent measurements. The current density–voltage (J-V) curves were measured using a source meter (Keithley, 2400 Series) under illumination of AM 1.5 G light from a solar simulator (Solar Light Co. model 16S-300) at 100 mW/cm^2 in a nitrogen glovebox. All devices were measured at a scanning rate of 0.15V/s scanning from open-circuit to short-circuit. The device pixels and the calibrated photodiode were masked to identical 1.3 mm^2 active areas. For time-dependent photocurrent measurements, the device was held at maximum power point voltage under simulated AM1.5 at 100 mW/cm^2, and then photocurrent transients were measured at maximum power point after switching the devices from open circuit to short circuit under illumination. Maximum power point was extracted from JV curves measured at reverse scan (from open circuit to short circuit).

Transient Photovoltage and Charge Extraction Measurements. TPV and CE measurements were performed on a home-built system as described everywhere.[30] A pulsed Royal-Blue Rebel 447.5 nm LED (Luxeon Star LXML-PR01-0425) was used as the perturbation source, with a pulse width of 4 μs, a repetition frequency of 2 Hz, and a 20 ns rising edge, driven by a homebuilt LED driver circuit and waveform generator (Agilent 33210A). The resulting voltage transient was measured by a Textronix TDS 2024B oscilloscope. A white LED (Bridgelux BXRA-56C9000-J) driven by a TTI Instruments (CPX400SA) power supply was used to illuminate the device, while the device was held at open circuit through a buffer with a 500 GΩ effective input impedance. Samples were mounted in a home-built vacuum chamber and tested under active vacuum (typically between 5 and 15 mTorr). For CE measurements a home-built circuit was used to allow the device to be switched from open-circuit (white light on) to short-circuit (light off). The circuit employs a switch that remains open while the white light is on and then closes when the light turns off, and the device's extracted current is shunted through a 511 Ω resistor. The corresponding voltage decay transient is again measured by the oscilloscope. After data collection, the voltage transient is converted to a current transient using Ohm's Law and used to determine a current volume. Charge carrier density (n) is calculated by integrating the area underneath the transient and dividing by the charge of an electron.

Open circuit photovoltage rise/decay measurements. The TPV/CE setup detailed above, was modified to measure the rise and decay of device photovoltage. The white light was pulsed with a 5 mHz repetition rate while the devices were held at open circuit through a buffer with a 500 GΩ effective input impedance. The photovoltage was measured at the rising edge and falling edge of the white light pulse to obtain the rise and decay transients, respectively.

Notes and References

See Appendix 2 for Additional figures: Device hysteresis with four different perovskite devices in Figure S1. External quantum efficiency spectra for four different perovskite devices in Figure S2. Cyclic voltammetry scans for Zr-TiO_2 and TiO_2 films in Figure S3. Scanning Kelvin probe microscopy images showing topography and surface potential of a Zr-TiO_2 and TiO_2 films in Figure S3. X-ray photoemission spectroscopy (XPS) spectra for Zr-TiO_2 and TiO_2 films in Figure S4. Open circuit voltage transients for four different perovskite devices under three different illumination intensities in Figure S6.

References:

(1) Gao, P.; Gratzel, M.; Nazeeruddin, M. Organohalide lead perovskites for photovoltaic applications. *Energy & Environmental Science* **2014**, *7*, 2448-2463.

(2) Lee, M.; Teuscher, J.; Miyasaka, T.; Murakami, T.; Snaith, H. Efficient Hybrid Solar Cells Based on Meso-Superstructured Organometal Halide Perovskites. *Science* **2012**, *338*, 643-647.
(3) Kojima, A.; Teshima, K.; Shirai, Y.; Miyasaka, T. Organometal Halide Perovskites as Visible-Light Sensitizers for Photovoltaic Cells. *Journal of the American Chemical Society* **2009**, *131*, 6050-6151.
(4) Zhou, H.; Chen, Q.; Li, G.; Luo, S.; Song, T.; Duan, H.; Hong, Z.; You, J.; Liu, Y.; Yang, Y. Interface engineering of highly efficient perovskite solar cells. *Science* **2014**, *345*, 542-546.
(5) Liu, D.; Kelly, T. Perovskite solar cells with a planar heterojunction structure prepared using room-temperature solution processing techniques. *Nature Photonics* **2014**, *8*, 133-138.
(6) Jeon, N.; Noh, J.; Kim, Y.; Yang, W.; Ryu, S.; Il Seol, S. Solvent engineering for high-performance inorganic-organic hybrid perovskite solar cells. *Nature Materials* **2014**, *13*, 897-903.
(7) You, J.; Hong, Z.; Yang, Y.; Chen, Q.; Cai, M.; Song, T.; Chen, C.; Lu, S.; Liu, Y.; Zhou, H. Low-Temperature Solution-Processed Perovskite Solar Cells with High Efficiency and Flexibility. *Acs Nano* **2014**, *8*, 1674-1680.
(8) Hanusch, F.; Wiesenmayer, E.; Mankel, E.; Binek, A.; Angloher, P.; Fraunhofer, C.; Giesbrecht, N.; Feckl, J.; Jaegermann, W.; Johrendt, D.; Bein, T.; Docampo, P. Efficient Planar Heterojunction Perovskite Solar Cells Based on Formamidinium Lead Bromide. *Journal of Physical Chemistry Letters* **2014**, *5*, 2791-2795.
(9) Hao, F.; Stoumpos, C.; Cao, D.; Chang, R.; Kanatzidis, M. Lead-free solid-state organic-inorganic halide perovskite solar cells. *Nature Photonics* **2014**, *8*, 489-494.
(10) Qin, P.; Domanski, A.; Chandiran, A.; Berger, R.; Butt, H.; Dar, M.; Moehl, T.; Tetreault, N.; Gao, P.; Ahmad, S.; Nazeeruddin, M.; Gratzel, M. Yttrium-substituted nanocrystalline TiO_2 photoanodes for perovskite based heterojunction solar cells. *Nanoscale* **2014**, *6*, 1508-1514.
(11) Stranks, S.; Eperon, G.; Grancini, G.; Menelaou, C.; Alcocer, M.; Leijtens, T.; Herz, L.; Petrozza, A.; Snaith, H. Electron-Hole Diffusion Lengths Exceeding 1 Micrometer in an Organometal Trihalide Perovskite Absorber. *Science* **2013**, *342*, 341-344.
(12) Xing, G.; Mathews, N.; Sun, S.; Lim, S.; Lam, Y.; Gratzel, M.; Mhaisalkar, S.; Sum, T. Long-Range Balanced Electron- and Hole-Transport Lengths in Organic-Inorganic CH3NH3PbI3. *Science* **2013**, *342*, 344-347.
(13) Wehrenfennig, C.; Eperon, G.; Johnston, M.; Snaith, H. and Herz, L. High Charge Carrier Mobilities and Lifetimes in Organolead Trihalide Perovskites. *Adv. Mater.* **2014**, *26*, 1584–1589.
(14) Juarez-Perez, E.; Sanchez, R.; Badia, L.; Garcia-Belmonte, G.; Kang, Y.; Mora-Sero, I.; Bisquert, J. Photoinduced Giant Dielectric Constant in Lead Halide Perovskite Solar Cells. *Journal of Physical Chemistry Letters* **2014**, *5*, 2390-2394.

(15) Snaith, H.; Abate, A.; Ball, J.; Eperon, G.; Leijtens, T.; Noel, N.; Stranks, S.; Wang, J.; Wojciechowski, K.; Zhang, W. Anomalous Hysteresis in Perovskite Solar Cells. *Journal of Physical Chemistry Letters* **2014**, *5*, 1511-1515.
(16) Kim, H.; Park, N. Parameters Affecting I-V Hysteresis of CH3NH3PbI3 Perovskite Solar Cells: Effects of Perovskite Crystal Size and Mesoporous TiO2 Layer. *Journal of Physical Chemistry Letters* **2014**, *5*, 2927-2934.
(17) Unger E.;, Hoke E.; Bailie C.; Nguyen W.; Bowring A.; Heumuller T.; Christoforod M.; and McGehee M. Hysteresis and transient behavior in current–voltage measurements of hybrid-perovskite absorber solar cells. *Energy Environ. Sci*., **2014** *7*, 3690-3698. .
(18) Baumann, A.; Tvingstedt, K.; Heiber, M.; Vath, S.; Momblona, C.; Bolink, H.; Dyakonov, V. Persistent photovoltage in methylammonium lead iodide perovskite solar cells. *Apl Materials* **2014**, *2*, 081501.
(19) Schulz, P.; Edri, E.; Kirmayer, S.; Hodes, G.; Cahen, D.; Kahn, A. Interface energetics in organo-metal halide perovskite-based photovoltaic cells. *Energy & Environmental Science* **2014**, *7*, 1377-1381.
(20) Thavasi, V.; Renugopalakrishnan, V.; Jose, R.; Ramakrishna, S. Controlled electron injection and transport at materials interfaces in dye sensitized solar cells. *Materials Science & Engineering R-Reports* **2009**, *63*, 81-99.
(21) Wojciechowski K.; Stranks S.; Abate A.; Sadoughi G.; Sadhanala A.; Kopidakis N.; Rumbles G.; Li C.; Friend R.; Jen A.; and Snaith H. Heterojunction Modification for Highly Efficient Organic-Inorganic Perovskite Solar Cells. ACS Nano, Just Accepted.
(22) Ehrler, B.; Musselman, K.; Bohm, M.; Morgenstern, F.; Vaynzof, Y.; Walker, B.; MacManus-Driscoll, J.; Greenham, N. Preventing Interfacial Recombination in Colloidal Quantum Dot Solar Cells by Doping the Metal Oxide. *Acs Nano* **2013**, *7*, 4210-4220.
(23) Pathak, S.; Abate, A.; Ruckdeschel, P.; Roose, B.; Godel, K.; Vaynzof, Y.; Santhala, A.; Watanabe, S.; Hollman, D.; Noel, N.; Sepe, A.; Wiesner, U.; Friend, R.; Snaith, H.; Steiner, U. Performance and Stability Enhancement of Dye-Sensitized and Perovskite Solar Cells by Al Doping of TiO2. *Advanced Functional Materials* **2014**, *24*, 6046-6055.
(24) Kitiyanan, A.; Yoshikawa, S. The use of ZrO_2 mixed TiO_2 nanostructures as efficient dye-sensitized solar cells' electrodes. *Materials Letters* **2005**, *59*, 4038-4040.
(25) Liu, H.; Tang, J.; Kramer, I.; Debnath, R.; Koleilat, G.; Wang, X.; Fisher, A.; Li, R.; Brzozowski, L.; Levina, L.; Sargent, E. Electron Acceptor Materials Engineering in Colloidal Quantum Dot Solar Cells. *Advanced Materials* **2011**, *23*, 3832-3837.
(26) Tang, J.; Kemp, K.; Hoogland, S.; Jeong, K.; Liu, H.; Levina, L.; Furukawa, M.; Wang, X.; Debnath, R.; Cha, D.; Chou, K.; Fischer, A.; Amassian, A.; Asbury, J.; Sargent, E.

Colloidal-quantum-dot photovoltaics using atomic-ligand passivation. *Nature Materials* **2011**, *10*, 765-771.
(27) *Noel N.; Abate A.; Stranks S.; Parrott E.; Burlakov V.; Goriely A.; and Snaith H. Enhanced Photoluminescence and Solar Cell Performance via Lewis Base Passivation of Organic–Inorganic Lead Halide Perovskites ACS Nano, **2014**, 8, 9815–9821*.
(28) Abate, A.; Saliba, M.; Hollman, D.; Stranks, S.; Wojciechowski, K.; Avolio, R.; Grancini, G.; Petrozza, A.; Snaith, H. Supramolecular Halogen Bond Passivation of Organic-Inorganic Halide Perovskite Solar Cells. *Nano Letters* **2014**, *14*, 3247-3254.
(29) Credgington, D.; Durrant, J. Insights from Transient Optoelectronic Analyses on the Open-Circuit Voltage of Organic Solar Cells. *Journal of Physical Chemistry Letters* **2012**, *3*, 1465-1478.
(30) Knesting, K.; Ju, H.; Schlenker, C.; Giordano, A.; Garcia, A.; Smith, O.; Olson, D.; Marder, S.; Ginger, D. ITO Interface Modifiers Can Improve V-OC in Polymer Solar Cells and Suppress Surface Recombination. *Journal of Physical Chemistry Letters* **2013**, *4*, 4038-4044.
(31) Bergmann, V.; Weber, S.; Ramos, F.; Nazeeruddin, M.; Gratzel, M.; Li, D.; Domanski, A.; Lieberwirth, I.; Ahmad, S.; Berger, R. Real-space observation of unbalanced charge distribution inside a perovskite-sensitized solar cell. *Nature Communications* **2014**, *5*.

Chapter6: Conclusions

This thesis has investigated long-lived charge carrier dynamics in polymer/quantum dot blends and organometal halide perovskites. Chapter three demonstrated that the PSOTT/PbS quantum dot blend undergoes significant energy-transfer from polymer to the PbS quantum dots without charge transfer, in contrast with the photoinduced charge transfer processes observed in the other blends (PDTPQx-HD/PbS quantum dot blend and PPEHTT/PbS quantum dot blend), resulting in working solar cells.

Chapter four demonstrated that both the PIA signal associated with charge formation on the polymer, as well as the external quantum efficiency of the hybrid photovoltaic devices decreased in magnitude with increasing quantum dot size, despite the broader absorption spectrum of the larger dots. We interpret these results as evidence that PTB1/PbS blends behave at least partially as bulk heterojunction (BHJ) solar cells, and conclude that the long-lived charge transfer yield is diminished at larger dot sizes as the energy level offset at the polymer/quantum dot interface is changed through decreasing quantum confinement. As discussed in chapter four, we speculate that these blends may be operating partially as QD Schottky diode cells, in parallel with a polymer/QD bulk heterojunction. The observed size-independent PL quenching (Figure S4 in Appendix1) could indicate that both charge and energy transfer are fast enough to compete with radiative decay, or that energy transfer and fast, energy-dependent, back hole transfer may be occurring in these blends. Such questions will be interesting topics for future investigations, and might be addressed with transient absorption spectroscopy. The fact that both the device performance and PIA measurements are consistent with decreased charge generation for smaller QD band gaps is notable. If we assume that the limiting factor for forming a type II heterojunction in this system is the energy offset between the valence band of the QD and the HOMO of the polymer, then our data indicate that the population of long-lived polarons residing on the polymer is reduced by the driving force for charge separation, although there is some uncertainty associated with extrapolating energy level offsets measured via cyclic voltammetry or photoemission to a solid-state device geometry.[1, 2] Our results point to a very strong dependence of long-lived polaron populations on the relative energy level alignment at the PbS/PTB1 interface, something that has not been reported previously in numerous studies.[3, 4] On the other hand, our data could also be consistent with the long-lived carrier population in these blends being limited by the recombination of the polymer hole polaron population with electrons on the QDs, as the barrier for this recombination event would be the driving force for the opposite hole transfer process. Future studies utilizing fast (e.g. picosecond) transient absorption spectroscopy, or temperature dependent PIA experiments could help differentiate between these processes.

Chapter five demonstrated that hybrid organometal halide perovskite solar cells employing Zr-TiO_2 electrodes and pyridine treatment give rise to an increase in overall power conversion efficiency and a decrease in hysteresis. We observed longer carrier lifetimes and higher charge carrier densities in devices on Zr-TiO_2 electrodes at microsecond times in transient photovoltage experiments, as well as at longer persistent photovoltages extending from ~millisecond to tens of sec. Furthermore, devices with Zr-TiO_2 electrodes and pyridine treatment show stabilized device performance as well as faster photovoltage rises. We interpret these results as indicating that the long time voltage decays are likely not a simple recombination process but are related to trap filling and emptying. We thus propose that the devices with Zr-TiO_2 somehow fills the trap distribution more quickly, but empties the filled charges more slowly. We attribute the faster photovoltage rise and faster photovoltage decay for the devices with pyridine treatment to lower trap density due to passivation of defect sites.[5] Future studies utilizing microscopic techniques (e.g. Kelvin probe force microscopy) to observe charge distribution could help the understanding of complicated competing effects on the carrier lifetimes.[6] Furthermore, interface modification of electron transporting layer employing fullerene derivatives would lead to further improvement and the understanding of device studies.[7] Finally, with the growing interest in hybrid polymer/PbS quantum dot solar cells and perovskite solar cells, they could lead to next-generation solar cells that are better than silicon in terms of both of performance and cost.

References

(1) MacLeod, B.; Horwitz, N.; Ratcliff, E.; Jenkins, J.; Armstrong, N.; Giordano, A.; Hotchkiss, P.; Marder, S.; Campbell, C.; Ginger, D. Built-In Potential in Conjugated Polymer Diodes with Changing Anode Work Function: Interfacial States and Deviation from the Schottky-Mott Limit. *Journal of Physical Chemistry Letters* **2012**, *3*, 1202-1207.

(2) Munro, A.; Zacher, B.; Graham, A.; Armstrong, N. Photoemission Spectroscopy of Tethered CdSe Nanocrystals: Shifts in Ionization Potential and Local Vacuum Level As a Function of Nanocrystal Capping Ligand. *ACS Applied Materials & Interfaces* **2010**, *2*, 863-869.

(3) Kamat, P. Quantum Dot Solar Cells. Semiconductor Nanocrystals as Light Harvesters. *Journal of Physical Chemistry C* **2008**, *112*, 18737-18753.

(4) Coffey, D.; Larson, B.; Hains, A.; Whitaker, J.; Kopidakis, N.; Boltalina, O.; Strauss, S.; Rumbles, G. An Optimal Driving Force for Converting Excitons into Free Carriers in Excitonic Solar Cells. *Journal of Physical Chemistry C* **2012**, *116*, 8916-8923.

(5) *Noel N.; Abate A.; Stranks S.; Parrott E.; Burlakov V.; Goriely A.; and Snaith H. Enhanced Photoluminescence and Solar Cell Performance via Lewis Base Passivation of Organic–Inorganic Lead Halide Perovskites ACS Nano,* ***2014****, 8, 9815–9821*.

(6) Bergmann, V.; Weber, S.; Ramos, F.; Nazeeruddin, M.; Gratzel, M.; Li, D.; Domanski, A.; Lieberwirth, I.; Ahmad, S.; Berger, R. Real-space observation of unbalanced charge distribution inside a perovskite-sensitized solar cell. *Nature Communications* **2014**, *5*.
(7) Wojciechowski K.; Stranks S.; Abate A.; Sadoughi G.; Sadhanala A.; Kopidakis N.; Rumbles G.; Li C.; Friend R.; Jen A.; and Snaith H. Heterojunction Modification for Highly Efficient Organic-Inorganic Perovskite Solar Cells. ACS Nano, Just Accepted.

Appendix 1 for Chapter 3: Size-Dependent Charge Transfer Yields in Conjugated Polymer/Quantum Dot Blends

The original article can be found at http://pubs.acs.org/doi/abs/10.1021/jp412545q

External quantum efficiency of PTB1/PbS devices with different ligand exchange

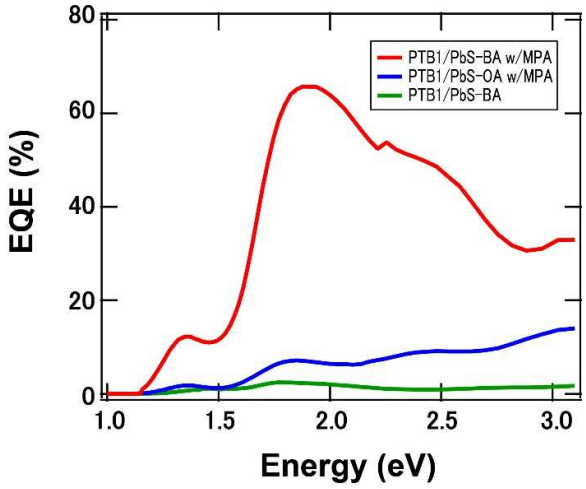

Figure S1 Figure S1. Effect of different ligand treatment of QD for PTB1/PbS QD photovoltaic devices. EQE spectra shows devices for PbS-butylamine (BA) with post-deposition MPA treatment (PbSBA w/MPA, red line), for PbS-oleate (OA) with post-deposition MPA treatment (PbS-OA w/MPA, blue line) as well as for PbS-butylamine (PbS-BA, green line).

Figure S1 shows the external quantum efficiency (EQE) spectra of PTB1/PbS QD devices using PbS-butylamine (BA) with post-deposition MPA treatment (PbS-BA w/MPA, red line), PbS-oleate (OA) with post-deposition MPA treatment (PbS-OA w/MPA, blue line) and PbS-BA (PbS-BA, green line). The significant increase in short-circuit current of the device for PbS-BA with post-deposition MPA ligand treatment are correlated with enhancing carrier mobility, decreasing a trapping site in QDs and improving device morphology relative to the device for PbSOA with post-deposition MPA treatment and PbS-BA.

Photo-induced Absorption

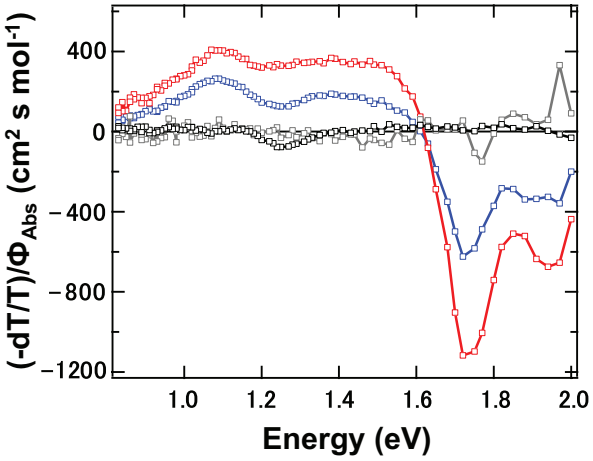

Figure S2 PIA spectra of films of neat PTB1 (gray), neat PbS quantum dots (black) with a 1.25 eV band gap, PTB1/PbS blend using 1.25 eV band gap QDs (blue) and PTB1/PC71BM (red). PIA spectra were scaled by the absorbed photon flux (ΦAbs) under 2.77 eV excitation.

Figure S2 shows the X Channel PIA spectra of a blend of PTB1 with PbS quantum dots using 1.25 eV band gap QDs (blue), a blend of PTB1 with PC71BM (red), a neat film of PbS quantum dots with a 1.25 eV band gap (black) and a neat film of PTB1 (gray). The neat polymer exhibits none of the features exhibited in the blend.

Experimental Methods. PTB1/PCBM blends were prepared in a similar manner by mixing the PTB1 solution with a 15 mg/mL solution of PC71BM in dichlorobenzene in a 1:1 (w/w) ratio.

Effect of MPA Ligand on Photoluminescence of solid QD films

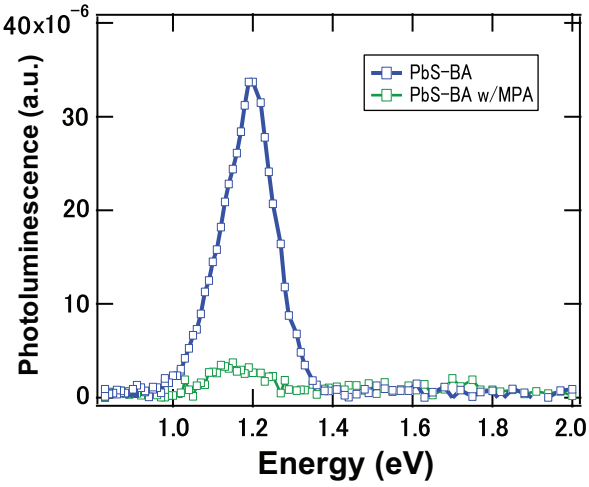

Figure S3 The photoluminescence (PL) spectra of films for PbS-butylamine (PbS-BA, blue

squares) and PbS-butylamine (BA) with post-deposition MPA treatment (PbS-BA w/MPA, green squares). These films were excited at 2.77 eV.

Figure S3 shows the PL spectra of films of PbS-butylamine (PbS-BA, blue squares) and PbSbutylamine (BA) with post-deposition MPA treatment (PbS-BA w/MPA, green squares). Treating PbS QDs with MPA greatly diminishes the PL (at 1.20 eV) from the QD. Films were made by spin coating on glass in the same way as the PIA samples. PL spectra were collected by the PIA set-up.

Photoluminescence Quenching in Polymer/QD blends.

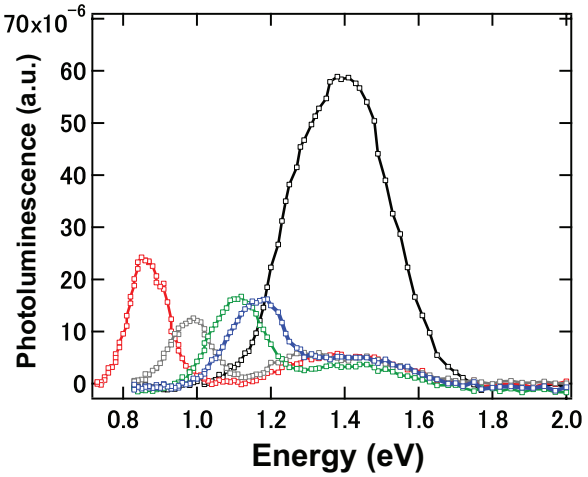

Figure S4 The photoluminescence (PL) spectra of polymer/PbS QDs blends with varying QDs band gap, 1.25 eV (blue), 1.22 eV (green), 1.05 eV (gray), and 0.90 eV (red) (butylamine treated) shown in Figure 3 in the manuscript. The black spectrum shows the PL of the neat PTB1 polymer. The PL spectra were collected in parallel with the PIA data, using an automated shutter to block the probe light.

Films that have not been post-treated with thiols show residual photoluminescence since thiol treatment tends to quench the PL signal of QD (Figure S3).[1] Figure S4 shows the PL spectra of a film of a neat PTB1 film (black curve) and the PTB1/PbS blends with varying QDs band gap, 1.25 eV (blue), 1.22 eV (green), 1.05 eV (gray), and 0.90 eV (red) (butylamine treated). In all cases, the polymer PL signal peaking at ~1.4 eV is largely quenched in the presence of PbS QDs, indicating that blending the polymer with QDs introduces competitive relaxation pathways to excitons on the polymer. The PIA data suggest that charge transfer is occurring in all blends – but with a size-dependent yield of long-lived carriers. On the other

hand, Figure S4 indicates roughly equal amounts of PL quenching in all blends. Notably, the polymer PL is largely quenched even in blends with low band gap QDs, even though little polymer polaron signal is observed in the PIA spectra for these blends. This result could indicate the existence of an energy transfer pathway from the excited polymer to PbS QDs as observed in our previous work.[2]

Photoluminescence excitation (PLE)

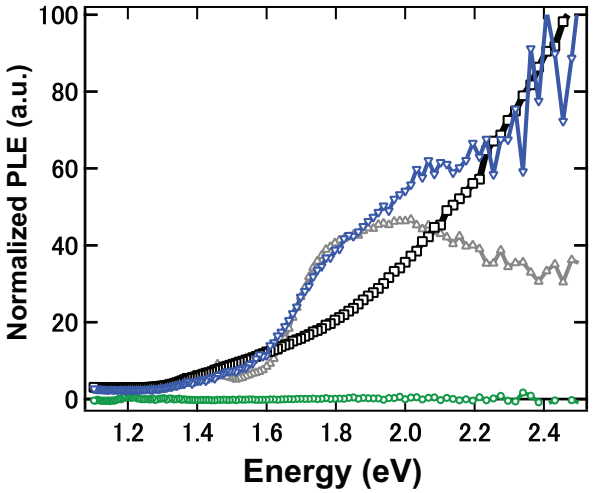

Figure S5 Photoluminescence excitation data using QDs with a 1.05 eV band gap. The blue (solid) line is signal from light detected at wavelengths greater than 1200 nm (1.03 eV) for a PTB1/PbS blend. The grey line is signal from light detected at wavelengths greater than 900 nm (1.38 eV) for a pristine PTB1. The black line is signal from light from a neat PbS detected at wavelengths greater than 1200 nm. The green line shows that no signal is detected from pristine PTB1 at wavelengths greater than 1200 nm.

We employed photoluminescence excitation (PLE) spectroscopy to investigate the possibility of energy transfer from the polymer to the QDs. Spectra were acquired by monitoring the quantum dot photoluminescence signal while sweeping the excitation light on the following three different films: a pristine PTB1, a neat PbS and a PTB1/PbS blend. Figure S5 shows the resulting PLE data. As expected, the PLE trace for the pristine quantum dot film detected at the quantum dot emission peak (black line) tracks the quantum dot absorption spectrum. Likewise the neat PTB1 polymer film shows no detectable emission at the quantum dot emission peak (green line). On the other hand, a PLE trace that follows the polymer absorption spectrum can be measured when detected at the polymer emission peak (gray line). Notably, the PLE trace for the PTB1/PbS quantum dot blend (collected at the quantum dot

emission) shows a strong feature that exactly matches the polymer absorption peak, providing strong evidence that energy transfer can indeed occur from PTB1 to PbS quantum dots in this size range.

Experimental Methods: PLE samples were made by spin coating the films on glass in the same way as the PIA samples. Since MPA treatment tends to quench the PL signal (mainly the quantum dot photoluminescence) the presented samples were left untreated. The same monochromated tungsten halogen lamp was used as the excitation source and sample photoluminescence intensity was monitored with a Si/InGaAs dual-band photodetector (ThorLabs,DSD2). A 900 nm long pass filter was used to filter excitation light in the pristine PTB1 spectrum, and a 1200 nm long pass filter was used to filter both scattered excitation light and polymer PL in the pristine PbS, PTB1/PbS, and pristine PTB1 control samples. Samples were held under dynamic vacuum with the film facing the excitation light. Emitted light was waveguided from the side of the glass substrate and focused using two aspheric lenses mounted in front of the photodetector. A fraction of the excitation light was split with a glass microscope slide to monitor the excitation intensity with an amplified silicon ($l \leqq 1000$ nm) or an amplified InGaAs ($l > 1000$ nm) photodetector. All spectra were normalized to the excitation intensity. Spectra for pristine PbS and PTB1/PbS were normalized to the nanocrystal exciton peak at ~1.05 eV. The pristine PTB1 spectra were scaled to match the blend intensity at 1.8 eV.

References

(1) Nelson, G.; Zhu, X. Reversible Surface Electronic Traps in PbS Quantum Dot Solids Induced by an Order-Disorder Phase Transition in Capping Molecules. *J. Am. Chem. Soc.* **2012**, *134*, 7592-7595.

(2) Strein, E.; Colbert, A.; Subramaniyan, S.; Nagaoka, H.; Schlenker, C. W.; Janke, E.; Jenekhe, S. A.; Ginger, D. S. Charge generation and energy transfer in hybrid polymer/infrared quantum dot solar cells. *Energy Environ. Sci.* **2013**, *6*, 769-775.

Appendix 2 for Chapter 5:

Zr-doped TiO_2 Electrodes Reduce Hysteresis and Improve Performance in Hybrid Perovskite Solar Cells while Increasing Carrier Lifetimes

Experimental methods:

J-V characteristics and time-dependent photocurrent measurements. Current density-voltage (J-V) curves were measured using a source meter (Keithley, 2400 Series) under AM 1.5 G light illumination from a solar simulator (Solar Light Co. model 16S-300) with intensity calibrated to 100 mW/cm^2 using a Si reference cell. The solar cells were masked with a metal aperture to define the active area, typically 0.013 cm^{-2}, and measured in a light-tight sample holder to minimize edge effects. Scanning rates of 0.15V/s or 0.025V/s were used to assess the hysteretic behavior of devices.

External quantum efficiency. Solar cells were illuminated with a monochromated (Acton 2150) 100 W tungsten-halogen light source (Oriel). Photocurrent spectra were measured using a Keithley 2400 source meter. A calibrated silicon photodiode (OSI optoelectronics) was used to calculate external quantum efficiencies. All photovoltaic measurements were collected with devices under dynamic vacuum (~20 mTorr).

Cyclic voltammetry. Cyclic voltammograms (CV) were acquired using a potentiostat (Autolab). Zr-doped TiO_2 and undoped TiO_2 films cast on FTO served as the working electrodes. The counter electrode and reference electrode were a platinum wire and Ag/AgCl in saturated 3M KCl solution, respectively. Tetrabutylammonium hexaflurophosphate (0.1 M) in anhydrous acetonitrile was used as the supporting electrolyte. Voltammograms were obtained using a scan rate of 0.25 V/s and by sweeping the voltage from 0 V → −1.5 V → 0 V. A ferrocene/ferricinum redox was used as the standard reference (−4.80 V relative to vacuum).[1]

X-ray photoemission spectroscopy (XPS). Zr-TiO_2 and TiO_2 films on FTO were measured in a Kratos Axis Ultra DLD under ultrahigh vacuum. A monochromated Al K-alpha x-ray anode ($h\nu$ = 1486.6 eV) was used to irradiate all samples. Data was collected and analyzed from a 300 x 700 μm spot size.

Scanning Kelvin probe microscopy (SKPM). The surface potential of Zr-TiO_2 and TiO_2 films on FTO were measured using Scanning Kelvin Probe Microscopy (Cypher/AFM, Asylum Research). A Cr/Pt coated tip (300kHz, spring constant 40 N/m) was used for all measurements.

Relative work functions were acquired by comparing the average surface potential of Zr-TiO_2 to TiO_2.

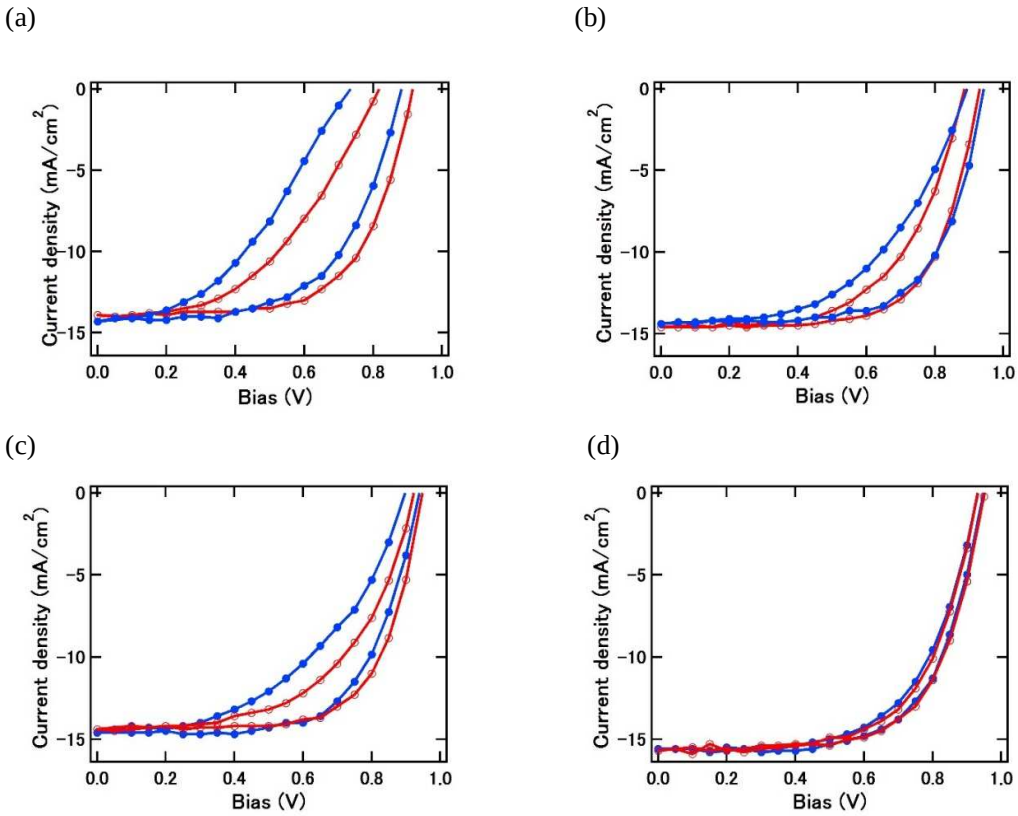

Figure S1 J-V curves of devices with (a) TiO_2 electrodes, (b) Zr-TiO_2 electrodes, (c) TiO_2/pyridine treatment, and (d) Zr-TiO_2/pyridine treatment acquired at the scanning rate of 0.15 V/s (blue filled circle) and 0.025 V/s (red empty circle).

Figure S1 shows the J-V characteristics measured when scanning from open circuit (V_{OC}) to short circuit (SC) and SC to Voc for TiO_2, Zr-TiO_2, TiO_2/pyridine treated, and Zr-TiO_2/pyridine treated devices. We report a significant reduction in the measured hysteresis in pyridine treated devices with Zr-TiO_2 electrodes. This observation is consistent even when measuring the solar cell with a different scan rate. Devices with TiO_2 electrodes, Zr-TiO_2 electrodes and TiO_2/pyridine treatment show large hysteretic behavior at both scanning rates.

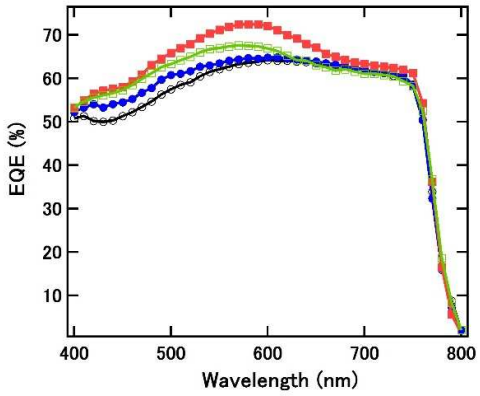

Figure S2 (a) External quantum efficiency spectra of complete devices using Zr-TiO_2 (blue filled circle), TiO_2 (black empty circle), Zr-TiO_2/pyridine treatment (red filled square) and TiO_2/pyridine treatment (green empty square)

Figure S2 shows the external quantum efficiency (EQE) spectra for Zr-TiO_2, TiO_2, Zr-TiO_2/pyridine treated and TiO_2/pyridine treated devices. We find charges are more efficiently extracted in Zr doped devices at shorter wavelengths (400 nm to 600 nm) and pyridine treatments improve charge collection efficiency across nearly the entire absorbing spectrum in both Zr-TiO_2 and TiO_2 devices.

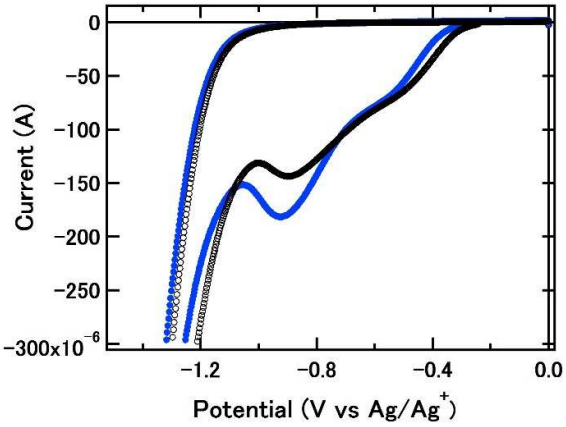

Figure S3 Cyclic voltammetry scans of Zr-TiO_2 (blue filled circle) and TiO_2 (black empty circle) films.

Figure S3 shows the current vs. voltage traces of Zr-TiO_2 (blue) and TiO_2 (black) films on FTO using cyclic voltammetry (CV). We report a slightly higher reduction potential (-0.92 V) for Zr-TiO_2 electrodes, compared to the measured reduction potential for TiO_2 electrodes (-0.87 V). Furthermore, we find an increase in the current amplitude for Zr-TiO_2, suggesting faster

reduction kinetics near the CB edge.

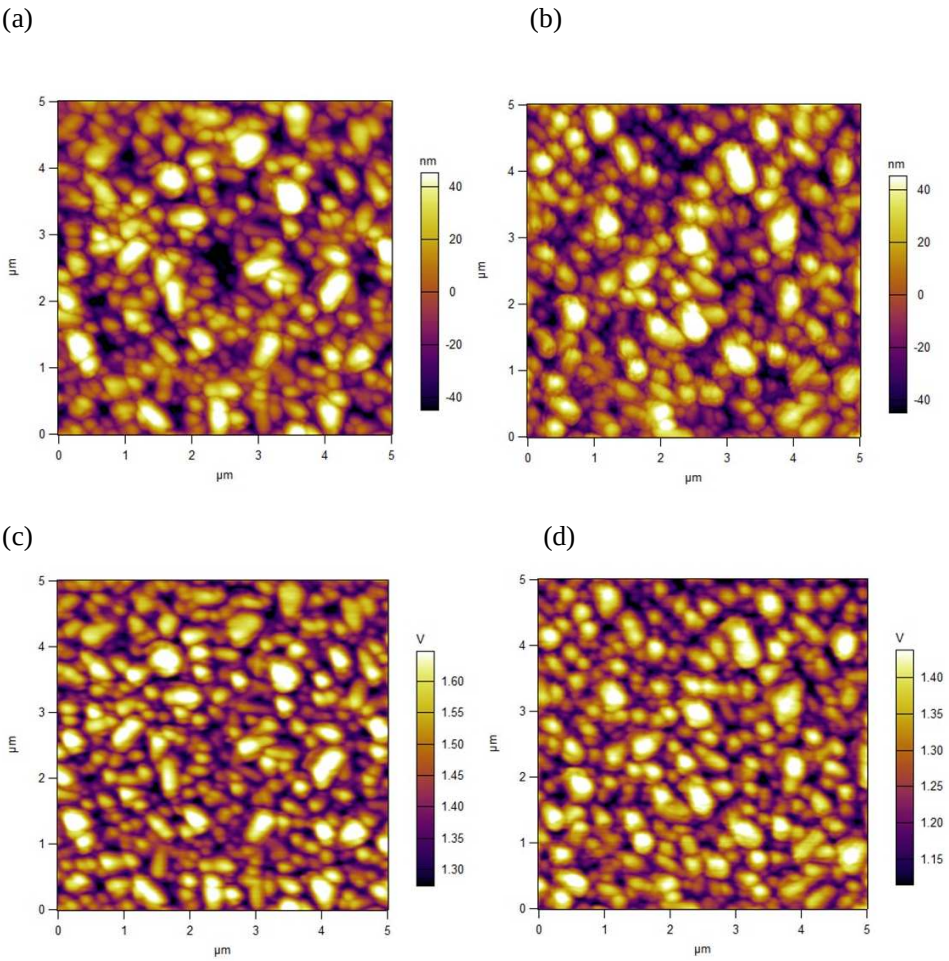

Figure S4 Scanning Kelvin probe microscopy (SKPM) images showing (a, c) topography and surface potential of a Zr-TiO_2 film and (b, d) topography and surface potential of a TiO_2 film.

Figure S4 shows topography and surface potential images obtained using scanning Kelvin probe microscopy (SKPM). The average work function difference between Zr-TiO_2 electrodes and TiO_2 electrodes is 0.18 V±0.04V, indicating a shallower work function for Zr-TiO_2 electrodes.

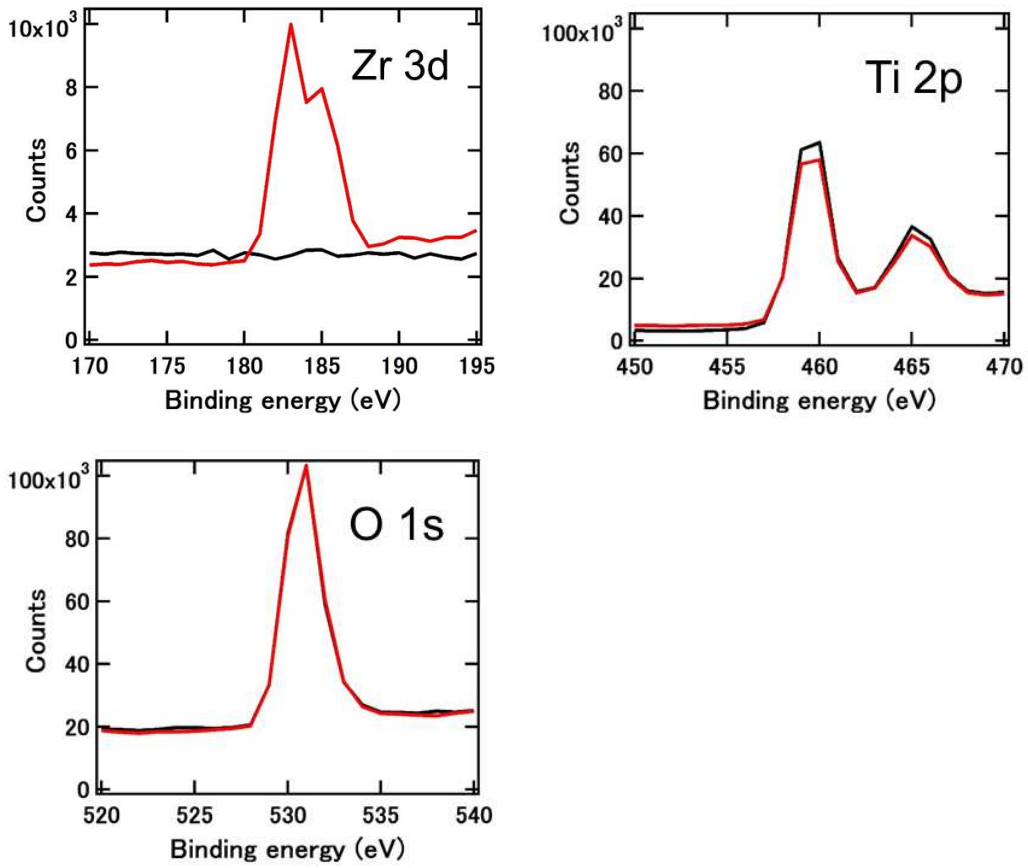

Figure S5 X-ray photoemission spectroscopy (XPS) spectra for Zr-TiO_2 (red) and TiO_2 (black) films on bare FTO. (a) XPS spectra of Zr 3d (b) XPS spectra of Ti 2p (c) XPS spectra of O 1s.

Figure S5 shows X-ray photoemission spectroscopy (XPS) spectra for Zr-TiO_2 and TiO_2 films on FTO. We confirm the successful doping of zirconium in TiO_2 by identifying the Zr 3d feature at 182.5 eV[2] and the decrease in intensity of the Ti 2p feature. We also report the Ti 2p and O 1s core level binding energies at 458.5 eV and 530.0 eV, respectively.[2] We integrate Zr3d and Ti2p peaks to calculate the Zr to Ti atomic ratio in the Zr-TiO_2 film to be 6% (1 to 15.69).

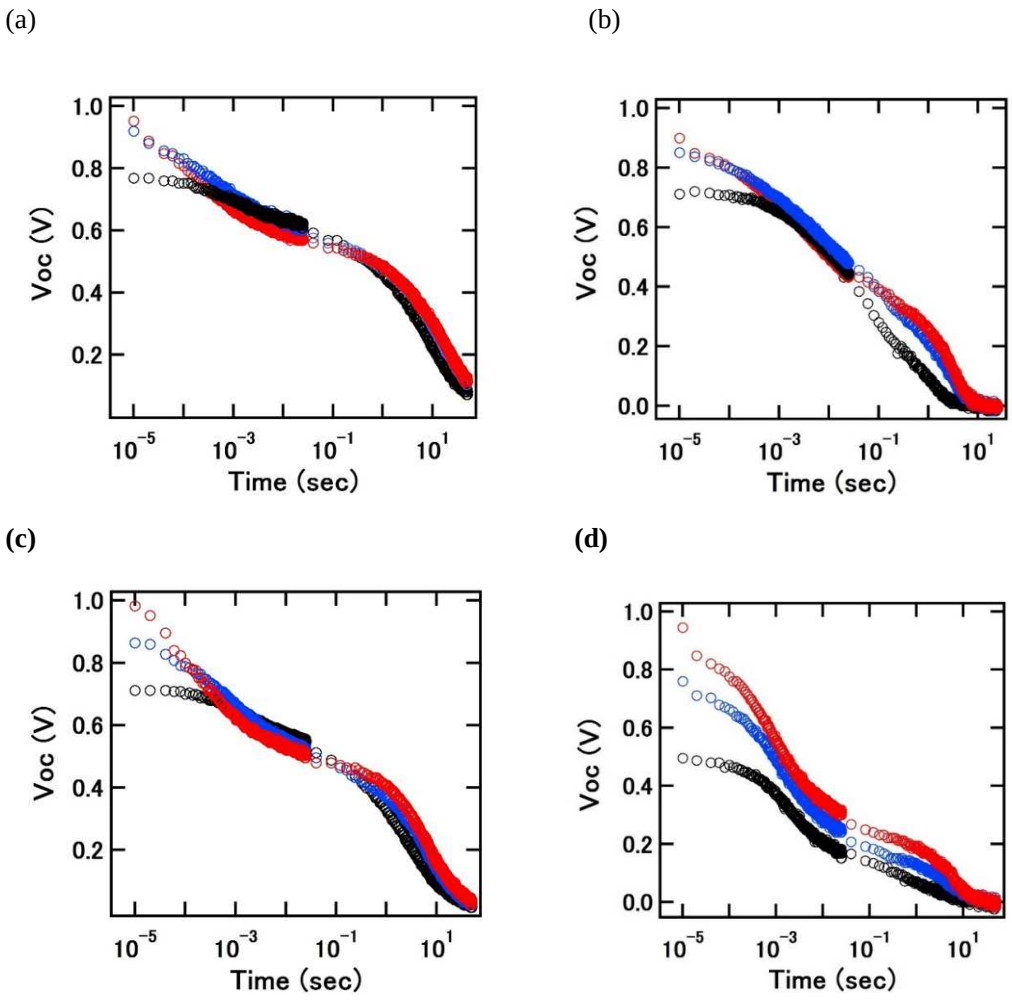

Figure S6 (a) Open circuit voltage transients for the perovskite devices based (a) Zr-TiO_2, (b) TiO_2, (c) Zr-TiO_2/pyridine treatment, (d) TiO_2/pyridine treatment under 118 mW/cm^2 (red circle), 11.1 mW/cm^2 (blue circle) and 2.0 mW/cm^2 (black circle) white LED illumination.

Figure S6 shows open circuit voltage transients for the four different perovskite devices under three different illumination intensities. Under high illumination intensities, all devices exhibit a fast photovoltage decay at short time scales ($<10^{-3}$ s) followed by a slower photovoltage decay at longer times ($>10^{-1}$ s)

References:

(1) Liu, H.; Tang, J.; Kramer, I.; Debnath, R.; Koleilat, G.; Wang, X.; Fisher, A.; Li, R.; Brzozowski, L.; Levina, L.; Sargent, E. Electron Acceptor Materials Engineering in Colloidal Quantum Dot Solar Cells. *Advanced Materials* **2011**, *23*, 3832-3837.

(2) Reddy, B.; Chowdhury, B.; Ganesh, I.; Reddy, E.; Rojas, T.; Fernandez, A. Characterization of V_2O_5/TiO_2-ZrO_2 catalysts by XPS and other techniques. *Journal of Physical Chemistry B* **1998**, *102*, 10176-10182.

Appendix 3 for Chapter 2:

Photoinduced absorption spectroscopy (PIA) manual

Turning on Electronics

- Turn on vacuum pump
  - Pump down until the needle gauge indicates that there's a vacuum

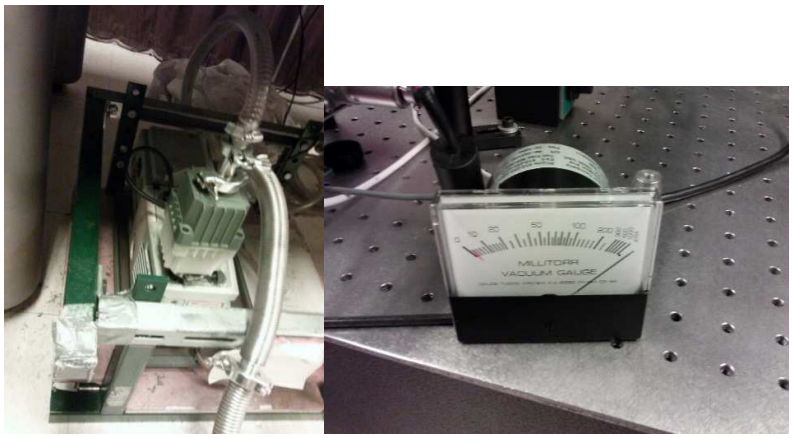

- Gently turn on water at the sink to cool the lamp
- Turn on air near the sink to cool the LED
  - Pull the tube out of the sink to see if water is flowing

- Turn on the DC Power Supply for the lamp
  - **BEFORE turning it on**, make sure voltage is turned all the way down
  - Turn current all the way up
  - Slowly turn up the voltage to ~10.80V

- Watch the current rise as you turn up the voltage. It should be ~8A
- We want current*voltage to be ~80W

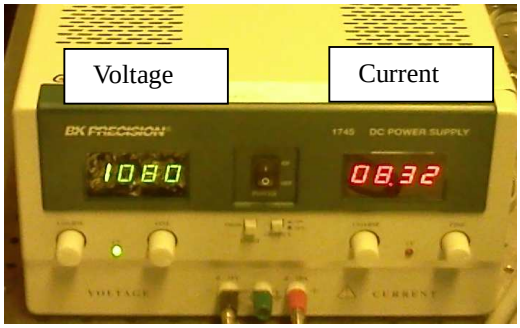

- Turn on the preamplifer (SR570)
  - Bias voltage = off
  - Input offset = off
  - Filter type = none
  - Gain mode = high bandwidth
  - Sensitivity = 200nA/V default
- You may have to adjust sensitivity
- Don't change sensitivity after setting the lockin phase

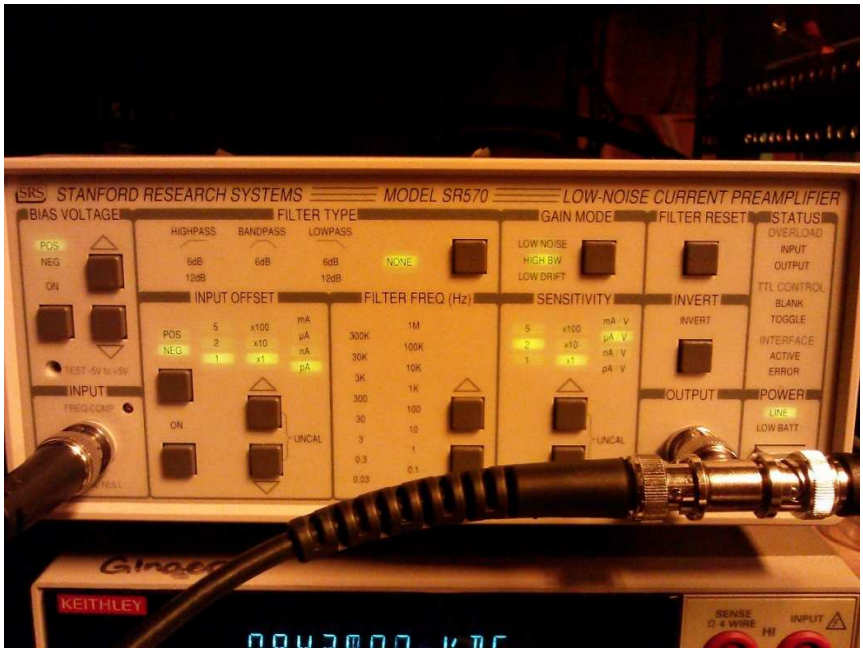

- Turn on the lock-in amplifier (SR830)
  - Time constant = 300mA, 24dB
  - Signal input = A, AC, float
  - Reserve = normal
  - Filters = line, 2x line
    - Turn filters off for frequency modulated measurement (later)
  - Channel 1 = x, Channel 2 = y
  - Sensitivity will change

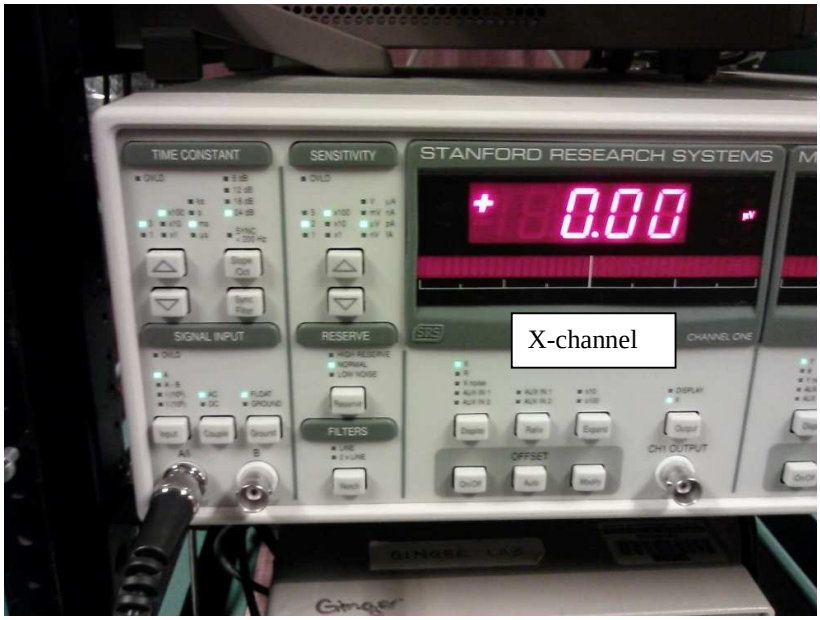

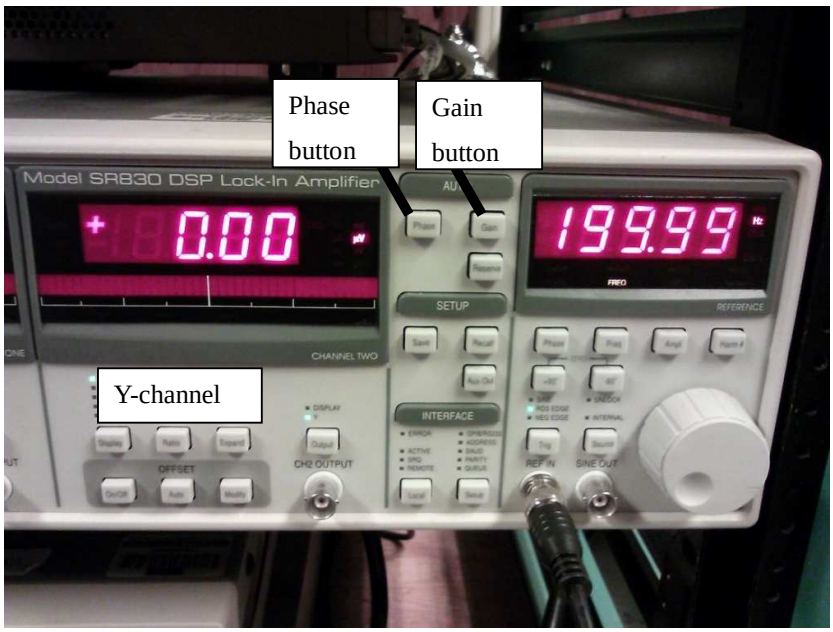

Turn on the function generator (Agilent 33120A arbitrary waveform generator)

- Press the square wave button
- Set to 200Hz

- Turn on the function generator's power supply

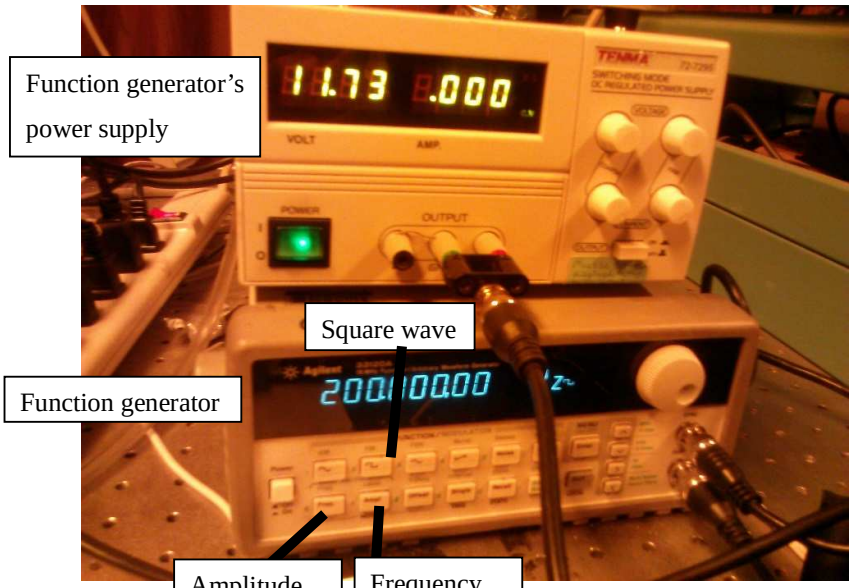

- Turn on the Keithley 2000

Aligning Lamp and Excitation Beam

- Go onto the Computer
  - Open “Acton Set Slits”
  - Open “Acton Grating Change”
  - Open “Acton Set Wavelength”

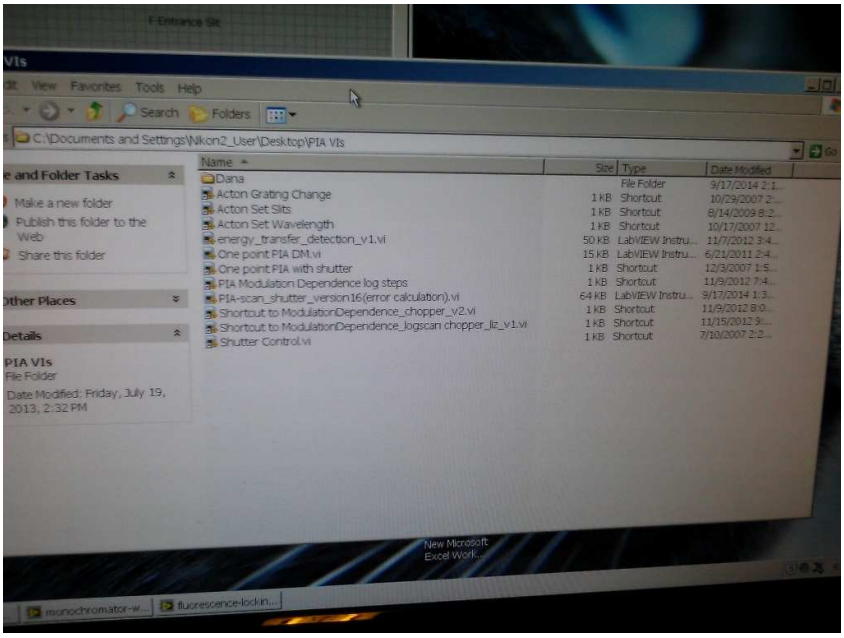

- On the “Set Wavelength” program
  - Select Port 2 and wavelength = 600nm [Press run]

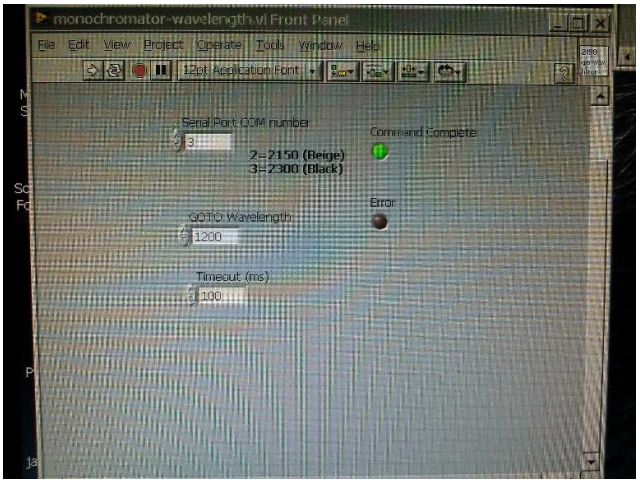

- On the “Grating Change” program
  - Grating 1 is for wavelengths up ~650nm

- Grating 2 is for wavelengths 650nm to Near IR

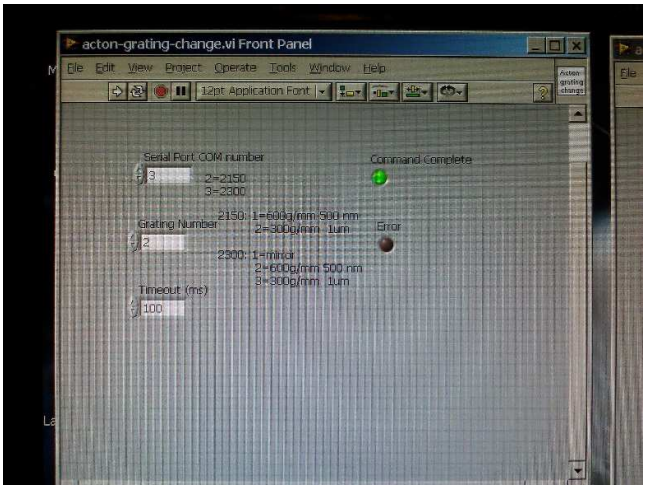

- On the “Set Slits” program
- Select Port 2 and slit width = 500um for T entrance slit [Press run]
- Select slit width = 500um for T exit slit [Press run]
- Select Port 3 and slit width = 500um for T entrance slit [Press run]
- Select slit width = 500um for T exit slit [Press run]

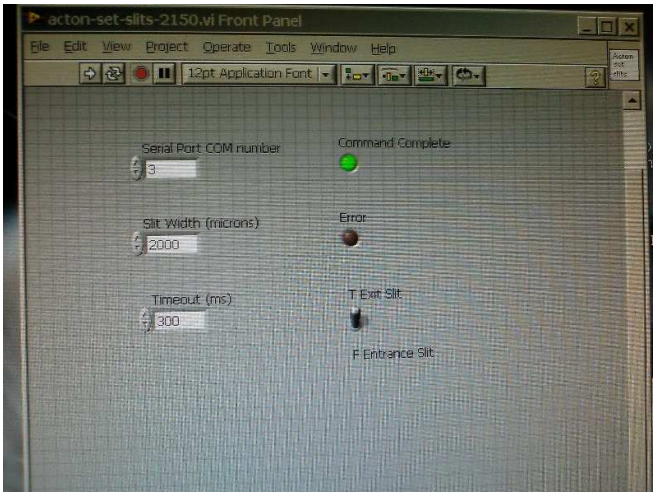

- Put a white block on the sample stage
- Focus the incoming beam (from monochromator) at the center of the stage by turning knobs on the stage

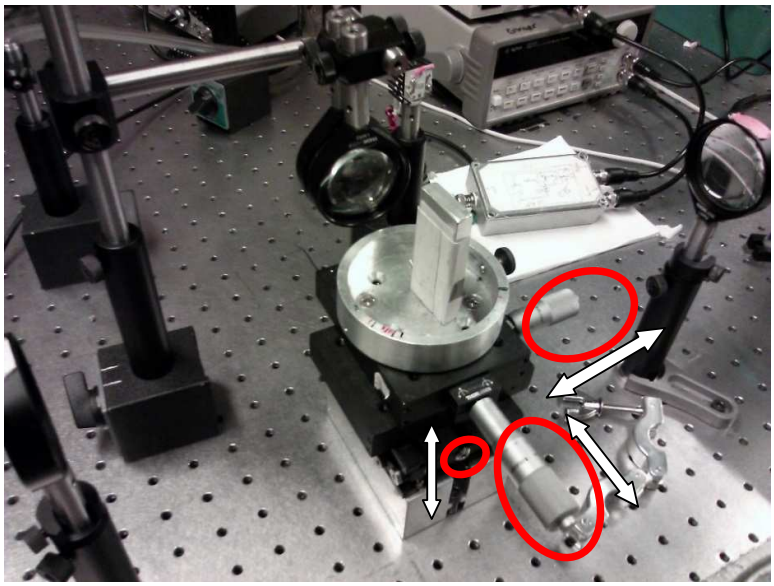

- Connect the LED to the amplifier circuit
- i.e. there is a box with BNC cables connected to the function generator and power source. Take the third BNC cable and connect it to the LED.
- Put the LED nub into the hole on the collimating reflector

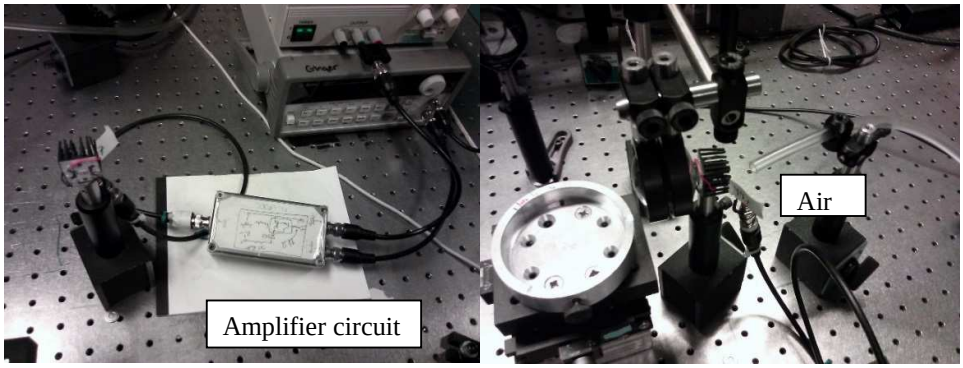

- Change the amplitude on the function generator to 3V (LED will turn on)
  Turn the voltage up to ~12V to get a current of 650 mA
  (but this changes based on LED specs - check the power output of the LED)

- Put the white block back on the sample stage
- Move the LED and reflector so that the lamp beam (red light) and LED beam (blue light) are aligned and focused at the center of the stage.

(You may turn down the LED intensity to see both lights simultaneously)

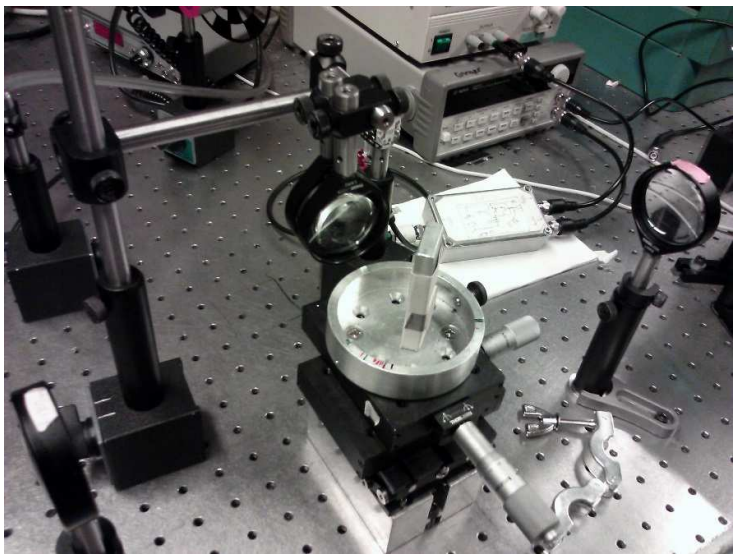

Aligning the Si-InGaAs detector

- On the function generator, turn down the LED amplitude so you can't see it
- Go onto the computer
- On the "Set Wavelength" program
  - Select Port 2 and wavelength = 1000nm [Press run]
  - Select Port 3 and wavelength = 1000nm [Press run]

(1000nm was selected for the detector because that's where the max signal is

- On the "Grating Change" program
  - Select Port 2 and grating = 2 [Press run]
  - Select Port 3 and grating = 2 [Press run]
- Change the long pass (LP) filter to 550 nm

(but this LP filter changes based on LED e.g. Red LED 630nm, LPfilter 650nm)

  - The filter is located in front of the black box of monochromator 3
  - Move the filter aside - bend the top so that it is not over the hole

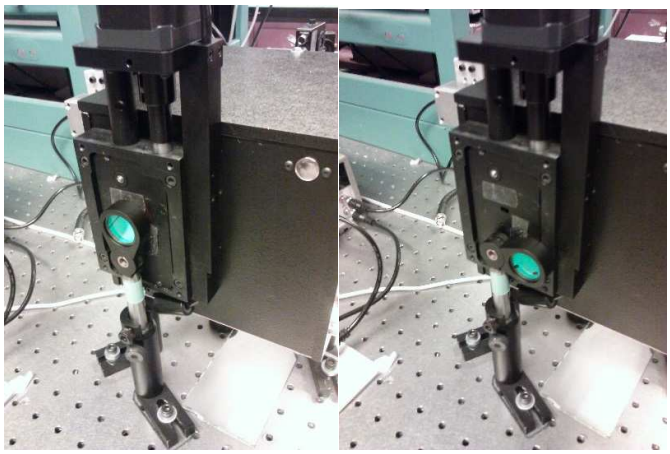

- Turn the knobs on the dual band Si-InGaAs detector (Thorlabs, DSD2) to maximize the signal on the Keithley
  - If the Keithley is not responding, press the “local” button

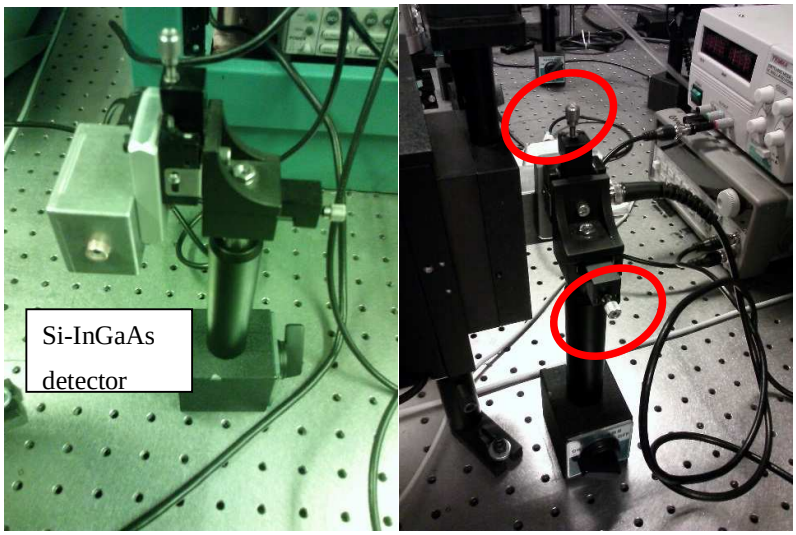

Getting the sample

- Go to the glove box, get your sample, and put it into the sample chamber
  - Put the glass side down (touching the holder)
  - Make sure the sample is tilted

- Put the sample chamber onto the stand
- Attach the vacuum hose to the sample chamber
  - Attach the clamp to the hose/sample holder
  - Open the black knob on the vacuum hose
  - Open the leaver on the sample chamber
  - Hold the vacuum hose until needle gauge says the sample chamber is under vacuum to avoid ripping off the top of the sample chamber

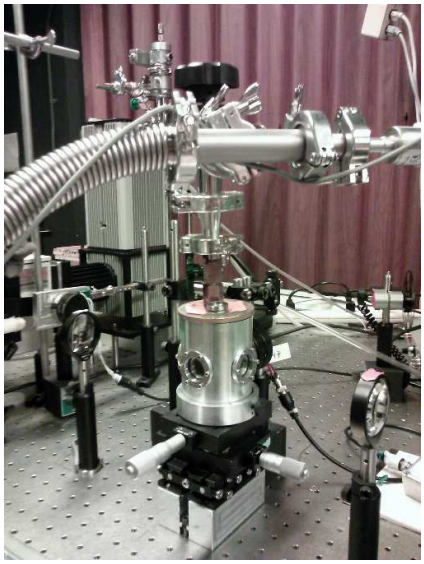

Setting the Phase and Checking for Signal

- Turn the room light off
- Turn the LED amplitude back up to 3V
- Open the “shutter” program
  - Close the Monochromater’s Shutter [Press run]

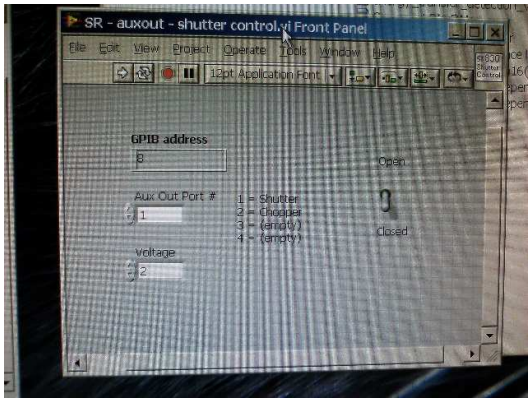

- On the “Set Wavelength” program
  - Select Port 3 and wavelength = 450 nm [Press run]

(but this changes based on LED e.g. Blue LED 450nm, Red LED 630nm)

- On the “Grating Change” program
  - Select Port 3 and grating = 1 [Press run]
- On the lock-in amplifier
  - Press the buttons under “sensitivity” until the signal is not overloaded
- Press the “phase” button On the lock-in amplifier
  - Make sure that the longpass filter is pushed aside when you do this
- Push the filter back into place
- On the “Set Wavelength” program
  - Select Port 2 and wavelength = 1000nm [Press run]
  - Select Port 3 and wavelength = 1000nm [Press run]
- On the “Gratings Change” program
  - Select Port 2 and gating = 2 [Press run]
  - Select Port 3 and grating = 2 [Press run]
- On the “shutter” program
  - Open the shutter [Press run]
- Press the “gain” button under the “auto” heading on the lock-in amplifier
- Open the “One Point PIA with Shutter” program [Press run]

- This tells you if you have any signal
- dT/T should be at least a couple ppm ($2x10^{-6}$)

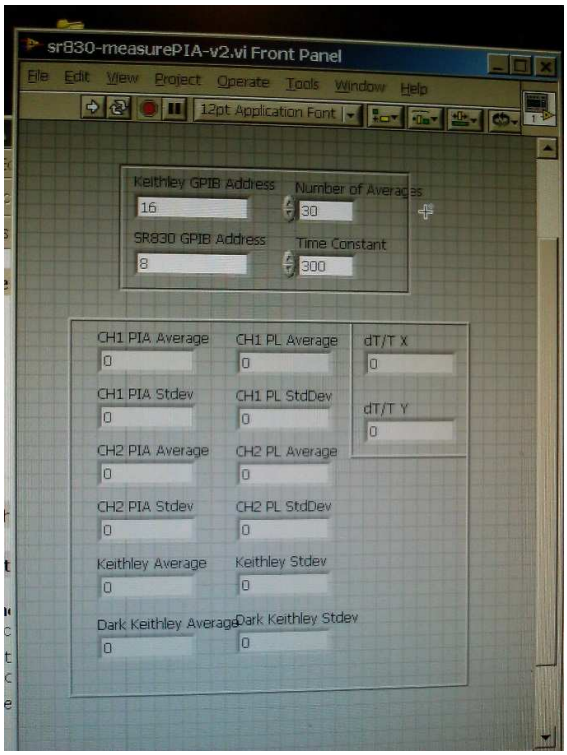

- Open the “PIA-scan shutter” program
  - Default Settings:

- Wav Start = 550nm
- Wav End = 1700nm
- Software Averages = 60
- Step Size = 10
- Delay Between Averages = 300ms
- Preread Delay = 1000ms
- First Wavelength = 4000
- Monochromater Settings: 2 and 3 (500um/500um slitwidth)
- Lockin Settings time const = 300ms
- Mod Freq = 200Hz
- Keithley address = 16
- SR830 address = 8
- Aglent 33120A address = 10

- Change LED bias to 3V
- [Press run]
- Wait until your data is collected

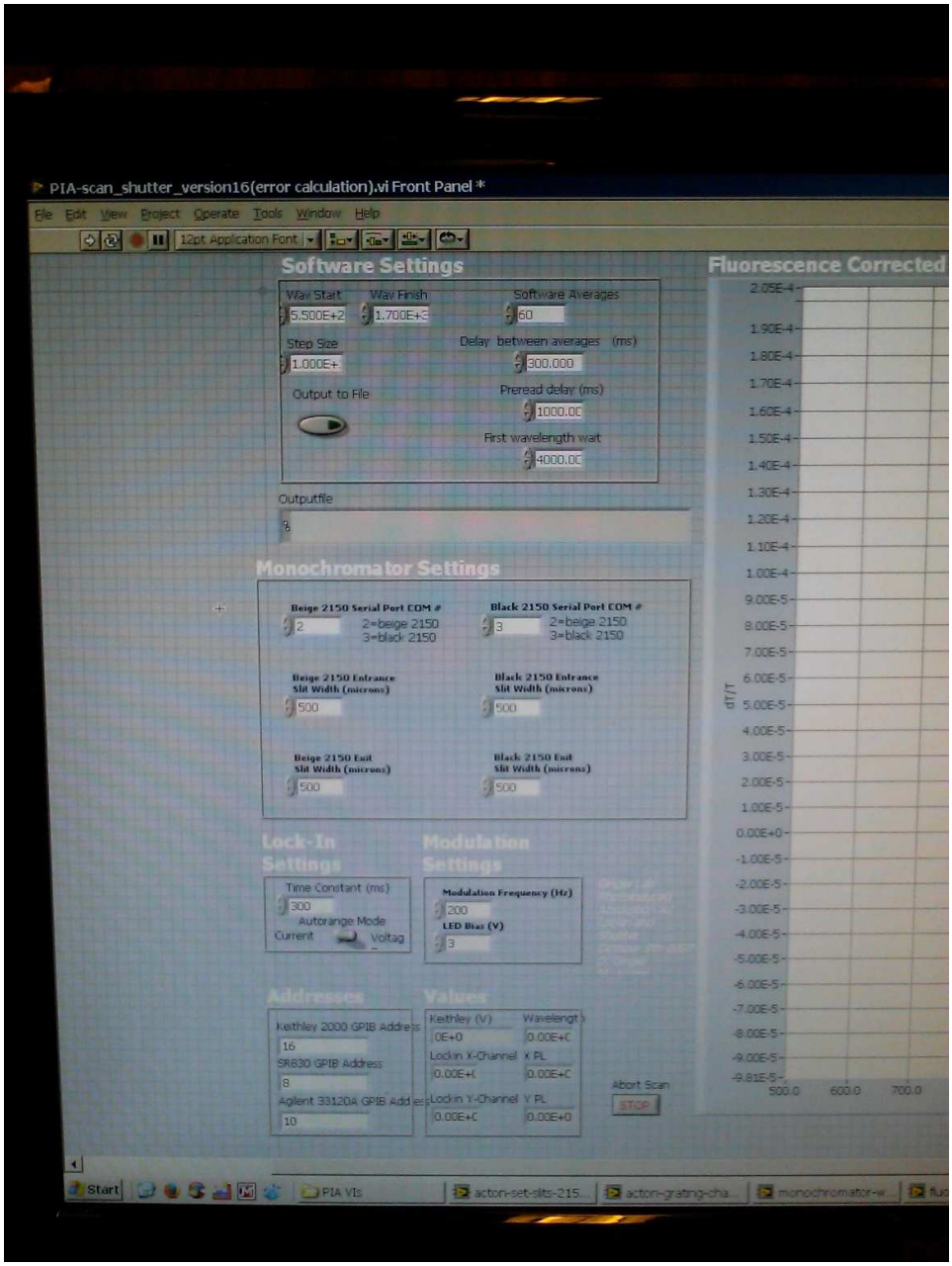

Measuring Frequency Modulation

- Unhook the photodiode BNC cable from the preamp
- Replace Si-InGaAs dual photodetector with amplified Silicon (Thorlabs, PDA36A) or InGaAs (Thorlabs, PDA10CS)

- Plug the power cable into the amplified photodiode
  - Make sure both the power cable and photodiode are **OFF** before plugging it in
- Unplug the bidirectional BNC cable from the preamp and plug it into the amplified Si photodiode
- On the lock-in, press the “notch” button under the “filters” heading
  - Make sure that no filters are selected now

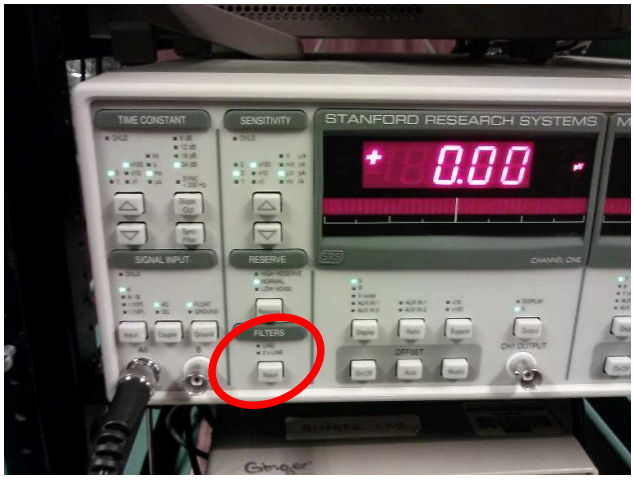

- On the “Set wavelength” program
  - Select port 2 and wavelength = 1000nm [Press run]
  - Select port 3 and wavelength = 1000nm [Press run]
- On the “Grating Change” program
  - Select port 2 and grating = 2 [Press run]
  - Select port 3 and grating = 2 [Press run]
- Open the shutter
- On the Kiethley, Press “local” so the number starts changing again
- With your hands, move the detector to optimize the signal on the Kiethley
- Close the shutter
- On the “Set wavelength” program
  - Select port 2 and wavelength = 450nm [Press run]
  - Select port 3 and wavelength = 450nm [Press run]

  (but this changes based on LED e.g. Blue LED 450nm, Red LED 630nm)
- On the “Grating Change” program
  - Select port 2 and grating = 1 [Press run]
  - Select port 3 and grating = 1 [Press run]
- On the lock-in amplifier
  - Press the buttons under “sensitivity” until the signal is not overloaded
  - Press the “phase” button

- Do this with the filter pushed aside
  - On the computer, open “Modulation Dependence log steps”
  - Default Settings:
- First frequency = 20Hz
- Last Frequency = 10000Hz
- Wavelength = 980nm
- Time Constant = 300ms
- Number of Points = 30
- Preread Delay = 1000ms
- Software Averages = 60
- Delay between averages = 300
  - Change LED bias to 3V
  - Change wavelength to 1140 nm for PTB1: PbS QDs because that’s where the maximum signal is.
  - [Press run]
- Wait while your data is collected

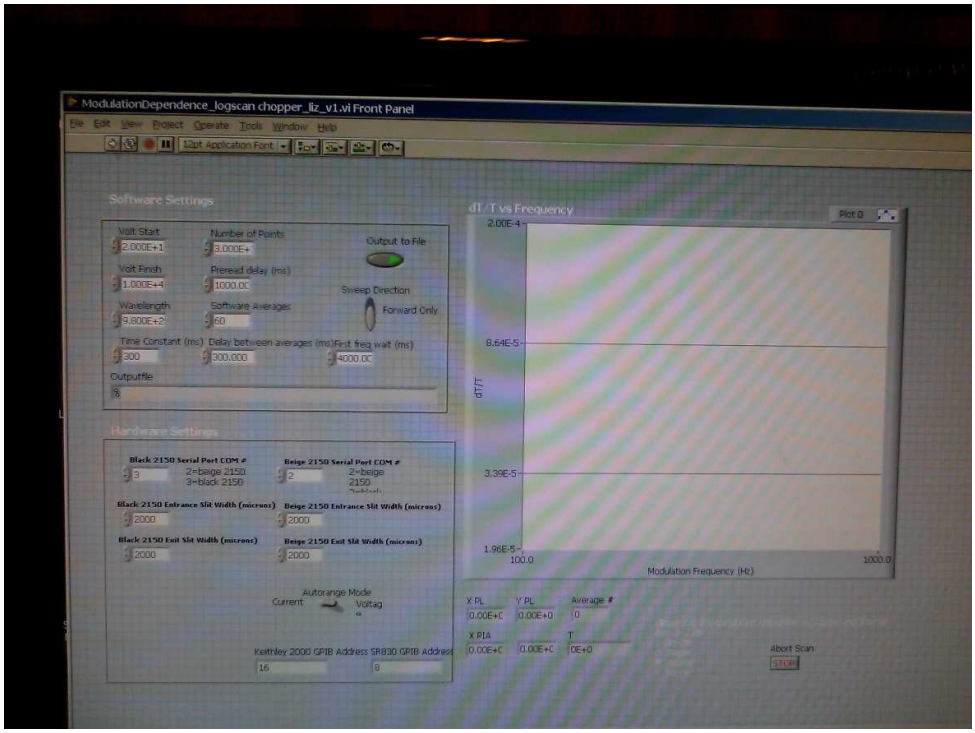
ModulationDependence_logscan chopper_liz_v1.vi Front Panel
File Edit View Project Operate Tools Window Help
12pt Application Font
Software Settings
Volt Start
2.000E+1
Number of Points
3.000E+
Output to File
Volt Finish
1.000E+4
Preread delay (ms)
1000.0C
Sweep Direction
Wavelength
9.800E+2
Software Averages
60
Forward Only
Time Constant (ms)
300
Delay between averages (ms)
300.000
First freq wait (ms)
4000.0C
Outputfile
Hardware Settings
Black 2150 Serial Port COM #
3
2=beige 2150
3=black 2150
Beige 2150 Serial Port COM #
2
2=beige
2150
Black 2150 Entrance Slit Width (microns)
2000
Beige 2150 Entrance Slit Width (microns)
2000
Black 2150 Exit Slit Width (microns)
2000
Beige 2150 Exit Slit Width (microns)
2000
Autorange Mode
Current
Voltag
Keithley 2000 GPIB Address
16
SR830 GPIB Address
8
dT / T vs Frequency
Plot 0
2.00E-4
8.64E-5
3.39E-5
1.96E-5
dT/T
100.0
1000.0
Modulation Frequency (Hz)
X PL
0.00E+C
Y PL
0.00E+0
Average #
0
X PIA
0.00E+C
T
0.00E+C
0E+0
Abort Scan
STOP